Technical University of Crete
School of Electrical and Computer Engineering

Development and integration of Mechatronics systems in Biomedical Microscopy

Diploma thesis

Christos Housos

Supervisor: Professor Balas Costas
Examination Committee: Professor Bucher Matthias
Examination Committee: Dr. Kortsalioudakis Nathanail

February 2021

Abstract

Microscopy has a critical role in both life, science, research and routine diagnosis. Microscopy has a long history of evolution with the today's contemporary systems offering a series of advanced digital imaging modalities towards the improved visualization of features of diagnostic importance. However, examining tissue samples in numerous slices of cm^2 size each at micron magnification level, requires enormous examination time that is clinically unrealistic. Due to this fact, examinations are performed on randomly selected representative tissue areas. This makes this life critical diagnostic procedure error prone and subjective, often resulting to high inter- and intra- observer disagreements. The advancement of mechatronics technologies in conjugation with the development of fast-multichannel imaging sensors and ultra-fast computational platforms, offer today unique possibilities for automated whole slide scanning and for improving diagnostic performance through Artificial Intelligence - Machine Learning methods. This thesis deals with the development of an integrated multimodal high content screening microscope offering also, improved spatial feature resolution power, approaching the performance of very expensive and delicate Confocal Microscopes. System Design schematics, Hardware Implementation, Systems Drivers and Graphical User Interface are presented and discussed together with preliminary technical and clinical validation.

Contents

List of Figures

Chapter 1

Introduction

Brief Description In the early days of evolution, people's desire to understand the microcosmos and the macrocosmos lead to the use of specialised machinery for enhanced observation. Since then, this desire expands in every direction with humanity's needs for knowledge and understanding, leading to the development of specialized systems. Biomedical imaging, as one of the main research fields demanding evolution, utilizes different observation techniques for imaging in biomedical sciences. The improvement of examination and diagnosis in these research fields is heavily dependent on technological advances.

Pathology is a medical subspecialty that practices the diagnosis of diseases. Microscopic examination of tissue reveals information capable of assisting the pathologist, in rendering accurate diagnoses and guiding therapy. The microscopic study of animal and plant cell and tissues through staining, sectioning and examination of them under a microscope (electron or light microscope), is called *Histology*. In order to enable scientists to study tissue characteristics and microscopic structures of the cells, a number of specialised techniques has been developed. Histological studies are used in forensic investigations, autopsy, diagnosis and education, among other fields. Additionally, histology is extensively used in medicine, especially in the study of diseased tissues to aid treatment. Staining of the tissues under examination with various stains which reveal tissue differences, is commonly used by histologists in order to validate their theories through observation. Early histologists used to utilise readily available chemicals to prepare tissues for microscopic studies. The methods of histological staining through chemical, molecular biology assays and immunological techniques, is typically referred to as *Histochemistry*.

Histopathological analysis of biopsy or surgical specimens, a common clinical practice for diagnostic purposes, requires inspection of hundreds of microscope's slides. Essentially, this process involves cutting the biopsy or surgical sample into very thin slices, placing them on glass slides and examining them under a microscope. Predominantly, the placement, positioning, and view control is -in most clinics and hospitals- done manually by the pathologists. For this reason, diagnosis still remains heavily dependent on the experience and performance of the pathologist.

Computer-based image analysis is already available in commercial diagnostic systems. At the same time, further advances in image analysis algorithms are needed, in order to fully realize the benefits of digital pathology in medical discovery and patient care. In the coming decades, pathology image analysis is even expected to extend beyond streamlining of diagnostic workflows and minimizing interobserver variability. It will seemingly proceed towards assisting diagnosis and treatment, as well as predicting patient outcomes and therapeutic responses.

Over the recent years, a wide range of optical imaging modalities based on multiple observation techniques have emerged. The motivation behind this tendency is the fact that a single technique is often unable to provide all of the required information, given optimal temporal and spatial resolution. Complementary techniques are needed, in order to achieve a full understanding of the structural and biochemical changes that occur in cellulosic materials, as they undergo physical, chemical or biochemical processing.

The host of techniques that allow visualisation with resolution in the submicron to nanometer scale, is generally referred to as *advanced-microscopy*. This level of detail enables the study of biomolecular structures, interactions, and mechanisms of catalysis at the fundamental length scale of proteins, lipids, amino acids, glycans, and other biomolecules. To that end, the advantages of advanced-microscopy techniques make them especially suitable for biomedical imaging. While many of these techniques are utilised in biological research and medical applications, the combination of different techniques can be a key factor in unlocking their full potential. However, the integration of different imaging modalities is often challenging, mostly due to the wide variation of hardware requirements. The need for rapid evolution in microscopy can be fulfilled by developing technologies, focused on integrating multiple imaging modalities and exploring applications of these techniques.

During the recent years, there has also been an increasing interest in automated microscopy, especially for automating many of the most labor-intensive tasks in microscopy applications. Much like in the industrial sector, automation of these vision systems reveals entirely new possibilities. Overall, full motorization combined with digitization of the microscope's images and custom lighting, is able to constitute a powerful and autonomous system which can be programmed to execute specialized image acquisitions with great accuracy and repeatability.

All in all, such systems intend to give specialists a machine, capable of executing all the tasks of a classic microscope, but with exceptional ease, speed, accuracy, repeatability, data management and automation.

Purpose of the Design The proposed system of our research is an easy to install and use motorized extension for digital microscopes. We aim to fully control and automate the mechanical and optical parts of a microscope, with which the specialists interact the most. This will result to a microscope extension that can scan and analyze the given samples with various techniques and minimal human interaction.

Motorization of the most used parts of a microscope is essential and can lead to a comfortable and relaxing imaging experience compared with the classical microscope usage. Moreover, operator skill requirements will be reduced, as the system can be set up through software, allowing for a simplified interface and use. This also improves the repeatability of image capturing and measurements between operators at varying skill levels. At the same time, automation reduces contact with the samples, therefore allowing a better analysis, by minimizing alterations in the results and other risks

Automation will also contribute to increase the number of techniques to be illustrated at the same time, which is always a tedious task. Overall, such a system is very useful in terms of comfort and speed, as well as accurate data analysis and image processing techniques, giving a different perspective in the way we observe and analyze the samples. In fact, an automatic system will provide a way to improve diagnostics, reducing the time required for the analysis.

Structure of the Thesis In the following chapters of the thesis as well as in this one, the whole research and work is presented in full detail. The first two chapters focus on the technology of microscopy as well as the research that was made. The following chapters focus on the presentation of the final result of our microscope and the way it was implemented.

Chapter 1 delineates the current state of microscopy and the reasons that led to this thesis subject. It introduces a brief description of our microscope purpose and functionality.

Chapter 2 presents the research made on microscopy and its techniques, while explaining the terminologies of microscopy. It starts with a brief history of Microscopy and continues with the presentation of microscopy techniques, that have been researched. Additionally, it includes the research made on the state of the art in microscopy.

Chapter 3 analyzes the proposed system design of our microscope. The main goal is to construct an easy to install and use motorized extension for digital microscopes. The analysis is continued with an insightful review of the hardware and software segmentation regarding the development of the microscope.

Chapter 4, the most extensive chapter, describes in detail the technical implementation of the microscope's system. The high level requirements, the proposed designs as well as the qualification and verification for each method are addressed. Beginning with, it focuses on designing a Modular Stepper Motor Driver. Subsequently, the essential and indispensable component of automated microscopes and the automatic focusing procedures are presented. Furthermore, it describes in detail the technical implementation of the core mechanics and results of our Absolute Metric for Focus Quality implementation. A Z-Stack Processing implementation and it's potential application on our microscope are also addressed. The chapter concludes with a presentation of our developed microscope.

Chapter 5 summarizes the results of the research. The chapter ends with suggestions and notes for future work.

From the beginning of my engagement with this research, there was time consuming problems and issues that could not have been handled without the precious help of the people i worked with. I want to especially thank my Supervisor Costas Balas, for providing clear guidance and supervision in every difficult decision and task of this thesis. I also want to thank my co-supervisors Matthias Bucher and Kortsalioudakis Nathanail for the helpful thoughts, discussion and for reading my research report, providing useful feedback.

Moreover, there were huge contribution to my work from the engineers of Spectricon and the researchers of Electronics Laboratory in Technical University of Crete. More specifically, i want to thank Thanasis Tsapras, Christos Rossos and Nikos Kaminakis, for the time and effort provided in order to design and construct, in real scale, all the hardware components of my research. For the contribution and knowledge while designing the software of the system, i want to render special thanks to Babis Boras, Makis Stefatos, Manos Gialitakis and all the researchers i worked with closely. Last but not least, i want to thank to Panagiotis Tsopelas and Dimitris Markelos for the knowledge and effort provided in the evaluation of every stage of my research results.

Additionally, i want to specially thank my fellow friends Theofilos Christodoulou, Yiannis Kritikos, Fotis Giariskanis and Stefanos Kargakos for their time, contributing with ideas and discussions while constructing this report. Finally, i want to thank my family and my girlfriend, for their patience and support in this intensive working period.

This research became possible with all these people contribution and i am grateful for knowing them and having them in my life.

Chapter 2

Background

2.1 Brief History of Microscopy

Historically, Microscopy may be certainly traced back to the thirteenth century and even to early AD. The term used in that era was "burning glasses", referring to the lenses used for the magnification, which can be found in Roman philosophers' writings. An early example of magnification that is the most often quoted is found in Seneca's "Quaestiones Naturales" (63 AD) "Letters, however small and dim, are comparatively large and distinct when seen through a glass globe filed with water."

In the following years, historical writings and reports state that this technique with "burning glasses" and water were only used. It is not till the sixteenth century that scientific curiosity and the study of nature led to further exploration of different techniques. The earliest microscopes that started to emerge had the shape of a tube made of opaque material with a single lens at one end and a flat glass plate at the other end. The later plate was used for placing the object to be examined. These simple instruments were used to study small insects which were placed on the glass plate. By placing the small objects on the glass plate researchers could later light by candle light or hold up these tubes towards the sun and thereby utilise the maximum light. These early prototypes of microscopes were spoken of as flea glass "vitrea pulicaria" or fly glass "vitrea muscaria".

Regarding the first microscope, it was perhaps formed of two convex lenses and it's invention was former to the telescope. Most probably it was Galileo who was the discoverer of the microscope in 1608 and it was later improved by Kepler in 1611 with his mathematical analysis. [1] The word "microscope" was coined in 1625 in Italy by Giovanni Faber, a member of the first Accademia Dei Lincei, after his fellow's member Gallileo's creation. The word is derived from the two Greek words "small" and "to look at".

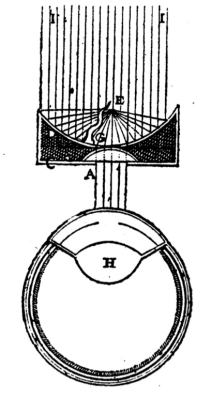

Figure 2.1: Earliest known picture of Simple Microscope - Descartes 1937
Source: Section Of The History Of Medicine - Notes on the Early History of Microscopy.

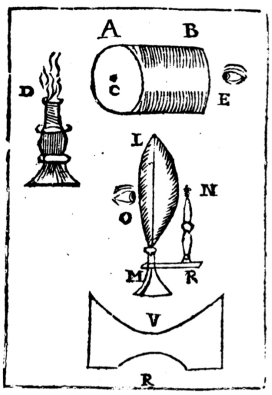

Figure 2.2: Kircher's diagram of a simple microscope.
Source: Section Of The History Of Medicine - Notes on the Early History of Microscopy.

A few years after Galileo's microscope, in 1637 the first printed images of microscopes 2.1 have been introduced by Descartes in his short treatise "La dioptrique" (in English "Optics", or "Dioptrics") and provided descriptions of microscopes. Followed in the year 1646 Athanasius Kircher presented his microscope 2.2 in his "Ars Magna Lucis et Umbrae". In Kircher's microscope the object to be examined was placed on the glass plate at C and illuminated by the candle D, the lens being at the opposite end, E, of the tube A B. Athanasius Kircher was one of the first to take a notably modern approach with microscopes to investigate the blood of plague victims.
We could surely state that these years had a great increase in the research of microscopy that will eventually define the modern microscopy. Following Kircher's microscope, more scholars began polishing and grinding lenses when they discovered that certain shaped lenses could increase the studied objects' size. One of the most notable scholars was Anton van Leeuwenhoek who succeeded in a usable magnification of 30X or 40X. One of the Anton van Leeuwenhoek's microscopes consisted merely of a metal plate pierced by a small hole into which a minute lens(L) was fitted. This plate fitted on a frame into which a tube containing a small live eel was placed. By adjusting screws the tail of the eel could be brought into focus, and the capillary circulation examined.

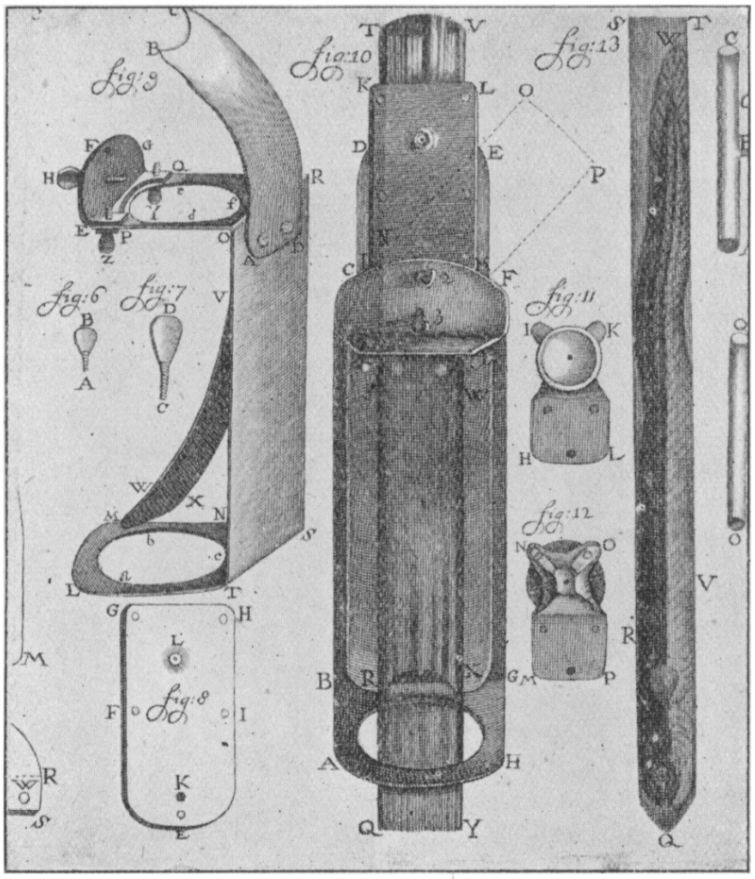

Figure 2.3: One of Anton van Leeuwenhoek's Microscopes
Source: Section Of The History Of Medicine - Notes on the Early History of Microscopy.

These types of microscopes were largely used in the following years. However the next major improvement needed almost 100 years. In 1729, the achromatic lens was developed for use in eyeglasses by the English optician Chester Moore Hall, and first manufactured commercially by J. Dollond in 1758, which crucially improved the quality of microscopes. Although, a period of more incisive observation has started, the microscopes were still very imperfect and it was not until their mechanical improvements in the 18th and 19th century that the full effect of their use was utilised. In the 18th and 19th century, microscopes became more stable and smaller, while the lens improvements that took place solved many of the optical problems. August Kohler invented a way to provide uniform microscope illumination, reducing optical glare from the light source and his invention revolutionized light microscope design. Additionaly, Ernst Leitz devised a way that

would allow for different magnifications using only one microscope by placing multiple lenses on a movable turret at the end of the lens tube.

In the beginning of the 20th century microscopes have seen major improvements most of which are used until today, yet there were even more to be made. In the start of the 20th century the German physicist, Ernst Ruska, working with electrical engineer Max Knoll, developed the electron microscope, a significant alternative to the light microscope, an instrument that uses a beam of electrons rather than light to generate an image. The use of electrons, instead of light, allowed for much higher resolution and thus could reveal the structure of smaller objects.

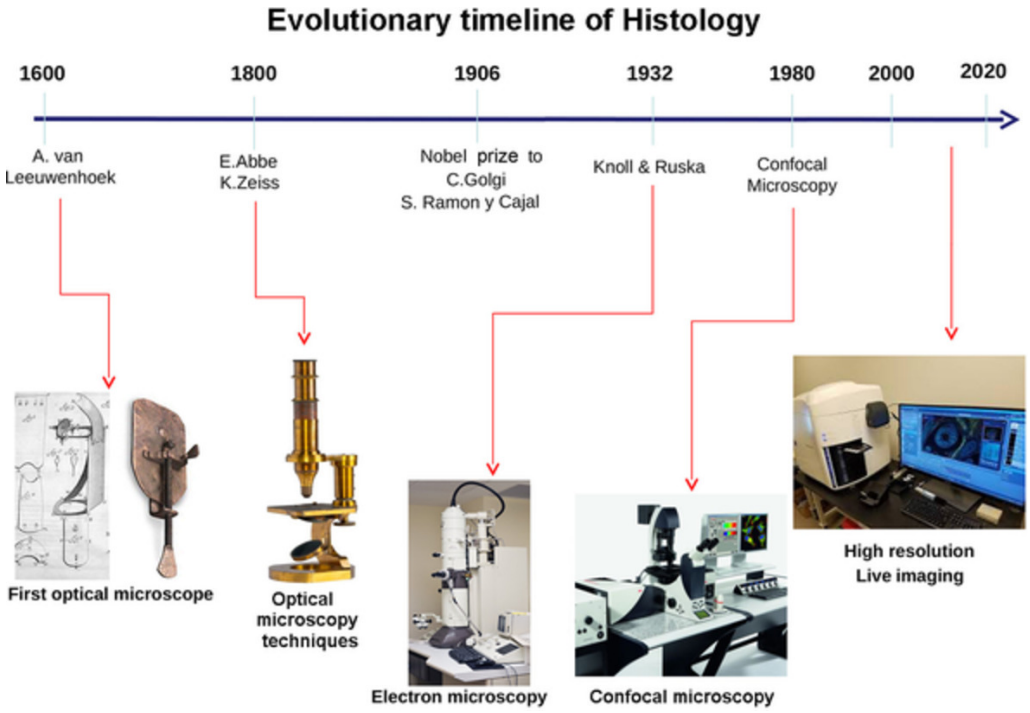

Figure 2.4: Evolution of Microscopes

Over the last years, the most recent developments in light microscope largely centre on the rise of fluorescence microscopy and the superresolution analysis of fluorescently labelled samples. In 1957, Marvin Minsky patended the principle of confocal imaging aiming to overcome some limitations of traditional wide-field fluorescence microscopes.

2.2 Microscopy Technologies

Microscopy, as an observation technological sector, uses light and optics to enhance the observer's capabilities of understanding the sample's structure. Light, is the primary vehicle for transporting energy either for big scale (universe) or for micro scale (microscopy) phenomena. As a phenomenon, light is complex and it is classically described with a simple model based on rays and wavefronts, which belongs to a larger family of wave-like phenomena, the electromagnetic radiation. The visible light (400 to 700 nanometers) to which the human eye responds, is a very small fraction of the entire electromagnetic radiation spectrum. The remainder of the electromagnetic spectrum is invisible to humans.

Microscopy, in its early days, relied on oil lamps and natural sunlight to provide an external source of illumination for their primitive (but often remarkably accurate) microscopes. Unfortunately, these methods did not provide reliable illumination and frequently the area of field illumination greatly exceeded the numerical aperture of the objective, causing glare and flooding.

Evolution of the light sources and optics used for specimen observation, enhanced the imaging quality and thus accuracy of assessment. Modern microscopy have developed a wide spectrum of useful modalities for life science research. These modalities are designed to aid in contrast enhancement and provide better observation and photomicrography of specimens.

In the research field of biomedical engineering, new microscopy technologies arises with the evolution of the observation. In the following diagram, Figure [2.5], some of the most recent microscopy techniques are plotted based on their capabilities on terms of Field of View and Spatial Resolution.

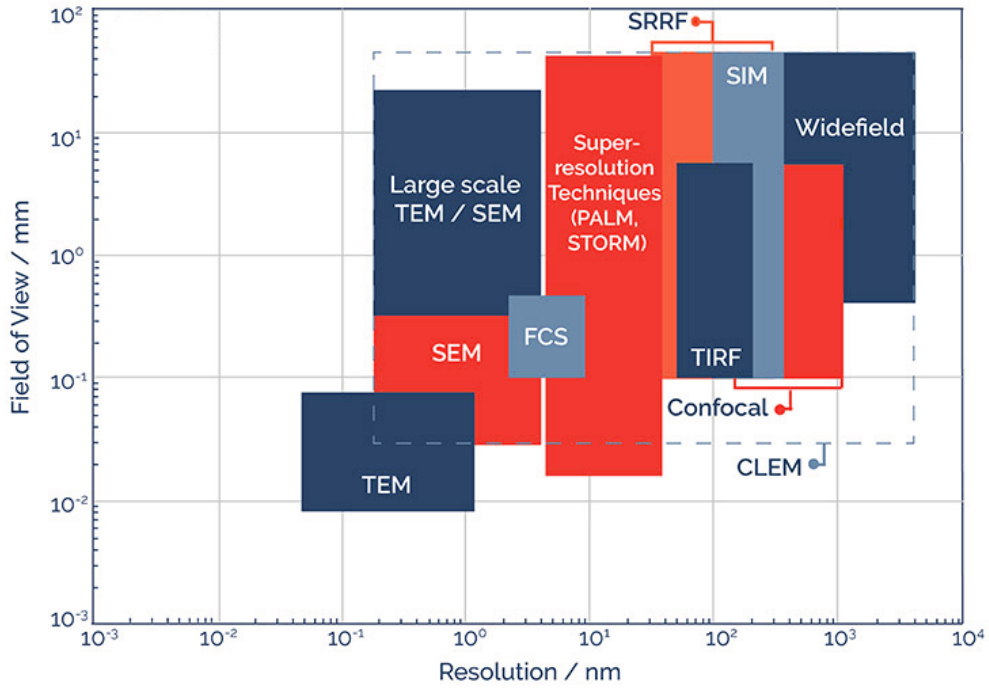

Figure 2.5: Microscopy Techniques
Source: Learning Center - ANDOR

Microscopy techniques shown in Figure [2.5], are separated in terms of illumination and observation types. In this thesis we are interested in two of the most widely used techniques and the state of the art optimization methods used in each technique. In the top right corner of this graph stands Widefield Microscopy (WF), which is one of the most basic modalities widely used in modern microscopy. Next, moving towards higher resolution microscopy is Confocal microscopy, a complex optical microscopy technique for increasing optical resolution and contrast of a micrograph by means of using a spatial pinhole to block out-of-focus light in image formation.

2.2.1 Widefield Microscopy

Widefield microscopy, is fundamentally any technique in which the entire specimen of interest is exposed to the light source with the resulting image being viewed either by the observer or a camera. In this section, microscope configurations for WF imaging will be discussed looking at light paths involved, the problems of out-of-focus light, as well as some of the more advanced WF techniques, such as WF Super-Resolution.

Brightfield Microscopy The most basic form of Widefield microscopy is 'brightfield microscopy' in which the entire specimen is illuminated by white light either from above (in an inverted configuration), or below (in a standard upright microscope), as shown in Figure [2.6]. This configuration has influence on the specimen which can be investigated. Upright microscopes are commonly used for applications with fixed samples, mounted on glass slides. Inverted microscopes have been invented to watch living cells. They are commonly grown in liquid solutions. Only a configuration with the objective below and the condenser above the specimen guarantees a close enough proximity of the objective to the specimen.

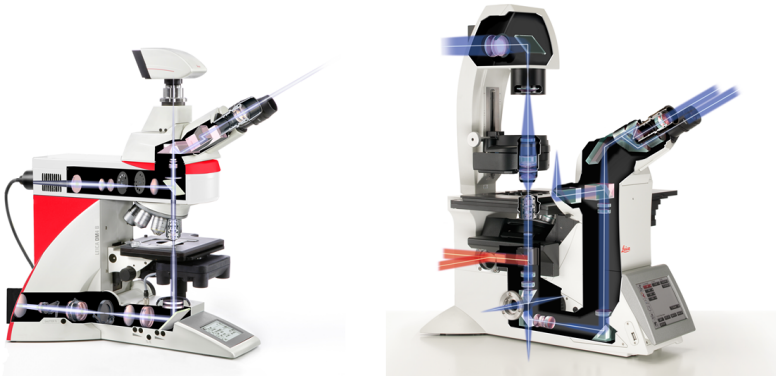

Figure 2.6: Widefield Microscopy Setups
Source: leica-microsystems.com

Construction of a microscope using the brightfield microscopy technique, is based on these components.

- **Light Source:** Trans-illumination below sample that propagates through to condenser and objective lens. Typically a broadband source such as a quartz halogen bulb or LEDs is used.
- **Condenser Lens:** Collects trans-illuminated light and focuses to sample.
- **Objective Lens:** Collects light which propagates through sample and enhances details by a factor of magnification.
- **Eyepiece/Camera:** Views or records the image.

There are some limitations to the brightfield microscopy technique, which include very low contrast or blurriness (out-of-focus material) for cellular or biological samples and low optical resolution due to limitations of light. Finally, samples that are naturally colorless and transparent cannot be seen well and often have to be stained before viewing.

Enhancing the resolution of a Brightfield microscope is accomplished by various simple methods. By reducing or increasing the amount of the light source by the iris diaphragm. Use of a colored (usually blue) or polarizing filter on the light source to highlight features not visible under white light. Use of an oil-immersion objective lens and a special immersion oil placed on a glass cover over the specimen.

However, simplicity of the brightfield technique is a huge benefit when first imaging an unknown sample. Additional optical microscopy applications include darkfield illumination, phase contrast, fluorescence, and differential interference contrast.

A typical brightfield illumination image has a dark sample with a white background, the darker the regions on a sample, the more absorption of light that has occurred, as shown in Figure[2.7].

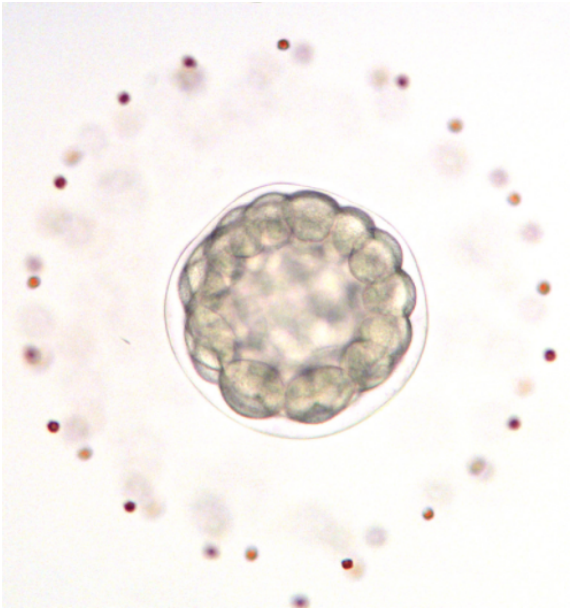

Figure 2.7: Bright Field technique in a sand dollar (Dendraster excentricus) embryo.
Source: igor.wikidot.com/article:simple-microscopy-tricks

Dark-field Microscopy In optical microscopy, dark-field describes a microscopy technique used to enhance the contrast in unstained samples. Dark-field microscopy describes microscopy methods, which exclude the unscattered light beam from the image. As a result, the field around the specimen (background) is generally dark.

Dark-field microscopy is a very simple yet effective technique and well suited for uses involving live and unstained biological samples. Considering the simplicity of the setup, as shown in Figure [2.8], the quality of images obtained from this technique is impressive.

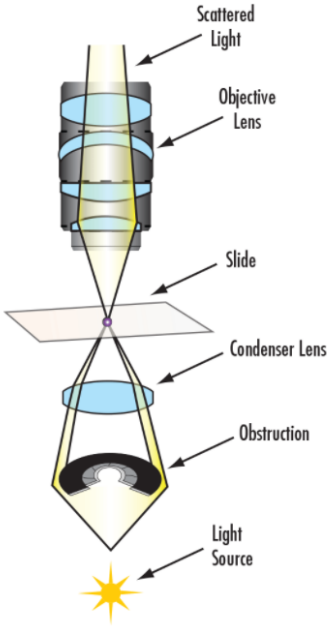

Figure 2.8: Darkfield Microscopy Setup
Source: edmundoptics.com

Construction of a microscope using the dark-field modality, is based on these components.

- **Light Source:** Enters the microscope and hits the dark field patch stop, which is a disc used to block light from entering the condenser and leaves a circular ring of illumination. Typically a broadband source such as a quartz halogen bulb or LEDs is used.
- **Condenser Lens:** Collects outer ring of illumination and focuses it on the sample.
- **Objective Lens:** Light hits the sample, and is transmitted or scattered from it. Scattered light enters the objective lens, whereas transmitted light is not collected by the lens. The direct illumination block assists in this step.
- **Eyepiece/Camera:** Views or records the image.

Dark-field microscopy has its own limitations. The low light levels seen in the final image, demands that the sample must be very strongly illuminated, which can cause damage. The interpretation of dark-field images must be done with great care, as common dark features of bright-field microscopy images may be invisible, and vice versa. In general the dark-field image lacks the low spatial frequencies associated with the bright-field image, making the image a high-passed version of the underlying structure.

A typical darkfield illumination image has a white/bright specimen with a dark background and environment filling the image. This is the exact opposite of a brightfield illumination image, and is useful for unstained specimens or images that require increased contrast. The advantage with using darkfield illumination is that unstained specimens can remain alive and vital, whereas their brightfield counterparts must be treated and are no longer active. Also, it is possible to acquire more qualitative results with this technique through live cellular analysis, as shown in Figure[2.9].

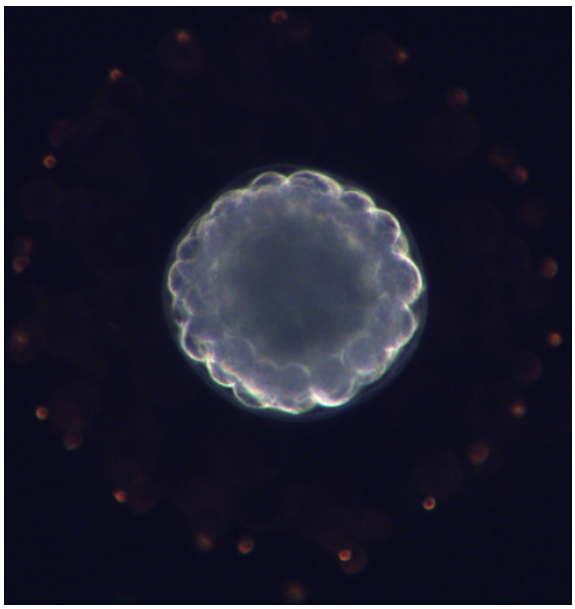

Figure 2.9: Dark Field transillumination technique in a sample of a sand dollar embryo.
Source: igor.wikidot.com/article:simple-microscopy-tricks

While the dark-field image may first appear to be a negative of the bright-field image, different effects are visible in each. In bright-field microscopy, features are visible where either a shadow is cast on the surface by the incident light or a part of the surface is less reflective, possibly by the presence of pits or scratches. Raised features that are too smooth to cast shadows will not appear in bright-field images, but the light that reflects off the sides of the feature will be visible in the dark-field images.

Epi-fluorescence Microscopy Epi-fluorescence is the term used to describe fluorescence microscopy in which the same lens (objective) is used to both illuminate and collect the emitted light from a sample. Light travels from the light source, passes through a filter set, through a dichromatic mirror and the shorter wavelength excitation light is reflected onto the sample via an objective. The longer wavelength emitted light from the sample travels back through the objective and passes through the dichromatic mirror to be imaged down the eyepieces and/or collected by a camera.

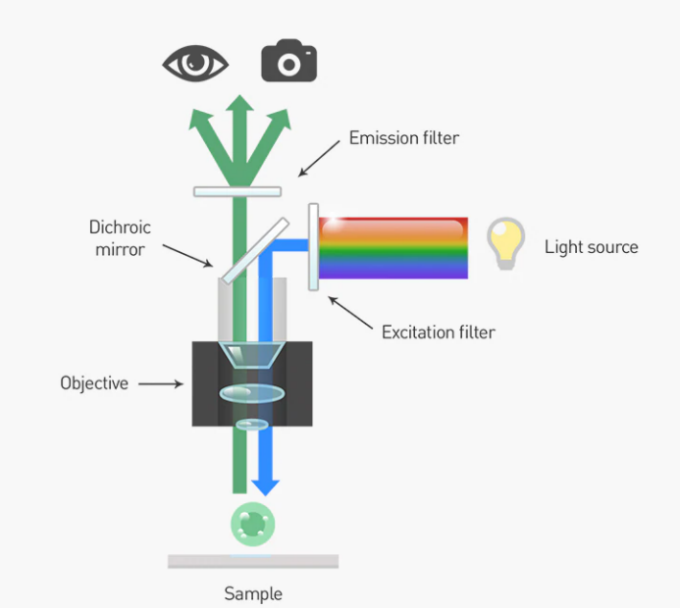

Figure 2.10: Epi-fluorescence Microscopy Setup
Source: thermofisher.com

Construction of a microscope using the Epi-fluorescence illumination technique, is based on these components.

- **Light Source:** Usually a xenon arc or mercury vapor lamp or more recently powerful LEDs.
- **Excitation Filter:** Narrows the wavelengths of the incoming light to only those used to excite the sample.
- **Dichroic beamsplitter or mirror:** Reflects the excitation light to the sample and simultaneously transmit only the emitted light from the sample back to the detector.
- **Emission Filter:** Transmits only the wavelengths of the emitted light from the sample and blocks all the light passed through the excitation filter.
- **Eyepiece/Camera:** Views or records the image.

A filter set will be designed to capture the maximum excitation and emission wavelengths of a given fluorophore, but will not capture all of the fluorescence. Most modern filter sets are designed so that the excitation filter has a defined band of wavelengths that it allows through. This style of filter is referred to as a band-pass filter. Band-pass filters are normally identified by the middle-value wavelength and the width of a band. In a simple epi-fluorescence microscope setup, once the excitation light leaves the excitation filter it is reflected onto the target. The fluorophores in the target become excited and then emit light that is shifted towards the red end of the spectrum (compared to the excitation light). Not all of this emitted light will be captured by the detector—only what is allowed through the dichroic beam-splitter and also passes through the emission filter. Emission filters are usually band-pass or long-pass filters, depending on the specific fluorophore and imaging experiment. A long-pass filter may be desirable if you need all the light beyond a certain wavelength to pass through to the detector, as shown in Figure [2.11].

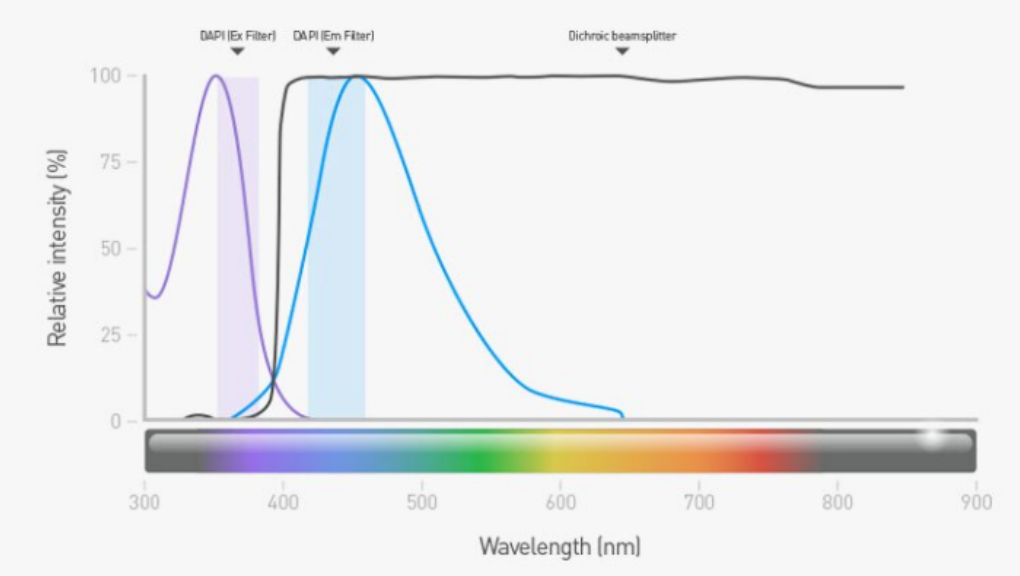

Figure 2.11: Epi-fluorescence Microscopy Spectrum
Source: thermofisher.com

Epi-fluorescence illumination compound microscope also have limitaitions based on the spatial resolution. It cannot resolve or distinguish between two objects that are less than 200 nm apart. Additionally, because the whole sample is illuminated at the same time, these setups are detecting all of the in-focus and out-of-focus light in your sample. These limitations mean that, depending on the lenses in your objectives, the system will be able to determine that two different-colored probes are present in the same cell, but not always be able to resolve their spatial relationship to each other without a lot of controls, individual pixel analysis, and math. By understanding and working within the limitations of these systems, designers can be confident about the data and images they collect, as well as being able to fully understand the data and formulate conclusions. The use of lasers in Epi-fluorescence microscopy, narrows the excitation range to 2–3 nm which is around 10 times narrower than the range of wavelengths you get when using excitation filters, as a result we observe increase in resolution, as shown in Figure [2.12].

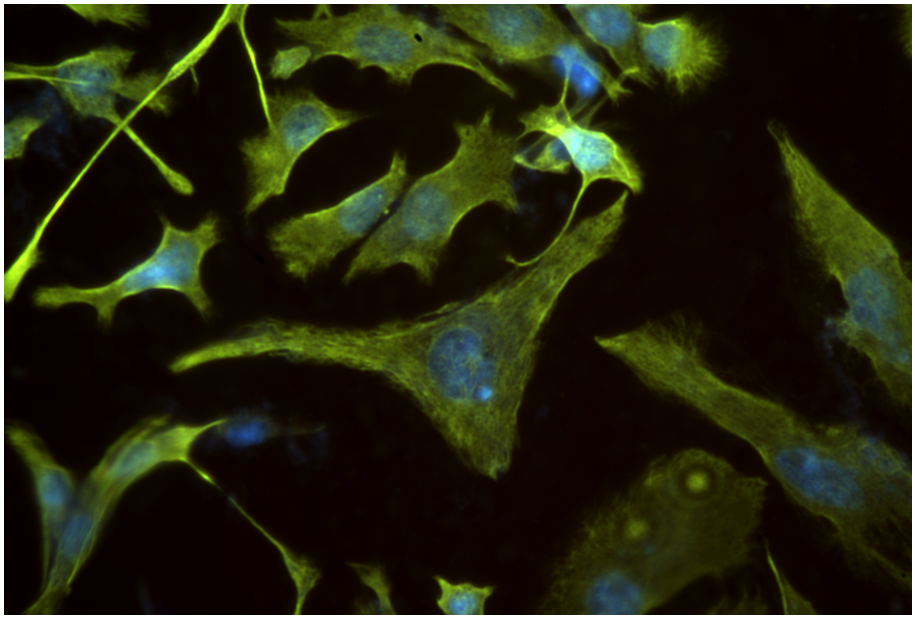

Figure 2.12: Epi-fluorescence Microscopy results using lasers

2.2.2 Confocal Microscopy

In the recent years there has been a tremendous explosion in the popularity of confocal microscopy, due in part to the relative ease with which extremely high-quality images can be obtained from specimens prepared for conventional fluorescence microscopy, and the growing number of applications in cell biology that rely on imaging both fixed and living cells and tissues. Confocal technology is proving to be one of the most important advances ever achieved in optical microscopy. The principle of confocal imaging was patented in 1957 by Marvin Minsky and aims to overcome some limitations of traditional wide-field fluorescence microscopes.

Principal of Operation Confocal microscopy, is an optical imaging technique for increasing optical resolution and contrast of a micrograph by means of using a spatial pinhole to block out-of-focus light in image formation. A confocal microscope uses point illumination and a pinhole in an optically conjugate plane in front of the detector to eliminate out-of-focus signal – the name "confocal" stems from this configuration. As only light produced by fluorescence very close to the focal plane can be detected, the image's optical resolution, particularly in the sample depth direction, is much better than that of wide-field microscopes. However, as much of the light from sample fluorescence is blocked at the pinhole, this increased resolution is at the cost of decreased signal intensity – so long exposures are often required. The setup of such a system is presented in Figure [2.13].

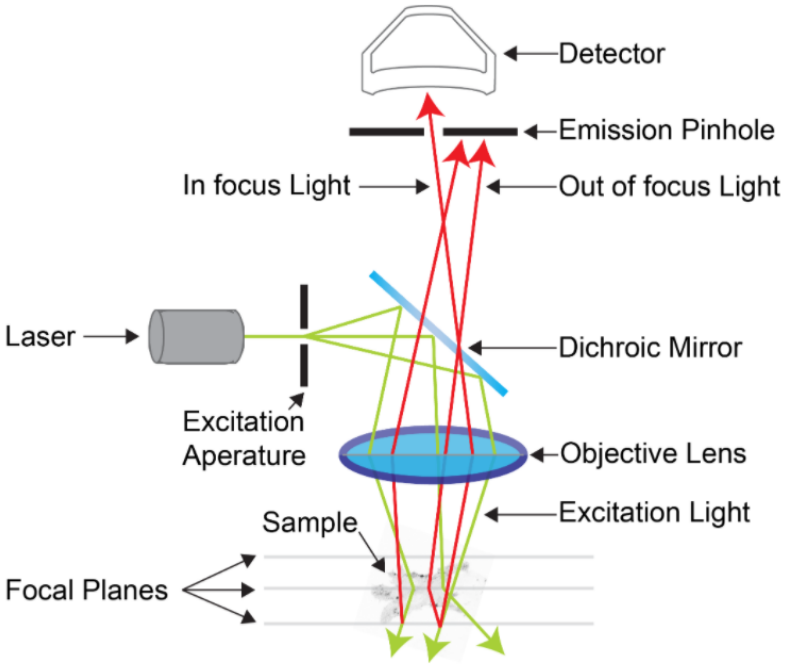

Figure 2.13: Confocal Microscope Configuration
Source: The University of Queensland uq.edu.au

This type of confocal setups have significant draw backs compared to a Widefield microscope, in terms of complexity and construction restrictions (size, weight and design flexibility).

The achievable thickness of the focal plane is defined mostly by the wavelength of the used light divided by the numerical aperture of the objective lens, but also by the optical properties of the specimen. The thin optical sectioning possible makes these types of microscopes particularly good at 3D imaging and surface profiling of samples. As only one point in the sample is illuminated at a time, 2D or 3D imaging requires scanning over a regular raster in the specimen.

Laser Scanning Confocal Microscopy (LSCM) The LSCM achieves a controlled and highly limited depth of focus, using a focused laser driven by a galvanometer-based scanning system. As the laser is reflected by a dichromatic mirror and scanned across the specimen in a defined focal plane, secondary fluorescence emitted from points on the specimen (in the same focal plane) pass back through the dichromatic mirror and are focused as a confocal point at the detector pinhole aperture. This spot, in turn, forms a reflected epi-fluorescence image on the original pinhole. If the specimen is in focus, the light passes through the pinhole to a detector (usually a photomultiplier). When the specimen is not in focus, the light reflected from it is defocused at the pinhole and very little passes through. Thus, fluorescence emission returning from the specimen to the detector is spatially filtered. As the pinhole aperture is reduced in size, it blocks more of the stray light from being detected but also lowers the total signal level. Although the absolute signal value is far less than observed with the widefield microscope configuration, rejecting the light from other focal planes increases the specific signal-to-noise ratio for the features of interest [2] [3]. The construction of a Laser Scanning Confocal Microscope is shown in Figure [2.14].

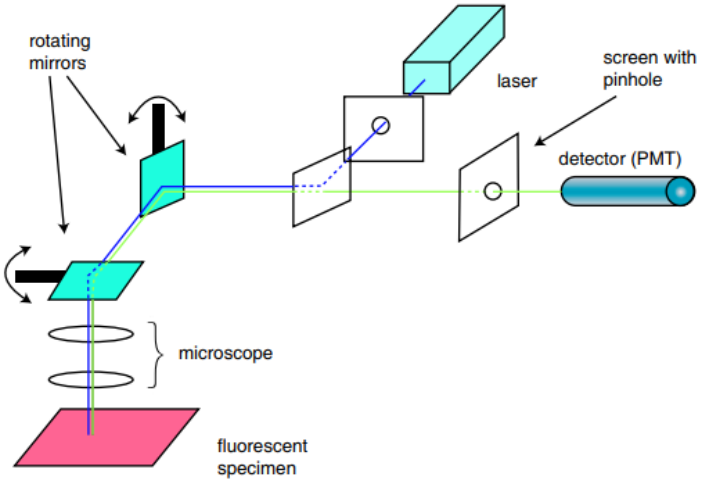

Figure 2.14: Laser Scanning Confocal Microscope Configuration
Source: The University of Queensland uq.edu.au

The beam is scanned across the sample in the horizontal plane by using one or more (servo controlled) oscillating mirrors. This scanning method usually has a low reaction latency and the scan speed can be varied. Slower scans provide a better signal-to-noise ratio, resulting in better contrast. Successive slices make up a 'z-stack', which can either be processed to create a 3D image, or it is merged into a 2D stack (predominately the maximum pixel intensity is taken, other common methods include using the standard deviation or summing the pixels).

Using this technique has several advantages over conventional microscopy techniques such as, increase of the optical resolution, greater contrast, controllable depth of field, reduced noise, elimination of image degrading out-of-focus information and the capability to collect serial optical sections from thick specimens.

On the other hand, the harmful nature of high-intensity laser irradiation to living cells and tissues, the limited number of excitation wavelengths available with common lasers, the photobleaching of the out of focus planes and the high cost of purchasing and operating multi-user confocal microscope systems, are some of the most significant disadvantages of using a method like this.

In order to construct a confocal imaging system with more advantages, we could use slit apertures instead of pinholes. Using slit apertures the signal level is increased and, if a detector array is used, a line image can be generated in real time. [4]

Spinning Disk Confocal Microscopy (SDCM) A variation of the galvanometer-based confocal microscope is the spinning disk confocal microscope, which can operate in real time (30 frames per second) or even faster to capture dynamic events in a wide spectrum of timescales. Spinning disk confocal microscopy (SDCM) represents an alternative to LSCM. Rather than a single pinhole, a SDCM has hundreds of pinholes arranged in spirals on an opaque disk, which rotates at high speeds. When spun, the pinholes scan across the sample in rows, building up an image. Using a spinning disk vastly improves the speed of image acquisition (allowing for imaging of fast dynamic processes and live specimens), and considerably reduces photo damage.

The principle is based on a Nipkow-style disk that is opaque with the exception of thousands of drilled or etched pinholes, often covered with miniature focusing lenses, arranged in interleaved Archimedean spiral patterns. Each illuminated pinhole on the disk is imaged by the objective to a diffraction-limited spot on the specimen. The fluorescence emission reflected from the specimen can be observed and recorded after it has passed back through the Nipkow disk pinholes. Several thousand points on the specimen are simultaneously illuminated by the disk achieving, in effect, several thousand confocal microscopes, all running in parallel. Spinning the disk fills in the spaces between the holes and creates a real-time confocal image that can be directly observed with the naked eye, as with the standard microscope.

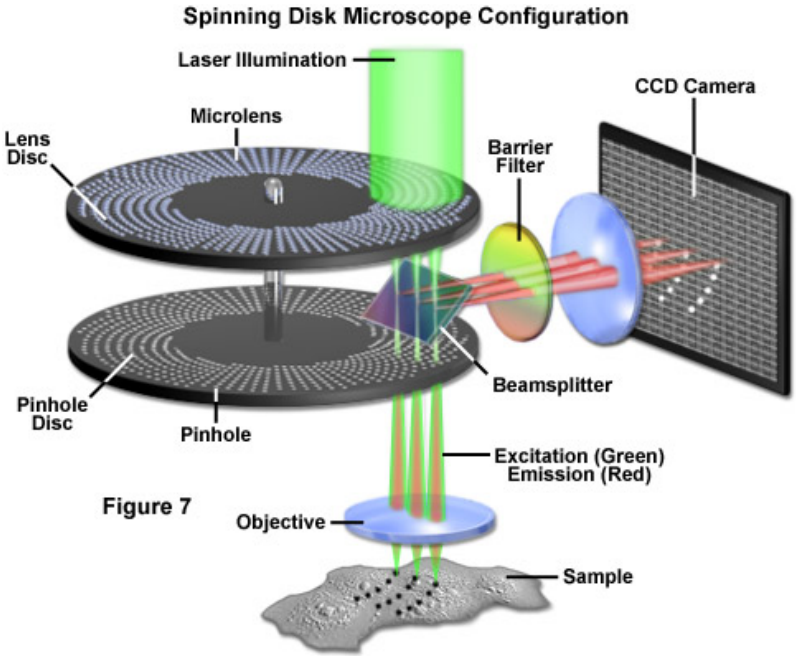

Figure 2.15: Spinning Disk Microscope Configuration
Source: Education in Microscopy and Digital Imaging - ZEISS.

An alternative to the Nipkow disk involves recent technology that offers high light throughput using a disk that is etched with a pattern of perpendicular slits, rather than pinholes, providing greater transmission while maintaining an acceptable level of confocality (Figure 7). Unlike the Nipkow-style disks, these slit-pattern disks are produced with varying slit widths that match different objective numerical apertures, magnifications, and specimen thicknesses. Thus, the slit disks enable confocal images to be acquired at high resolution using objectives ranging in magnification from 10x to 100x. Both spinning disk designs were developed primarily for live-cell imaging applications where a compromise exists between the needed increase in image acquisition speed versus a slight loss in axial resolution. Most spinning disk microscopes are illuminated with lasers or arc lamp sources and are coupled to sensitive electron-multiplying CCD cameras in order to image faintly fluorescent specimens.

Several manufacturers have introduced confocal systems using laser light shaped into a line, rather than a point, to scan the specimen, but with a substantial decrease in image acquisition time at

the expense of resolution (usually a factor of 1.2 in one dimension). Unlike the case with spinning disk microscopy, the degree of confocality can be controlled by the user by invoking changes to the line shape and size. Line scanning microscopes are used with CCD camera systems rather than photomultipliers and are generally much faster in acquisition speed than spinning disk or laser scanning confocal microscopes. In summary, there has been a tremendous explosion in the popularity of confocal microscopy in recent years, due in part to the relative ease with which extremely high-quality images can be obtained from specimens prepared for conventional optical microscopy, and its great number of applications in many areas of current research interest.

Figure [2.16] presents a z-projection of an osteosarcoma cell, stained with phalloidin to visualise actin filaments. The image was taken on a confocal microscope, and the subsequent deconvolution was done using an experimentally derived point spread function. Image Parameters Microscope: Zeiss LSM 780 Confocal Microscope Pinhole [m]: 23 μm Total Size-Width: 133.69 μm Total Size-Height: 134.91 μm Total Size-Depth: 6.48 μm Voxel-Width: 42.0 nm (pixel size) Voxel-Height: 42.0 nm (pixel size) Voxel-Depth: 80.0 nm Resolution: 23.5938 pixels per micron Zoom: 1.0 Objective: Plan-Apochromat 63x/1.40 Oil DIC Numerical aperture: 1.40

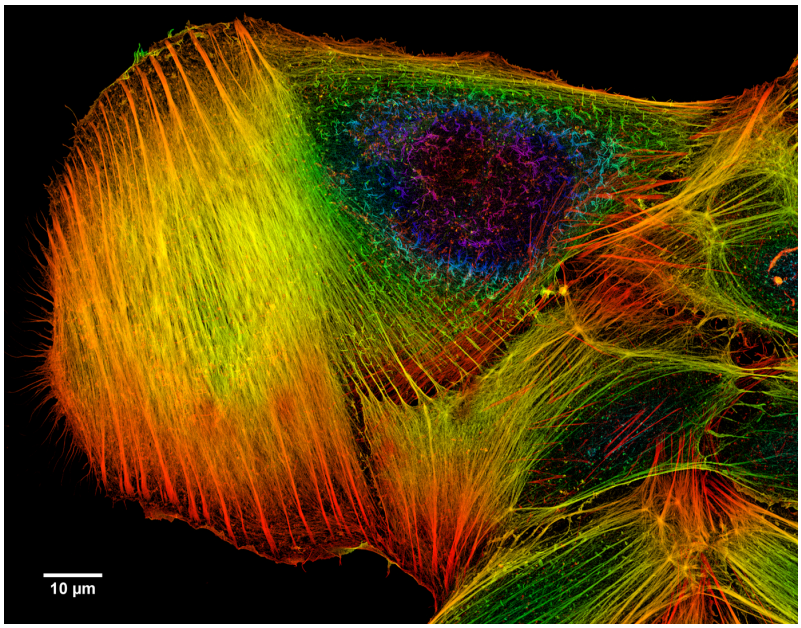

Figure 2.16: Confocal Colour coded image of actin filaments in a cancer cell
Source: wikipedia.org

2.2.3 Super resolution microscopy

The spatial resolution of a microscope describes its ability to distinguish detail in a specimen and is typically expressed as the minimum distance that two objects can have and still be perceived as two individual entities.

In conventional microscopes, the resolution is defined by the numerical aperture (NA) and the wavelength of light. Considering an ideal setup, in wide-field microscopy the resolution is almost half the wavelength of light used and can be up to 200nm. This theoretical limit is also comparable to that of confocal microscopes, although not always feasible as experimental limitations and the properties of the specimen itself might induce additional constraints.

When examining a system that consists of multiple optical elements, its optical characteristics can be conveniently described by the following three measures:

- Point Spread Function (PSF)
- Optical Transfer Function (OTF)
- Modulation Transfer Function (MTF)

Point Spread Function The Point Spread Function corresponds to the Impulse Response of an optical system. This essentially describes the system's transfer function when imaging a point source. In practice, images produced by an optical system are the convolution of its Point Spread Function with the actual object that is observed, as depicted in Figure [2.17]. The degree of spreading of the PSF - typically measured as the Full Width at Half Maximum (FWHM) - can be used to determine the axial resolution of an optical system. It can be therefore considered as an objective measure of a system's quality in that regard. The PSF can be symmetrical on all imaging axes, or non-symmetrical, and may also vary depending on the position in the object plane, or not - in which case it is called *shift invariant*. The Point Spread Function is also notably used in deconvolution, in order to reduce out of focus light or blur, something that is commonly used in 3D wide field imaging.

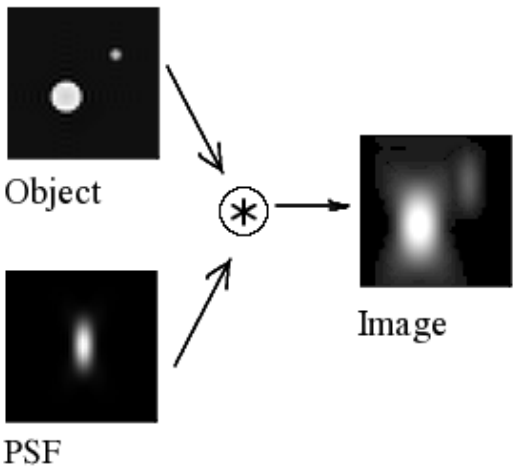

Figure 2.17: Image formation in a confocal microscope: central longitudinal (XZ) slice. The 3D acquired distribution arises from the convolution of the real light sources with the PSF
Source: en.wikipedia.org

Optical Transfer Function The Optical Transfer Function describes a system's response to different spatial frequencies. Fundamentally, this transfer function is the Fourier Transform of the PSF and is therefore complex-valued in principle. In case of an isotropic PSF, namely a Point Spread Function that is symmetric about its centre, the OTF is real valued. The Optical Transfer Function essentially describes the system's response to a periodic sine-wave, both in magnitude and phase, as a function of the wave's period or frequency. In an ideal diffraction-limited imaging system with a circular pupil, the magnitude of the real part of the OTF gradually decreases until it becomes 0 at the diffraction limit. Figure [2.18] depicts such a system, where its OTF and images of a point source and a spoke target can be examined. It is also important to notice how resolution and contrast are greatly reduced as the spatial frequency increases, especially when the system is out of focus.

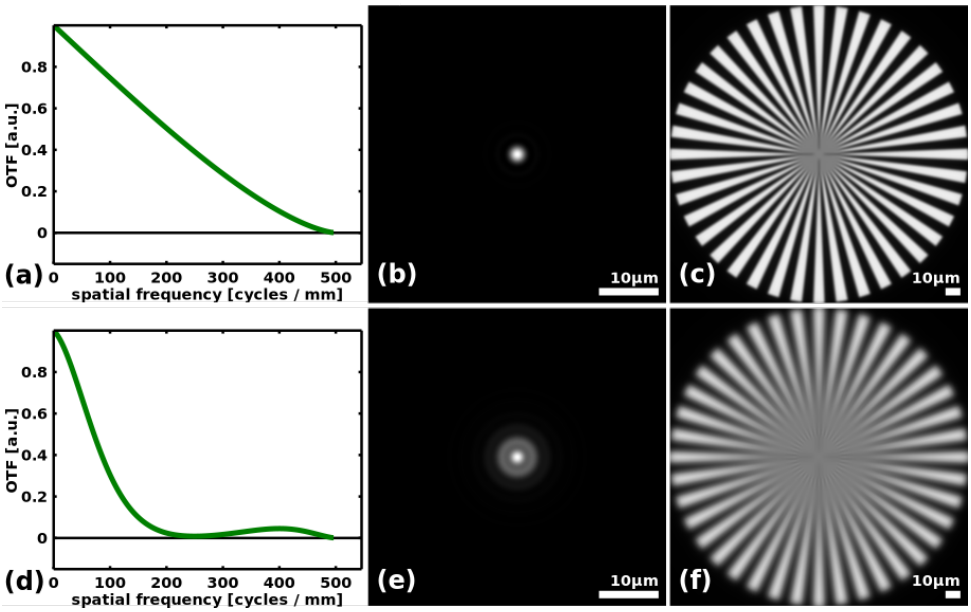

Figure 2.18: Illustration of the Optical Transfer Function (OTF) and its relation to image quality. OTF and images of point source and spoke target in well-focused (top) and out of focus (bottom) imaging system without aberrations

Source: en.wikipedia.org

Modulation Transfer Function The Modulation Transfer Function is another metric very similar to - and in several cases equivalent with - the Optical Transfer Function. The MTF again describes a system's response to a periodic sine-wave pattern as a function of its spatial frequency, although it neglects phase effects. It is formally defined as the magnitude of the OTF. The Modulation Transfer function is commonly preferred as a metric when comparing different optical systems, as it essentially encapsulates information both for resolution and contrast. Contrast (or modulation) practically defines how well the minimum and maximum intensity values of an observed object are transferred to the image plane and is typically examined along with spatial resolution in order to determine a system's quality, or suitability for a specific application.

High Resolution Imaging in Wide Field Microscopy In high resolution microscopy and tomography, especially with wide-field microscopes, resolution comes at the expense of greatly reduced depth of field. This means that information inside the focal plane can be captured with improved resolution and sharpness, whereas information outside the focal plane quickly becomes blurred and less defined. Therefore, in order to achieve high-resolution imaging across the specimen, many images have to be acquired - each at a different focal plane along the optical axis - and then combined to construct the final image. The step between each acquisition has to be calculated according to the depth of focus of the point-spread-function, in order to avoid under sampling. The set of images corresponding to the different focusing settings is typically referred to as "*z-stack*".

For the composition of the final image, one has to extract the in-focus information from each image of the z-stack and eventually combine all useful information into a single (2-Dimensional) image.

Over the years and while trying to achieve better contrast to facilitate imaging for various applications, a number of microscopy techniques has emerged trying to overcome the theoretical limits of conventional microscopes.

Phase contrast imaging is one characteristic example, where minor changes in phase result in noticeable variations in magnitude on the image plane. This microscopy technique is especially suitable when observing living cells in culture, although edge features can be significantly distorted and image quality can be heavily affected by floating debris and out of focus objects. Phase Contrast is also not suitable for thick specimens.

Polarized Light Microscopy Polarized Light Microscopy encompasses a number of techniques utilizing polarized light to enhance contrast and resolution. The illumination light is polarized, according to which certain polarizations can then be selectively rejected by the receiver. Such techniques can be especially useful in birefringent specimens, namely samples whose refractive index varies depending on the polarisation and propagation direction of illuminating light, where the strong interraction with polarized light creates increased contrast with the background. A typical example of Polarized Light Microscopy is Differential Interference Microscopy.

Differential Interference Microscopy (DIC) is a technique that is trying to amplify thickness and refractive index variations across the specimen, by utilizing plane-polarised light and light shearing prisms. DIC is especially useful when examining thick plant and animal tissues, as it enables optical selection of a thin slice due to the decreased depth of focus at wide aperture.

A big advantage of Wide Field Microscopes is that all of the aforementioned concepts, along with Bright Field, Dark Field, Light Sheet and Fluorescence Microscopy can inherently be performed by the same system, requiring little to minor setup changes. Addressing the most important limitations of Wide Field microscopy can therefore lead to the creation of highly versatile multi-modal systems, capable of performing a number of microscopy techniques, suitable for a wide variety of applications.

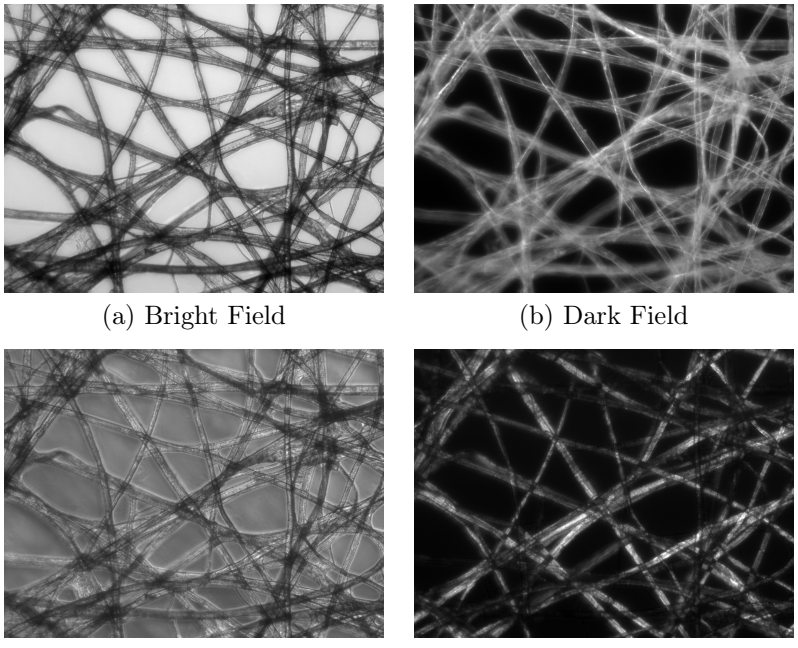

(a) Bright Field (b) Dark Field

(c) Phase contrast (d) Crossed Polarized

Figure 2.19: Comparison of transillumination techniques used to generate contrast in a sample of tissue paper using Wide Field Microscopy
Source: en.wikipedia.org

High Resolution Imaging in Confocal Microscopy Confocal Microscopy typically offers better spatial resolution than conventional wide-field microscopy. Confocal microscopes utilise a pinhole to reject out of focus light and can accommodate depth of field selection, therefore providing sharper and more accurate representations of the observed object. This effect can be exploited by drastically reducing the pinhole aperture, thus improving the specific Signal to Noise Ratio corresponding to the features of interest, which comes at the expense of lower signal levels and increased time required to perform a complete raster scan of a specimen.

Spinning disk confocal microscopes can provide close to real time imaging with very good spatial resolution by simulating the presence of thousands of small confocal microscopes on the spinning disk. Several confocal microscopes have also employed *galvanometer* scanners to expedite high-resolution fluorescence imaging by increasing photon efficiency. In practice, most of the high resolution techniques used in confocal microscopes can significantly improve image quality, although at the same time they require higher levels of light excitation than wide field microscopy - thereby increasing the effects of photobleaching and phototoxicity. They are therefore less suitable for examining dynamic events, or facilitating high-speed multi-dimensional microscopy and extracting temporal information.

Deconvolution Microscopy Deconvolution is a technique typically used in light microscopy to achieve sub-resolution imaging, even in 3 Dimensions. It is a computational restoration method trying to map diffracted light back to its original location in space, utilising deconvolution and the information derived by the system's Point Spread Function. The determination of the PSF and overall system's optical characteristics is crucial for this method's performance. The overall purpose of deconvolution is to improve the Signal to Noise Ratio and various algorithms have been developed to achieve this goal [14].

This method can be applied in Bright Field, Light-sheet, Dark Field and Fluorescence Microscopy, as well as Confocal and Electron Microscopy, conveniently improving resolution and structural analysis. Its computational efficiency even enables 5D Microscopy, capturing all 3 spatial dimensions, with temporal information as the 4th dimension and spectral information as the 5th - according to the excitation light's wavelength. While Deconvolution Microscopy is very promising in theory, in practice its performance greatly depends in the quality and space variance of the PSF, as well as noise and the calculation of aberrations and the system's optical characteristics.

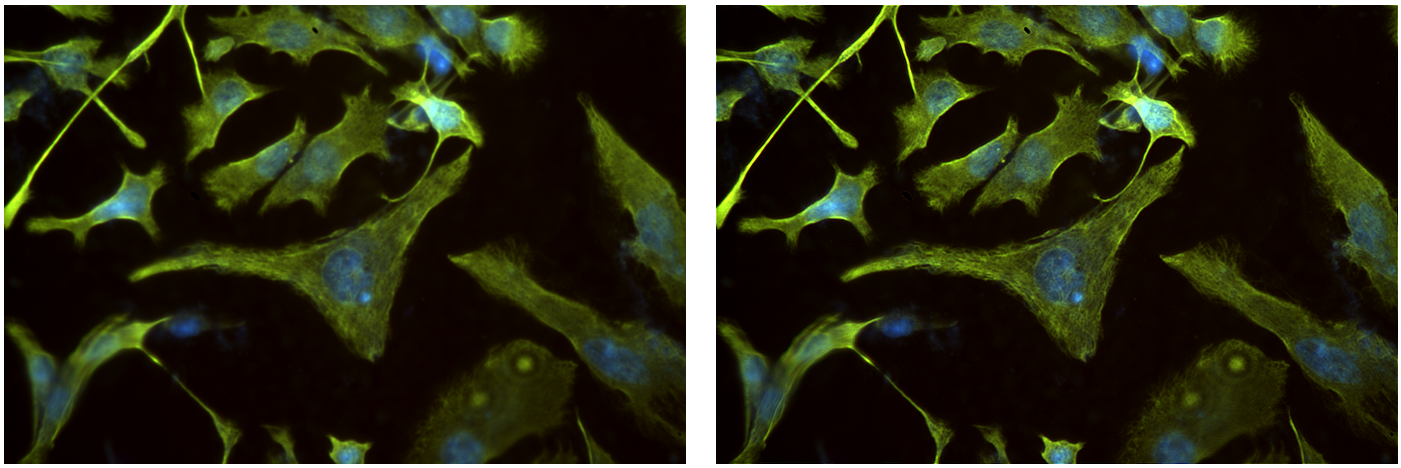

Figure 2.20: Widefield fluorescence microscopy from Spectricon's Lumnia Fluorescence Microscope. before (left) and after (right) deconvolution.
Source: Spectricon

2.3 State of the Art Microscopy

Microscopy, evolving through time, has reached a state of observation experience, that enables real time multidimensional imaging with different imaging modalities. The technological advances in electronics, optics and illumination, have given microscopy the chance of introducing itself to the new era of advanced instrumentation.

Fully controlled and optimized microscope parts, provide advantages in automation of calibration, data acquisition and processing. Data created out of observation of a single imaging region, are growing in multidimensional and complex structures. After intensive processing, these structures transform into images with extraordinary detail. Even the concept of automated diagnosis and image enhancements, with the use of Artificial Intelligence and/or advanced computational methods, is possible due to the evolution and reduced cost of state of the art hardware for machinery construction.

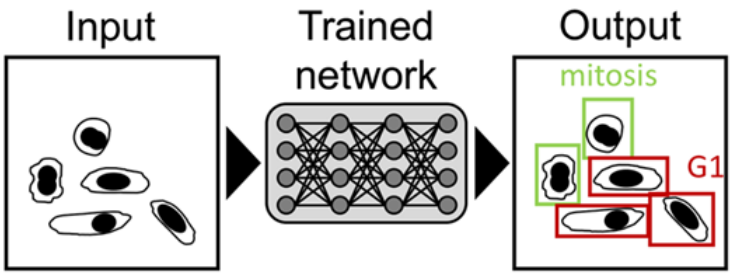

Figure 2.21: AI Diagnosis

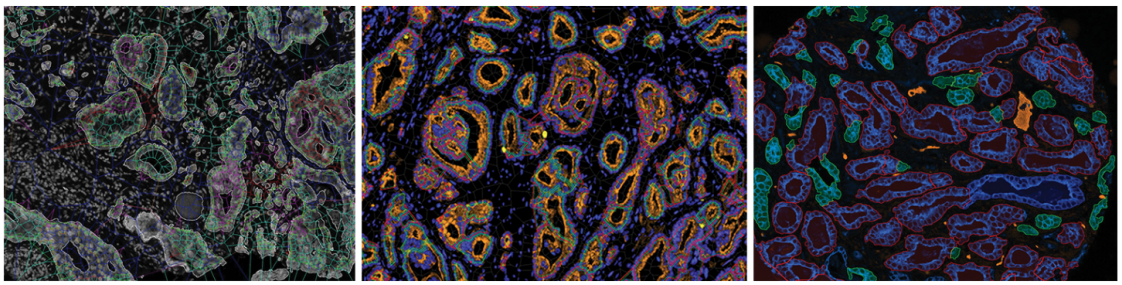

Figure 2.22: Prediction Prostate Cancer Progression with the use of Artificial intelligence. Source: https://www.the-scientist.com/features/artificial-intelligence-sees-more-in-microscopy-than-humans-do-65746

In Figure [2.22], the normal prostate contains microscopic glands that appear as ring-like or circular structures (grey in leftmost image). Artificial intelligence (AI) based methods, including deep learning approaches, are able to identify abnormalities in these and other structures to predict clinical outcomes from histological images of prostate cancer. In the right image, red is used to highlight complete ring structures while green denotes abnormal ring fragments indicative of cancer. This information can be used to predict the cancer's grade, a measure of disease severity. AI techniques can also evaluate levels of the androgen receptor (blue in center image), which, when present and activated, drives tumor growth and cell proliferation (bright yellow).

2.3.1 Advanced Multi Modal Microscopy

The term *advanced-microscopy* generally refers to the host of techniques that allow visualisation with resolution in the submicron to nanometer scale. This level of detail enables the study of biomolecular structures, interactions, and mechanisms of catalysis at the fundamental length scale of proteins, lipids, amino acids, glycans, and other biomolecules. To that end, the advantages of advanced-microscopy techniques makes them especially suitable for biomedical imaging.

Advanced Super Resolution Super-resolution microscopy, is based on a series of techniques in optical microscopy that allow images to have greater resolution than the imposed by the diffraction limit, which occurs due to the diffraction of light. Many techniques that rely on far-field fluorescence observation, are able to slightly improve resolution (up to about a factor of two) beyond the diffraction-limit. Some notable examples of this are confocal microscopy with closed pinhole or aided by computational methods - such as deconvolution or detector-based pixel reassignment - the 4Pi microscope, and structured-illumination microscopy technologies like SIM and SMI.

The methods for advanced super-resolution microscopy in the far-field that can improve resolution by a much larger factor, can be conveniently classified in two major groups:

- **Deterministic super-resolution:** Techniques of this class exploit the nonlinear excitation reponse of fluorophores - the most commonly used emitters in biological microscopy - as a means to enhance resolution. Such methods include STED, GSD, RESOLFT and SSIM.
- **Stochastic super-resolution:** Methods in this category take advantage of the complex temporal behaviour of molecular light sources - induced by the underlying chemical complexity-. This characteristic can be used to make several nearby fluorophores emit light at separate times, thereby becoming resolvable in time. Notable examples are Super-resolution optical fluctuation imaging (SOFI) and all single-molecule localization methods (SMLM), such as SPDM, SPDMphymod, PALM, FPALM, STORM, and dSTORM.

Fluorescence microscopy and its advances are leading the evolution of super resolution microscopy. The fundamentals of these new techniques, are optics and image processing based on the PSF Deconvolution. Advanced microscopy techniques are developed for specialized microscope applications, where specific characteristics of observation determine the system's functionality and implementation. Such methods are mostly tailored to specific applications, and despite being significantly competent in the prescribed tasks, are often incompatible with changes in observation strategy. Consequently, modularity and expansion of these systems are bound by several constraints, especially when used in a routine state and in requiring an update. Figure [2.23] presents a Lattice Light Sheet Microscope and its complex illumination design.

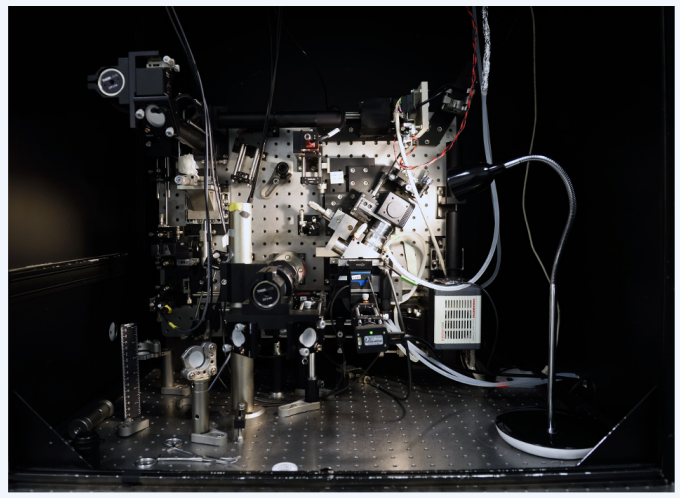

Figure 2.23: Lattice Light Sheet Microscope
Source: https://www.viennabiocenter.org/facilities/advanced-microscopy/

Multimodal Imaging Over the recent years, a wide range of optical imaging modalities based on different contrast mechanisms have emerged. The motivation behind this tendency is that a single technique is often unable to provide all of the required information, given optimal temporal and spatial resolution. Complementary techniques are needed to achieve a full understanding of the structural and biochemical changes that occur in cellulosic materials as they undergo physical, chemical or biochemical processing.

While many of these techniques are utilised in biological research and medical applications, the combination of different techniques can be a key factor in unlocking their full potential. However, the integration of different imaging modalities is often challenging, mostly due to the varying hardware requirements. The need for rapid evolution in microscopy can be fulfilled by developing technologies, focused on integrating multiple imaging modalities and exploring applications of these techniques.

A notable example of modularity in microscope systems is the Multimodal NLO microscope, as shown in Figure [2.24].

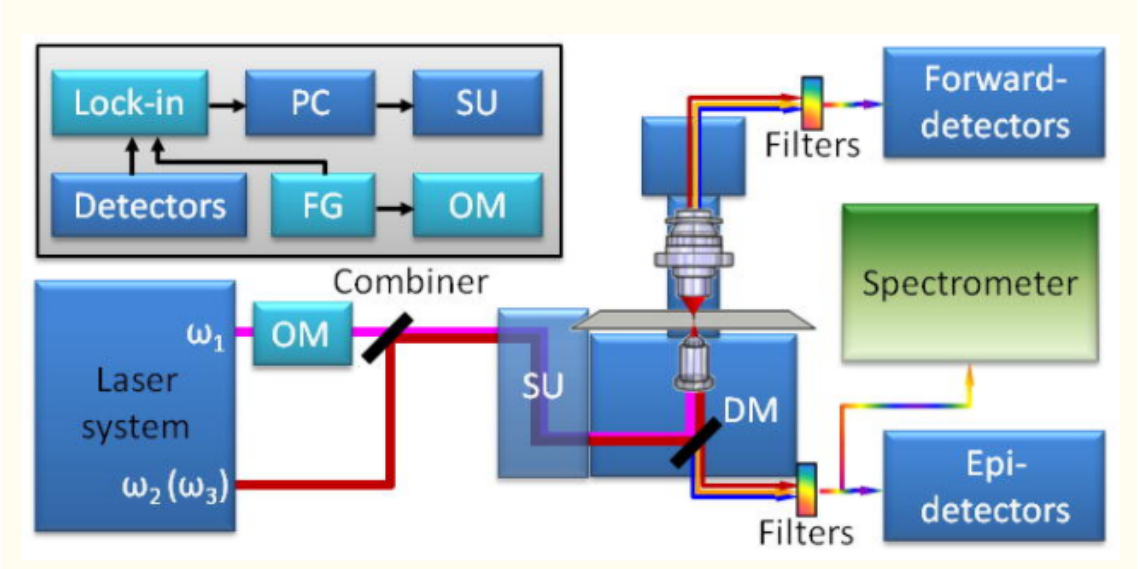

Figure 2.24: Multimodal Imaging system
Source: https://www.ncbi.nlm.nih.gov/pmc/articles/PMC3863942/

In the above image, $\omega 1$ and $\omega 2$ are pump and Stokes beams used for CARS and two-beam modalities, respectively. $\omega 3$ is a longer wavelength (lower frequency) beam available in OPO based laser systems ($\omega 1 > \omega 2 > \omega 3$). OM is an optical modulator, SU is a scanning mirror unit. DM is an exchangeable dichroic mirror. The inset shows the connections between electronic components for phase sensitive heterodyne detection. Lock-in is a lock-in amplifier, PD is a photodiode, PC is a computer, FG is a function generator. The blue colored components are used for modalities with homodyne type of detection. The light blue color represents components required for modalities with heterodyne detection. The spectrometer is a part of compound Raman modality.

Another example of a multimodal microscope, is an integrated microscope that can perform structural and functional imaging of cells in 3-D and for extended periods of time. This system combines optical coherence microscopy (OCM), multi-photon microscopy (MPM), and second harmonic generation (SHG) microscopy in a single instrument. Spectral-domain OCM data provides structural information based on the optical scattering from the sample, without the need for exogenous contrast agents to label structures. MPM provides functional information by using auto fluorescence, exogenous fluorophores or genetically-expressed fluorescent proteins that are linked to cell function or physiology. With simultaneous acquisition, perfect image registration is possible, providing spatiotemporal relationships between cell and tissue structure and function.

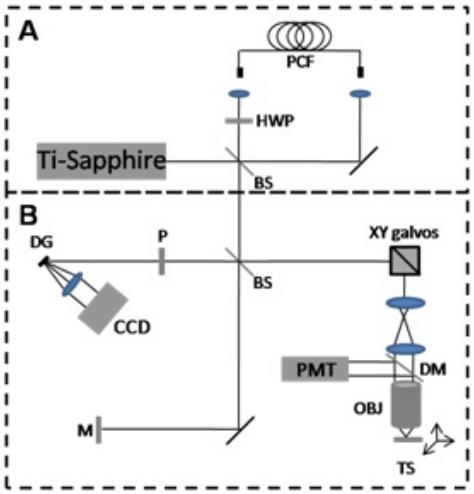

Figure 2.25: Multimodal Imaging system
Source: https://biophotonics.illinois.edu/?q=research/multimodal-imaging

Experimental setup of the integrated spectral domain optical coherence and multiphoton microscope. Region A is the dual spectrum laser source while region B is the microscope. Abbreviations: BS, beam splitter; DG, diffraction grating; DM, dichroic mirror; F, emission filter; HWP, half-wave plate; M, mirror; MMF, multi-mode fiber; OBJ, objective lens; P, polarizer; PCF, photonic crystal fiber; PMT, photomultiplier tube; TS, translation stage.

Multimodal analysis is powered by the concept of integrating multiple techniques in a single microscope. The unique configuration an integrated microscope enables simultaneous acquisition of both anatomical (structural) and functional imaging information, with particular emphasis for applications in the fields of tissue engineering and cell biology, as shown in Figure [2.26].

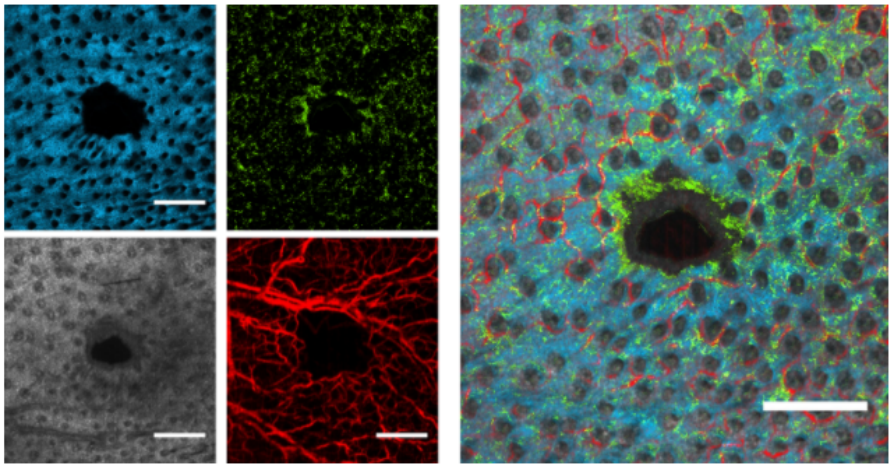

Figure 2.26: Multimodal Imaging using MPM and OCM on an open wound
Source: https://biophotonics.illinois.edu/?q=research/multimodal-imaging

The primary advantage of multimodal microscopy over other imaging techniques is its suitability for high-content real time imaging. This ability enables high resolution visualization which is of great interest for both biological research and medical practice. Multimodal microscopy is able to produce very accurate, multi dimensional data structures of specimens, with the use of simple techniques. The resulting information, given proper processing, can clearly compete with datasets from specialized microscopes in terms of reliability, while also greatly eliminating restrictions in construction and analysis specialization.

2.3.2 Automated Microscopy

State of the art Microscopy, as described previously, is capable of ultra high resolution observation in a single imaging region at a time. An analyst that needs to examine a big area of a specimen with high magnification and high resolution techniques, would probably have to spend a lot of time and effort, highly concentrated at each imaging region in order to extract results non biased by the human factor.

Modern-day microscopes, whether they are research-based microscopes or point-of-care microscopes, have a wide array of components that can be automated. Shutters, filter wheels, stages, light sources, and focus control can all be replaced with versions that are electronically controlled. However, assembling a fully automated optical imaging system that performs optimally is an extremely complex task that can be highly demanding. Getting the setup right requires expertise, experience in optics and electronics, and a big investment of time.

Some of the most important microscope components that can be automatically controlled are presented:

- **Focus Control:** Focus motors are connected to the fine focus transmission gear set of a microscope stage to enable automated focus control through the image acquisition software. These motors perform manual focusing in many advanced microscopes, too, so there is no mechanical coupling between the user control and the stage.

- **Stage Control:** Motors can also control the stage in the x- and y-axes. This extension enables the ability of positioning the system in different imaging regions without any mechanical coupling between the user control and the stage. Especially helpful for automated scanning.

- **Illumination Sources:** Light sources for widefield microscopy include tungsten-halogen sources for transmitted light, arc gas lamps for fluorescence excitation, while various kinds of lasers are used for confocal applications. The metal-halide lamp and LED sources are often used as a replacement for the mercury arc-discharge lamp. Light source selection can be done by the user through direct manual intervention or using controls available by the software. In advanced systems, the software can switch between light sources in pre-determined sequences.

- **Shutters:** Electromechanical shutters block the light sources from illuminating the specimen between camera exposures, and they are especially essential when imaging fluorescent or live specimens to minimize photobleaching and phototoxicity. They are also used to select between multiple light sources and pathways, in some cases in rapid mode, for example, to gather two images per time point in time-lapse sequences. Automated high-performance shutters are microprocessor controlled and are interfaced with a computer to coordinate their operation with other parts of the microscope.

- **Wavelength Selection:** Wavelength selection can be effected through various devices, such as multiple filters, beam splitting units that direct light through several pathways, monochromators, or acousto-optic tunable filters (AOTFs). While manual switching is slow and requires constant user intervention, automatic switching enables the user to achieve rapid switching between the desired wavelengths and schedule those experiments in the user's absence. Wavelength selection can be done manually, either by direct selection or by actuation of a control mechanism, or it can be done by the software in a pre-programmed sequence.

- **Camera/Detector System:** The user can control the operation of the camera or detector through the use of the software. Software-control can be applied for image collection in the absence of the user.

An automated microscope system can be pre-set to record images in time-lapse or x-y-z scanning mode, in the absence of the user. The desired spectral profiles of the fluorophores, the exposure time, gain and threshold can be selected or be automated entirely.

In confocal or deconvolution microscopy, Z-stack settings can be stored in memory and applied to the desired fields. Images for each field can be acquired with the settings selected for the particular field, and these settings can be different from one field to another. Storage of coordinates allows return of the motorized stage to the individual fields at the appropriate time intervals while autofocusing protects from focus drift over time, something especially important for live specimens and area scanning.

When both large fields of view and high resolution is required, the solution is given by tiling the microscope. The software guides the system to acquire the desired number of neighboring fields that will then be automatically stitched to one large field of view. Meta-data and label storage allows proper archiving of the data, with replication of exact imaging conditions, when desired.

State of the art advanced automated microscopy yields two basic designs.

- A modular design, specialized in high resolution multidimensional analysis of a small area, using a variety of different imaging modalities. Usually this design is used for research and education. Figure [2.27] presents a modular automated microscope DSX1000 made by Olympus, which is an All-in-One System with a Wide Magnification Range that implements High-Resolution Image at High Magnification, Long Working Distance Objectives and Multiple Observations techniques.

Figure 2.27: Olympus DSX1000 Digital Microscope
Source: https://www.olympus-ims.com/en/microscope/dsx1000/high-end-model/

- A non modular design, specialized on scanning large areas with limited techniques based on the research field it applies to, usually used for specialized routine tasks. Figure [2.28] presents a non modular automated microscope NanoZoomer made by Hamamatsu, which is whole slide scanners that rapidly scan up to 360 microscope glass slides.

Figure 2.28: NanoZoomer S360 Digital slide scanner
Source: https://www.hamamatsu.com/eu/en/product/type/C13220-01/index.html

Chapter 3

System Design

3.1 Introduction

As described in the previous section, Automated Microscopy and the evolution of the observation experience through multimodal analysis are key features for state of the art biomedical imaging and diagnosis. In this section we are going to present the Proposed System Design of our Modular Microscope Automation extension.

Histopathological analysis of biopsy or surgical specimen, requires inspection of hundreds of microscope's slides, is a common clinical practice for diagnostic purposes. Essentially, the process involves slicing the biopsy or surgical sample into very thin slices, placing them on glass slides and viewing them under microscopes. Predominantly, the placement, positioning, and view control is done manually by the pathologists in most of the clinics and hospitals. Because of this, the diagnosis remains heavily dependent upon the experience and performance of the pathologist.

Spectricon's Lumnia-FL Microscope For the purpose of this research, we gained access to Spectricon's Lumnia-FL multimodal Microscope, as shown in Figure [3.1]. The Lumnia microscopes are built upon an innovative modular design comprising a basic digital microscope platform and several add-on units. All Lumnia versions come with the Phenotype software suite, which is operated through a touch screen-based graphical user-interface.

Spectricon's Lumnia-FL Microscope is a fluorescence microscope having as critical part the the polyline light source (a diode laser array). The polyline is integrated as an attachment onto the basic microscope platform, providing narrow band and efficient fluorescence excitation.

Laser line excitation leaves sufficient spectral space for the imaging module to uncouple the emissions from multiple different fluorophores with overlapping spectra. The whole system is built upon an innovative design allowing for the real-time inspection of multiple fluorophores simultaneously and for the quantitative fluorescence intensity mapping.

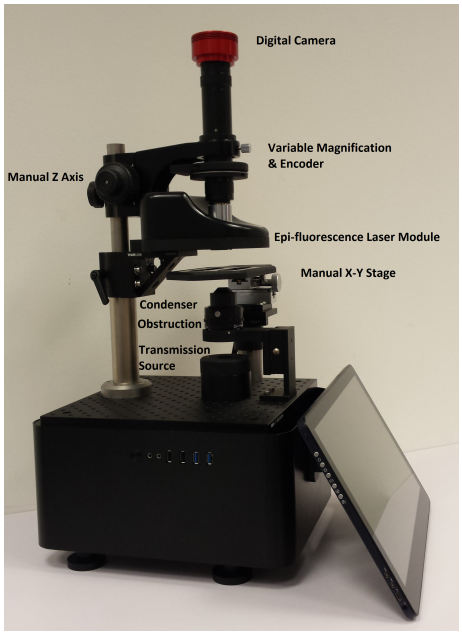

Figure 3.1: Spectricon's Lumnia-FL Microscope
Source: spectricon.com

Lumnia-FL microscope is a great tool for our research due to its modularity and multimodality. Some of the main features Lumnia-FL provides are presented.

- **PolyLine laser ring:** PolyLine laser ring enables multicolor fluorescence imaging. Lumnia-FL makes separate imaging of multiple fluorophores a routine-real time procedure, since laser lines consume only a small range from the imaging channel. This way full spectrum and true color imaging is enabled.
- **Controllable Light Sources:** Lumnia-FL offers both transmission and epi-illumination via its computer controllable light drivers.
- **Modularity:** With a working distance of 2.5 cm and a dual operation of both upright and inverted position, Lumnia-FL removes any limitations in sample volume. Mounting experimental tools and sample manipulators are possible by using the breadbord platform.
- **Phenotype-F Suite:** Control and synchronize laser excitation and imaging or view fluorescence images in a time-lapse mode. Using Phenotype-F Suite you can calibrate fluorescence intensity and perform flat-field correction for all laser lines enabling reliable fluorophore uptake mapping. You can also calculate fluorescence spectroscopy and excitation-emission matrices and display them for every image pixel.

Using this microscope and its extended software capabilities, we can configure different examinations, navigate manually through samples and capture images in different imaging modes with separate controls for each illumination mode, as shown in Figure [4.101].

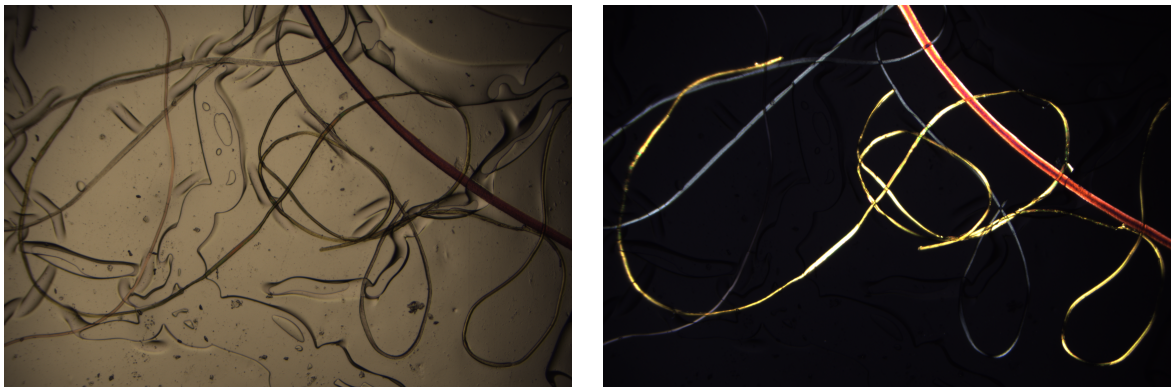

Figure 3.2: Lumnia-FL Imaging Modalities (a) Brightfield, (b) Multi Epi-Fluorescence

This microscope also offers more advanced features for Spectral Acquisition, Selective Excitation/Emission (Ex/Em) Overlay Maps and Intensity Maps that produce specialized data structures for research and diagnosis, as shown in Figure [4.102].

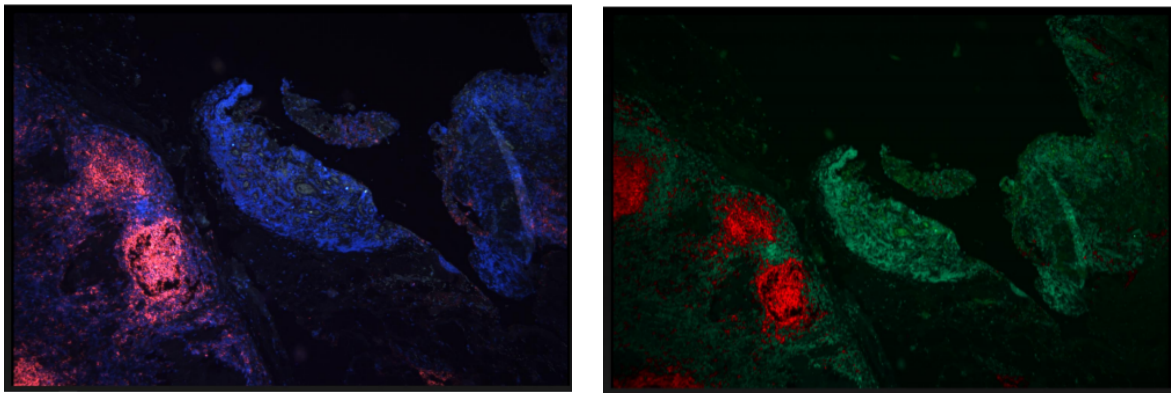

Figure 3.3: Lumnia-FL Imaging Advanced Modalities (a) Multi Epi-Fluorescence, (b) Selective Ex/Em Overlay Map (Emission: Green[510-575] + Red[640-...])

3.2 Proposed System Design

The proposed system of our research is an easy to install and use motorized extension for digital microscopes. We aim to fully control and automate the mechanical and optical parts of a microscope, with which the specialists interact the most. This will result to a microscope extension that can scan and analyze the given samples with various techniques with minimal human interaction. Finally, the outcome will be presented to the specialists for their research. Motorization of the most used parts of a microscope is essential and can lead to a comfortable and relaxing imaging experience compared with the classical microscopes usage, as shown in Figure [3.4].

Figure 3.4: (a) Standard microscopy, (b) Advanced Automated Multimodal Microscopy

Full motorization will lead to an overall increase in throughput due to the automation of several imaging techniques. Moreover, operator skill requirements will be reduced, as the system can be set up through software, allowing for a simplified interface and use. This also improves the repeatability of image capturing and measurements between operators at varying skill levels.

Automated procedures like focusing and slide scanning can benefit the specialists from different aspects. By reducing the contact with the samples it is possible to perform a better analysis, minimizing alterations in the results and other risks. These automated procedures will contribute to increase the number of techniques to be illustrated at the same time, that is always a tedious task. Overall, such a system is very useful in terms of comfort, speed, more accurate data analysis and image processing techniques that will give a different perspective in the way we observe and analyze the samples. In fact, an automatic system will provide a way to improve diagnostics reducing the time, required for the analysis. [8]

3.2.1 Hardware Segmentation

In terms of Hardware, such a system can be constructed by utilizing various components regarding the movement, magnification, light and sample digitization. In our research we will focus on the following.

- **High Resolution Motorized XY Linear Stage**

  A motorized XY linear stage assists on moving the microscope's sample with great accuracy and repeatability. Moreover, it enables the user to set and save location points of great importance, for return inspection. By utilizing such a stage, the system can perform a large out-of-field-of-view image capture, through stitching, allowing for measurement of features

too large to be inspected in a single field of view. An automated geometric measurement at multiple point locations improves the sample acquisition speed, while minimizing the human element from the process, thus improving repeatability of the analysis.

- **High Resolution Motorized Z Linear Stage**

  A motorized Z linear stage enables controlling the focus of the microscope. This can lead to fast, accurate and repeatable camera height adjustments or even better to auto-focusing, that will provide a sharp image without the need of human inspection. This addition also enables the system to perform EFI (Extended Focal Imaging). This is done by capturing multiple Z focus images to generate all-in-focus images, 3D images and Z height or depth measurements. Another very useful utility, provided by a Z motorized linear stage, is the Focus map. This map is created when stitching in the XY plane by compensating for any sample drift in focus and so collecting the height data of each image.

- **Joystick with buttons**

  A Joystick and some buttons are used to interact with the motorized system. This is very important as the feel of the joystick does not require any skill to understand and it is subconsciously associated with the motorized motion. Moreover, customization of the user interface with the help of the joystick and buttons associated with it is of great importance.

- **Magnification Encoder**

  A Magnification Encoder provides feedback from the microscope's magnification unit. By using this information, the software can calculate the image dimensions in absolute values. This is very useful when the XY stage needs to make a move proportional to the image's real dimensions or when the Z stage produces the height map. This technique can also be achieved by using software image processing procedures that some times lack of accuracy.

- **Custom Light Sources**

  Custom designed light sources are crucial for controlling which technique the microscope will illustrate in the sample acquisition state. By utilizing various light sources, it is possible to extend the capabilities of any microscope to a multimodal scanning microscope with automated light conditioning. This means that the system can automate any procedure that needs different lighting conditions and also auto calibrate its processes' correlation with the peripherals.

- **Digital Camera**

  A digital camera provides the ability to capture, process and illustrate the sample in a high resolution digital form. Compared to the classic binocular techniques, which could only save and process images and results within human brains, we observe significant improvement in the imaging throughput and in the technical capabilities. With the digital camera the system will be able to utilize hardware and software to process and save images, maps and results with high accuracy and repeatability.

Overall, full motorization combined with digitization of the microscope's images and custom lighting will result in a powerful and autonomous system that can be programmed to execute specialized acquisitions with great accuracy and repeatability. By utilizing this hardware we are able to create a fast, ergonomic and accurate measuring instrument.

3.2.2 Software Segmentation

This microscope's Software has been constructed with the precious help of the engineers of Spectricon. Figure [3.5] presents the functional block diagram of this Automated Microscope's software.

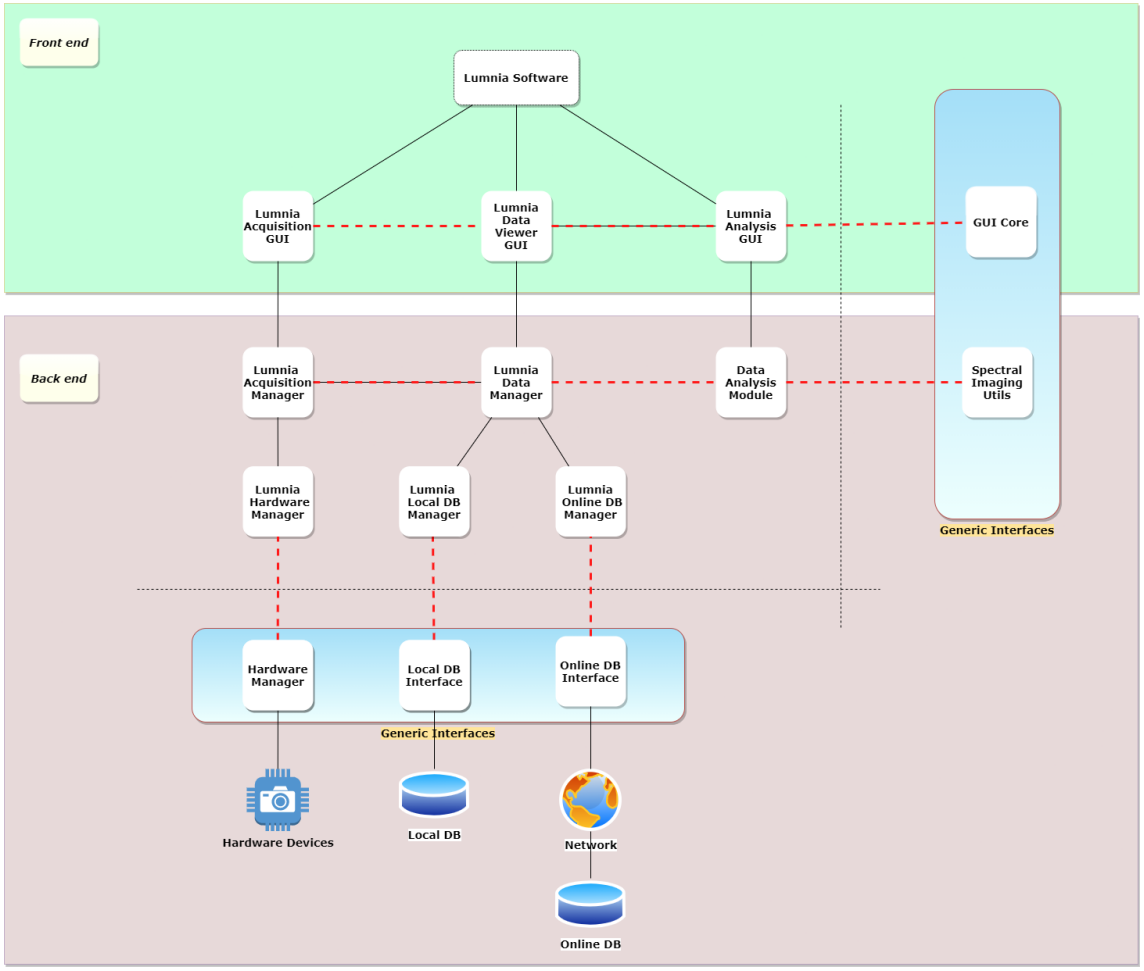

Figure 3.5: Lumnia Software Functional Block Diagram

This diagram presents the fundamental structure of the software of our system. We separately worked into the back end and front end by utilizing some generic interfaces for the construction. In terms of height, we observed the system's levels of operation from low to high.

In our research, we got involved to several fundamental structures of this software in order to enable the use of the motorized extensions through Spectricon's software. A brief description of these structures is presented.

- **Lumnia Hardware Manager**

  The hardware manager unit of the system provides all the low level mechanisms to communicate and control the various hardware components (motors, cameras, light sources, encoders and joysticks). The system recognizes the connected devices and builds up the utilities and software associated with them. Also, this unit provides the ability of utilizing x-y-z motors, encoders, joysticks and the GPU of the system for image capturing and processing. Each hardware device has to be treated separately from the system, because it has its own way of communication and timing. For these reasons a separate driver for each device is created, so mid level access to the hardware components is now available.

- **Lumnia Acquisition Manager**

  This manager, uses the mid level hardware access provided from the Hardware Manager to construct the specific acquisition techniques the microscope will implement. This unit can perform multi spectral and/or hyper spectral imaging, auto focusing acquisition, stitching acquisition and much more. While in these acquisitions, structures of data and images that delineate each case are created. In every capturing occasion, the output structure of this unit will be a fully described object for universal usage. This unit will utilize algorithms specifically designed either to measure application specific image characteristics or to produce real time data providing feedback to the hardware manager's controllers. By optimizing the processing of the data on the system's GPU, it is very efficient in calculating all the needed results for the sample's examination and system functionality.

- **High Level Functionality**

  The high level functionality of the system provides a wide variety of procedures that the system is capable of executing. By utilizing all the lower level software units, the system creates functions that combines them into complex and very useful software structures. These structures are the core of the system's functionality, as they can handle any occasion and task needed. Finally, their resources are already managed and optimized from the lower level designs so that the system offers a smooth real time experience.

- **Graphical User Interface (GUI)**

  The graphical user interface provides the ease of using a complex machine with simple and understandable structure and appealing appearance. It is always of great importance when designing a system, to work properly not only for users that always know how to use it and interact with it, but also for users that specialize in other scientific fields and can appreciate the machine's outcome from another perspective. That's why a well designed graphical user interface is essential for our system.

In conclusion, this system intents to give the specialists the ability to use a machine capable of executing all the tasks a classic microscope could also execute, but at the same time with the ease of speed, accuracy, repeatability, data management and automations without the human surveillance. Reading and loading the microscope's examinations from captured images, within microscope's software, setting up the system in the exact same configuration as when an image was captured and a lot of interesting stuff is now essential.

3.3 System Requirements

In Advanced Automated Microscopy systems, high resolution in each automated part is essential. From cameras to motors and encoders, these systems need to implement high precision calculations for each automated operation to occur as accurate as possible.

The acquired images need to contain as much detail as the high-resolution cameras allow, blurred content must be eliminated with high accuracy and thus, the accurate focusing of each of the captured images is of great importance. In addition to that, the collection of many segmented images, which form the sample(s) under investigation, need to be precisely matched and connected. To ensure a continuous, fast and smooth operation of digital microscope these processes need to be automated.

The requested functionality and the system requirements for this research are mentioned below:

- Hardware Requirements.
    1. X-Y Movement Resolution $<$ 10 µm.
    2. X-Y Movement Range $>$ 10 cm^2 ($\sim$ 4 microscope slides).
    3. Z Movement Resolution $<$ 1 µm.
    4. Z Movement Range $>$ 3 cm ($\sim$ working distance).
- Software Requirements.
    1. Scan and find the optimum focus for a given scene (Auto Focus).
    2. Verify if the captured image is focused and re-focus if needed (Absolute Focus Metric).
    3. Make a 2D full sharpness image reconstruction, from the captured z-stack images (Multi Focus Image Fusion).

There are three degrees of freedom according to the translation axes, namely X Y and Z. Focusing and z-stack fusion of the microscopes imaging region, are associated to the movement of the camera on the Z-axis. Precise positioning and potentially stitching of multiple images are associated to the X and Y axes.

Motors selection, motor-drivers design and hardware programming, are mandatory tasks for this project and already done, but they will be documented separately.

Chapter 4

Implementation

4.1 Introduction

In this chapter the implementation of the system is presented. The high level requirements, the proposed designs as well as the qualification and verification for each method are addressed. Our system is based on the Lumnia-FL pathology microscope that it is designed to analyze carcinoma histology specimens, as shown in Figure [4.100].

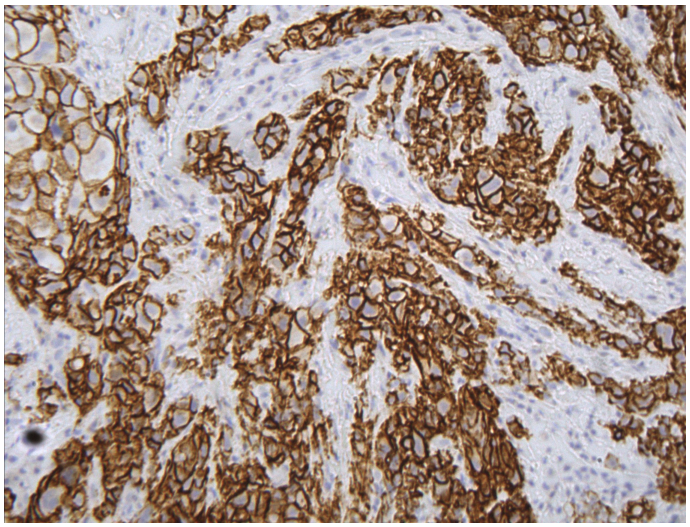

Figure 4.1: Pathology - Stained Tissue

The tissues analyzed with the techniques we are going to implement are usually stained with DAB and/or Hematoxylin stains. DAB, when applied to a tissue like this, is oxidized by hydrogen peroxide in a reaction typically catalyzed by horseradish peroxidase (HRP). The oxidized DAB forms a brown precipitate at the location of the HRP (usually in the membranes), which can be visualized using light microscopy.

Hematoxylin stain is one of the principal tissue stains used in histology. It is the most widely used stain in medical diagnosis and is often the golden standard. The hematoxylin stains cell nuclei blue, the stain shows the general layout and distribution of cells and provides a general overview of a tissue sample's structure. Hence, a pathologist can easily differentiate between the nuclear and cytoplasmic parts of a cell, which can be also visualized using light microscopy.

Visualization of these stains is already implemented by Spectricon with the use of their high end microscopes. The next step is automation in image acquisition data analysis.

Hardware Peripherals Selection First of all, the linear motorized stages are selected based on the system requirements specified in the previous chapter.

- **High Resolution Motorized X-Y Linear Stage**

  For the X-Y High Resolution Motorized Linear Stage which fulfils the system's requirements, we selected the **8MTF - Motorized XY Scanning Stage** by Standa, as shown in Figure [4.2]. This motorized Stage features Full Step Resolutions of 2.5 μm and can be driven up to 1/256 micro-stepping. In this setup the required micro-stepping is 1/16 or 0.156 μm per step. Moreover, this stage can handle speeds up to 10 mm/sec and has Horizontal load capacity up to 50 kg and Vertical load capacity up to 6 kg, as stated in Standa's datasheets.

Figure 4.2: High Resolution Motorized X-Y Linear Stage - 8MTF - Motorized XY Scanning Stage Standa

Source: standa.lt

- **High Resolution Motorized Z Linear Stage** For the Z High Resolution Motorized Linear Stage which fulfils the system's requirements, we selected the **8MT30-50 - Narrow Motorized Translation Stages** by Standa, as shown in Figure [4.3]. This motorized Stage features Full Step Resolutions of 1.25 μm and can be driven up to 1/256 micro-stepping. In this setup the required micro-stepping is 1/16 or 0.078 μm per step. Moreover, this stage can handle speeds up to 5 mm/sec and has Horizontal load capacity up to 5 kg and Vertical load capacity up to 3 kg, as stated in Standa's datasheets.

Figure 4.3: High Resolution Motorized Z - 8MT30-50 - Narrow Motorized Translation Stages
Source: standa.lt

The motorized stages and all the hardware parts (**Joystick**, **Magnification Encoder**, **Custom Light Sources** and **Digital Camera**) needed in order to construct a functional microscope, were provided by Spectricon.

This research is dedicated to the construction of the low level hardware, firmware and software structures for this modular setup. Specifically, we addressed the need for an ultra capable generic Motor Driver for our three axes. The additions to the current Lumnia-FL software are the motor drivers software implementation and the high level functionality that enables them to address several unsolved problems.

Implementation Segmentation The implementation of this research is divided into three stages.

- The first stage focuses on designing a Modular Motor Driver and its compatibility with the main system to fulfil our kinetic needs. The purpose of the first stage was to be familiarized with stepper motor drivers fundamental electronic structures and build one from scratch. Several designs were discussed and implemented with the help of Spectricon's engineers and therefore we constructed a new, innovative, design to fulfil our needs.
- The second stage focuses on designing a Focusing system that can robustly focus our setup in every occasion. The purpose of the second stage was to be familiarized with the image processing in order to extract useful data for our focusing application, and therefore use our motorized system to find the optimal focus plane of every imaging region. Several designs were implemented in order to address all the restrictions to accurately and efficiently focus our system.
- The third and final stage focuses on designing a Multi Focus Image Fusion technique for the microscope to provide full sharp 2D images. The purpose of the third stage was to be familiarized with the image processing using the z-stack of a single imaging region, in order to extract the out-of-focus parts of images and fuse them to an full sharp image. The z-stack acquisition procedure was held with the help of our precise motion controlled z axis.

In conclusion, in the following pages of this chapter, we are going to focus on the implementation of the respective stages.

A block diagram representation of the proposed system is shown in Figure [4.4].

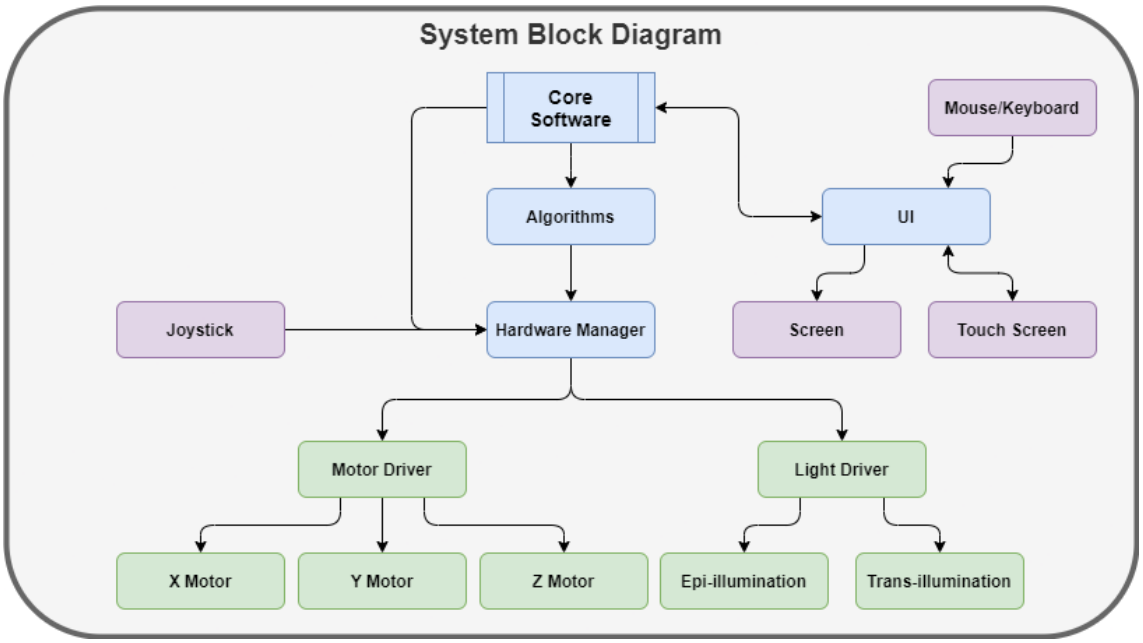

Figure 4.4: System Block Diagram

4.2 Motor Driver

The implementation of the various custom hardware devices used in this thesis took place in our laboratory. We designed all the circuitry and using microprocessors we developed the code structures, for each application, in *C* and *C++*. For the code design we used the Arduino Integrated Development Environment (IDE) and its Object Oriented Programming capability. Finally, the printed circuit boards design were accomplished by utilizing of Altium Designer software and custom techniques for the circuit board printing.

The Micro Controller Unit (MCU) The main processor used in our application is the ESP32 - Xtensa® dual-core 32-bit LX6 microprocessor. The dual core processing capabilities of this MCU combined with the FreeRTOS™ Real-time operating system and its Multitasking Fundamental, gave us a very powerful alternative instead of any other MCU in the market. We utilized the two cores of this MCU for the parallel execution of the device's independent functionalities and the tasks of each core for our object oriented design with Multitasking necessity. With this workflow, we achieved designing systems that communicate and execute commands in real time with high efficiency in both computational and power terms.

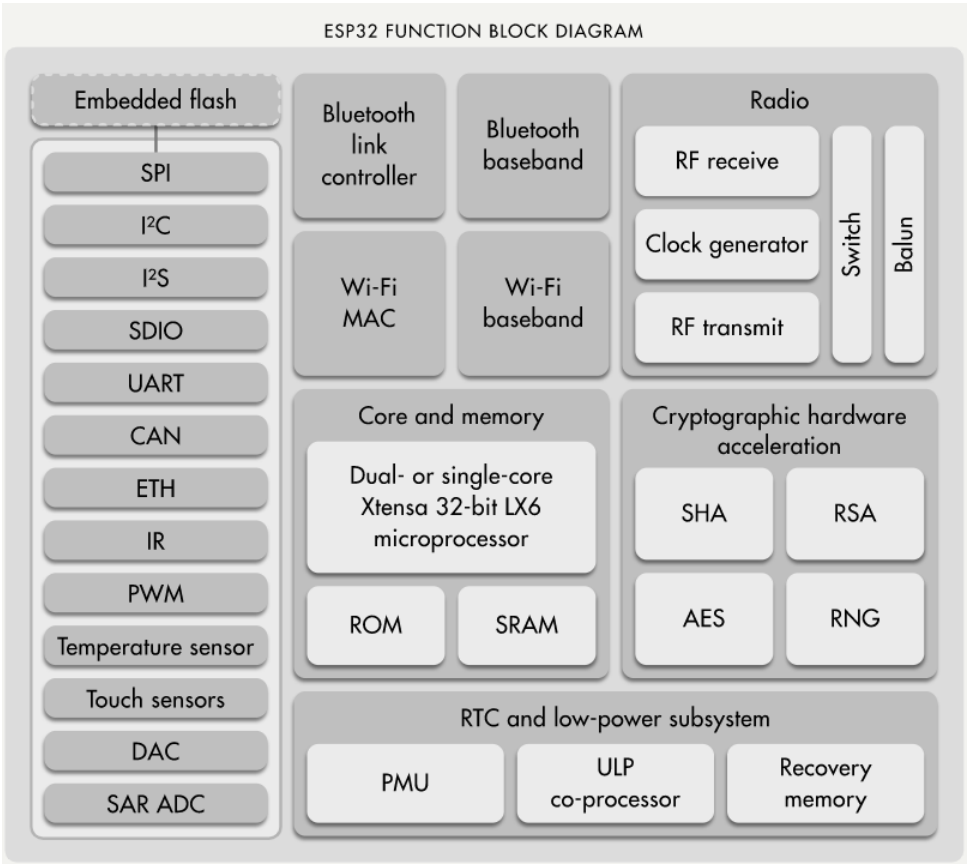

Figure 4.5: ESP32 Function Block Diagram
Source: esp32.net

We optimized our code with the help of the powerful and very fast cores of this System on Chip (SoC), running at 240 MHz, by utilizing only the needed blocks of it's functional block diagram [4.5]. This processor can be used for WiFi - Bluetooth - Radio communications, Cryptography, Low-Power applications and of course for Real-Time processing. Our main goal and the reason why we used this SoC is to implement independently the UART Communication (**Hardware Communication**) and the and fast GPIO manipulation (**Hardware Drivers**).

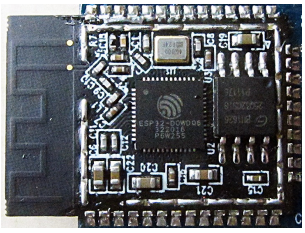

Figure 4.6: ESP-WROOM-32
Source: wikipedia.org

Hardware Segmentation Each hardware module of our system, is uniquely designed to accomplice it's own critical tasks. Each of driver types (motors, light sources etc.), share one important principle of operation, the Interpreter style of implementation. The idea is to design compact and light code for each machine, providing the ability of dynamically configuring its functionality. By doing so, the microprocessor will be "burned" with the firmware only the first time and then each high level software can set it up analogous of its application.

Motor Driver: For the motor driver module, we combined the ESP32 [4.6] with the TMC5160 motor controller. Additional external circuitry is used to ensure the correct power sequence of the driver and handling the system's interrupts with the help of the motor's linear stage limit switches. The principal of operation of a motor Driver like this, is design in order to efficiently and safely set up and operate a big variety of stepper motors.

- **ESP32 DevKit V1**
  The ESP32 chip comes with 48 pins with multiple functions. Not all pins are exposed in all ESP32 development boards, and there are some pins that cannot be used. The ESP32 DevKit V1 development board gives us access to 30 of the GPIOs of the ESP32 including, Capacitive touch, ADC, DAC, I2C, UART, CAN 2.0, SPI, I2S, RMII, PWM and more. Finally, with the CP2102 USB to UART Bridge this development board provides a complete plug and play interface solution that includes royalty-free USB drivers.

Figure 4.7: ESP32 DevKit V1
Source: espressif.com

- **TMC5160**
  The Watterott's TMC5160 SilentStepStick version with the external transistors is a powerful stepper motor controller specializing on high dynamic and high torque while handling up to 3A (RMS) continuous coil current. Based on Trinamic's SpreadCycle™ and StealthChop™ choppers, this driver ensures absolutely noiseless operation combined with maximum efficiency and motor torque.

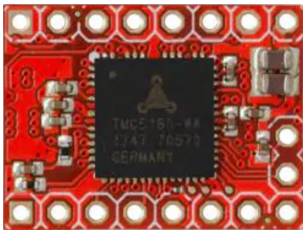

Figure 4.8: TMC5160 Driver
Source: watterott.com

- **Power Sequence Peripherals**
  The power sequence of the TMC5160 [4.8] is controlled with the help of, a power Relay, a Power Switch IC (TPS22919) and two Adjustable Switching Regulators (PTN78000). The Relay is responsible for providing power to the power MOSFETS, whereas and the Power Switch IC to the logic circuitry of the TMC5160. The Adjustable Switching Regulators provides stable 5V for the logic circuitry to operate and 12V to an external fan for cooling.

The block diagram of Figure [4.9], silhouette the system's setup and integration.

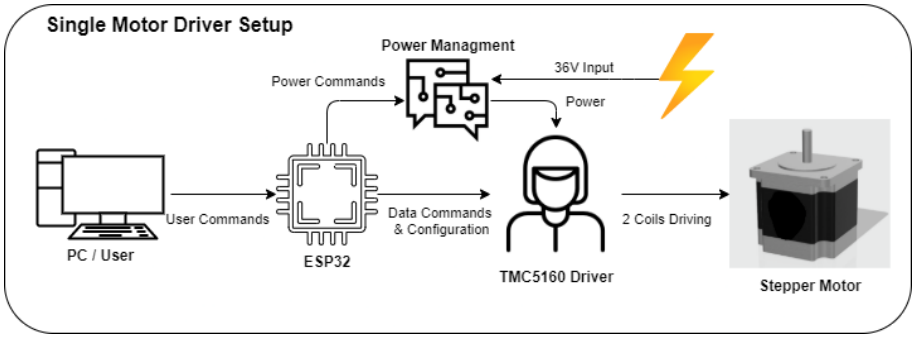

Figure 4.9: Motor Driver Peripherals

4.2.1 Circuitry

Creating our own Motor Driver PCB was created by utilizing the Altium Designer Software. Altium Designer is a PCB and electronic design automation software package for printed circuit boards.

Single Axis Design A single channel Motor Driver was built to prove the principal of operation of our design. Finally, after debugging the Driver we finalize the **Single Channel Motor Driver Schematic** design like shown in the figures [4.10, 4.11, 4.12] below.

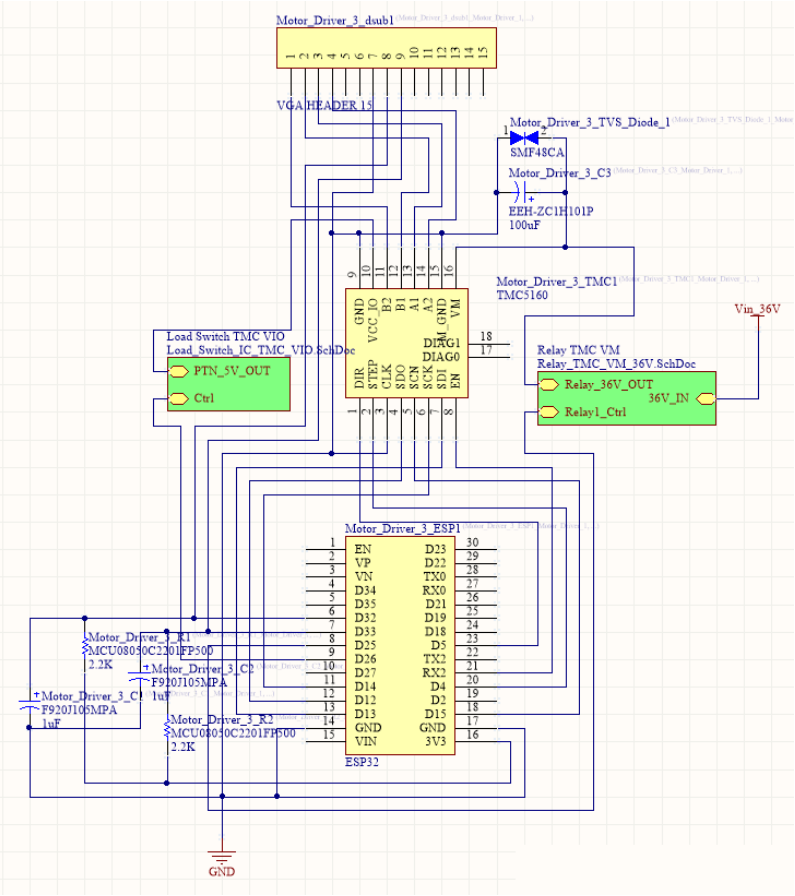

Figure 4.10: Motor Driver Schematic
Source: Altium Designer Motor Driver Project

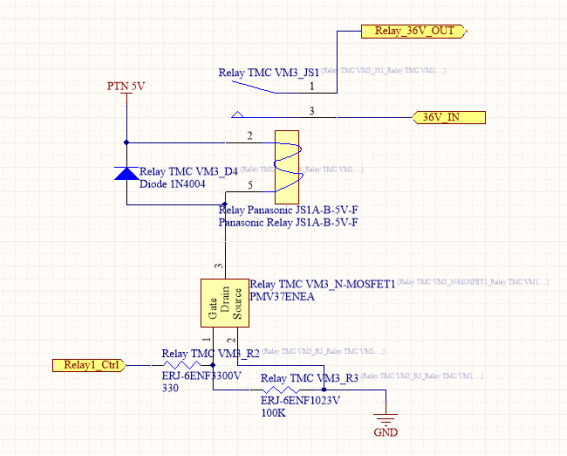

Figure 4.11: Relay Schematic
Source: Altium Designer Motor Driver Project

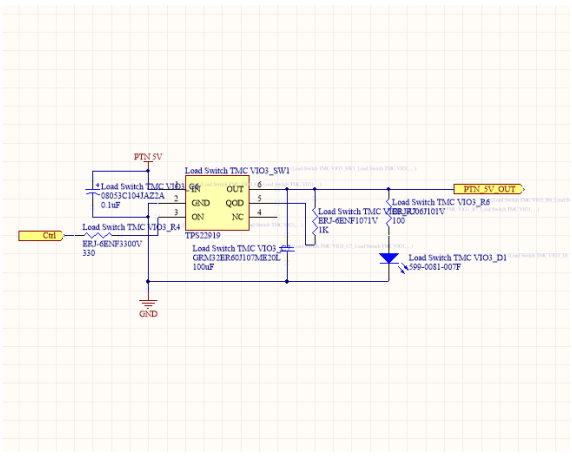

Figure 4.12: Load Switch Schematic
Source: Altium Designer Motor Driver Project

Three Axis Design Finalizing the single channel design was crucial so to proceed to the Three Axis Motor Driver Design and the PCB printing. The advantage of the **Three Axis Design** is the ability of operating three individual motors with a single PCB, including all the needed power and signal management. By utilizing three separate **ESP32 SoCs**, as a **6 Core Real Time Motion Controller** for **X Y Z** systems, and a **USB Hub** the system can be operated with one (USB) **Data Cable** and one **Power Cable**.

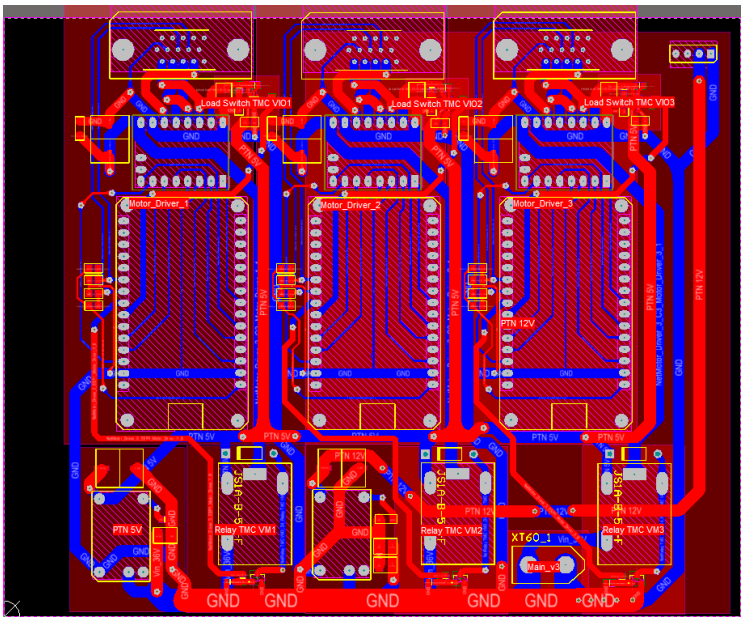

Figure 4.13: Motor Driver PCB
Source: Altium Designer Motor Driver Project

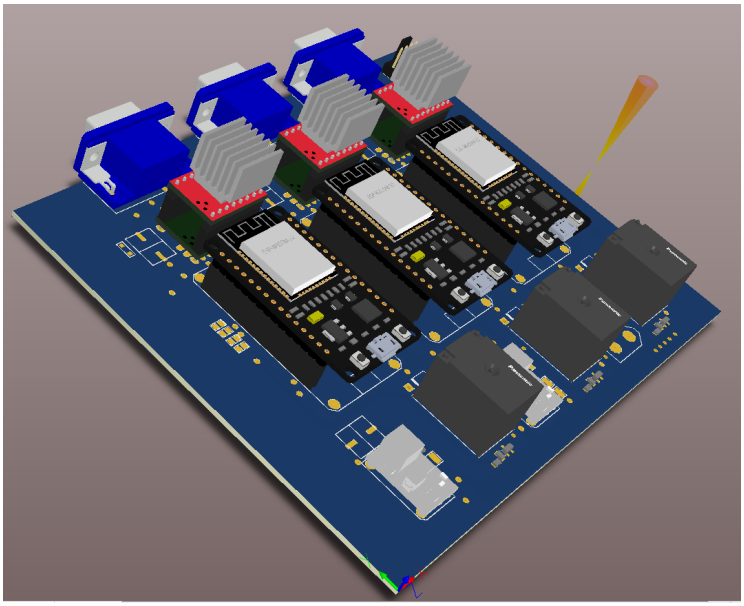

Figure 4.14: Motor Driver PCB 3D
Source: Altium Designer Motor Driver Project

Final Design The final system is enclosed with a robust aluminium case and it is installed inside the microscopes body. A silent but powerful fan is also mounted on the case, to keep the temperature of the Three Axis Motor Driver within an acceptable range. The motors connectivity to the drivers is accomplished by utilizing three VGA (DB-15) connectors. A single USB cable manages all the data transceiving from and to the drivers and the power is provided with a XT-60 connector.

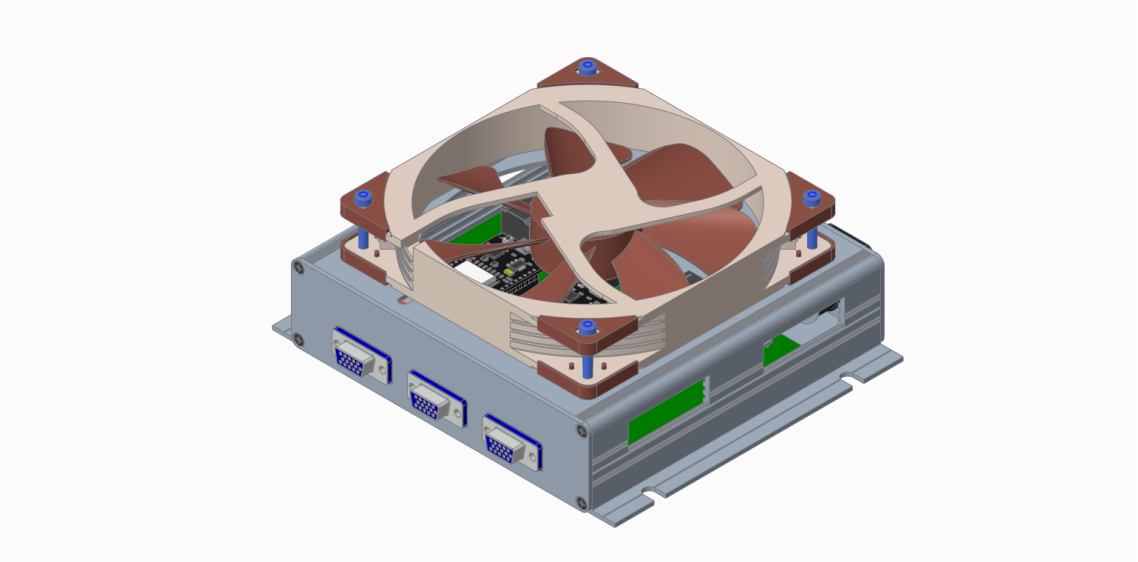

Figure 4.15: Motor Driver Final Design 3D
Source: Altium Designer Motor Driver Project

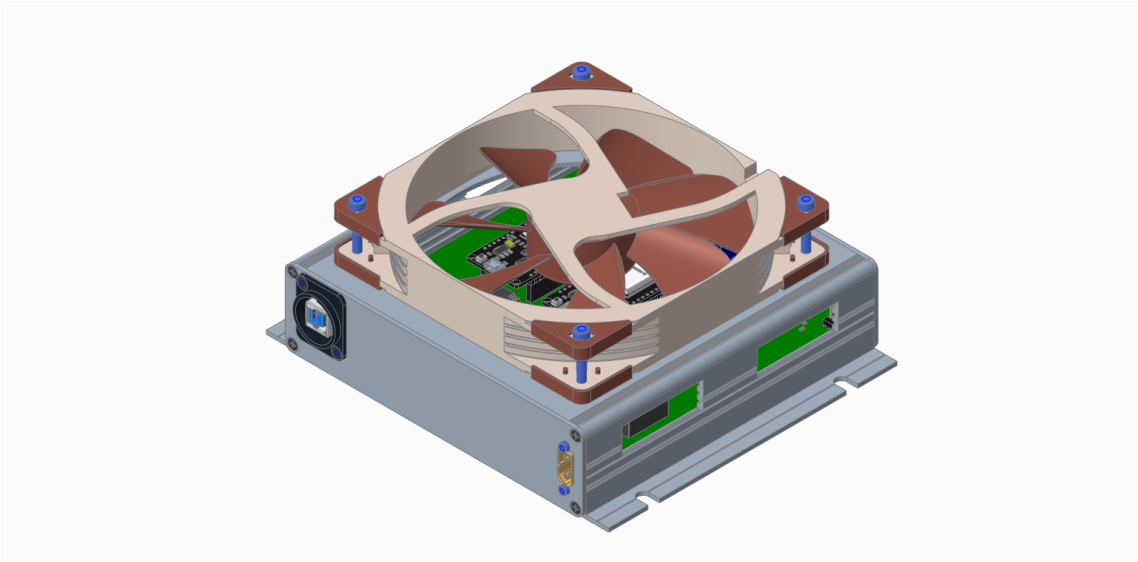

Figure 4.16: Motor Driver Final Design 3D
Source: Altium Designer Motor Driver Project

4.2.2 Functional Segmentation

Each **Motor Driver** module is dedicated on configuring its TMC5160 driver and operating the motor with respect to the input commands and the connected motor. Figure [4.17] presents the Functional Block Diagram of the Motor Driver's Design Architecture.

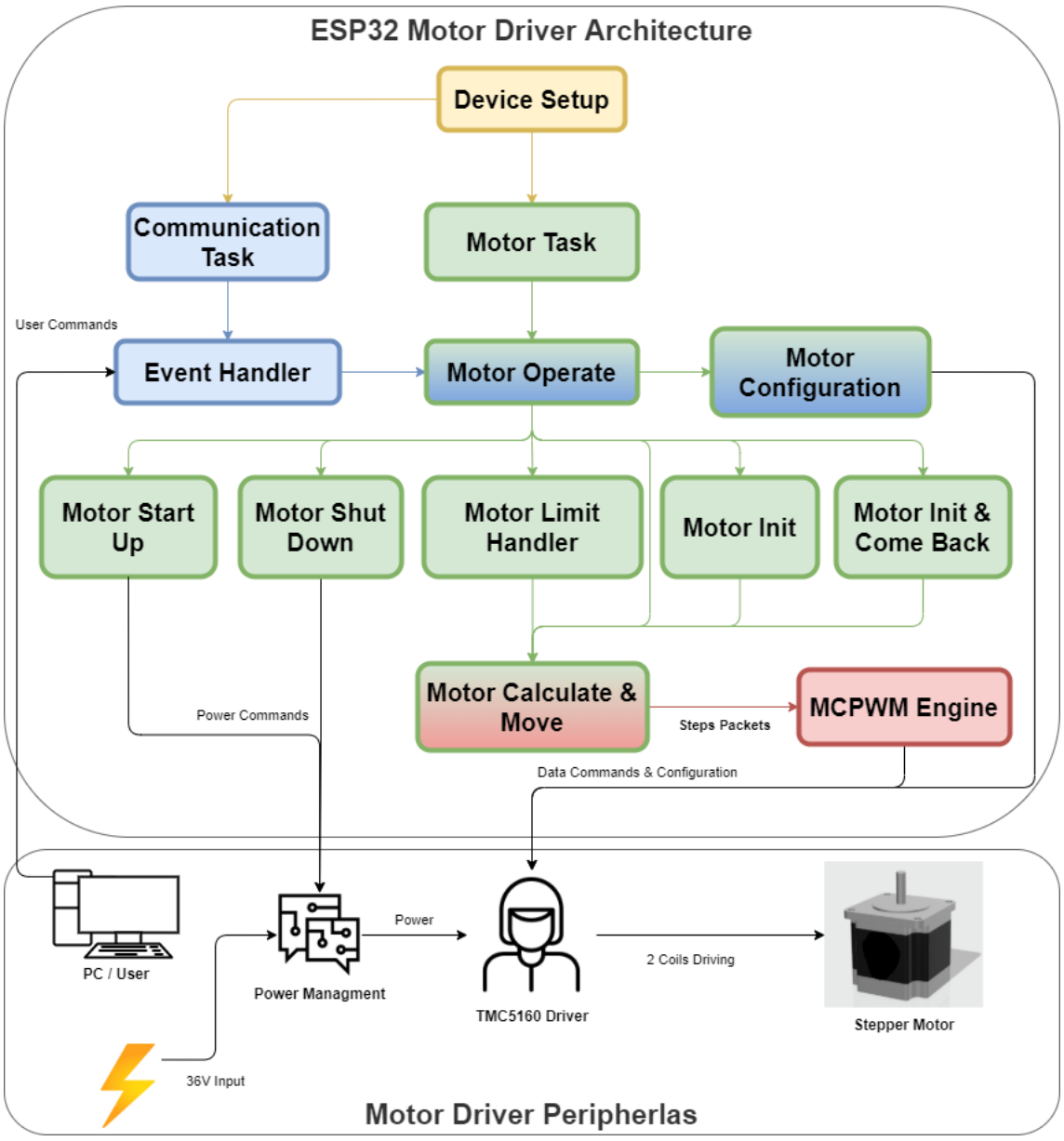

Figure 4.17: Motor Driver Architecture

The diagram of Figure [4.17] silhouette the interface the ESP32 Motor Driver with each of its peripheral components. Each of the blocks presented in the ESP32 Motor Driver Architecture section, will be described analytically in the following sections.

The fundamental functions, utilities and variables of the driver are **Utility Variables**, **Initial Calculations**, **Motor Operation** and **Motor Engine**.

- **Utility Variables**
  This set of variables is responsible for configuring and re-configuring in real time the system's behaviour. Therefore, by carefully configuring them, this driver can be used to drive a big variety of stepper motors.
  - `umPerStep`: Defines the minimum amount of distance the connected motor can move, it is measured in **um**. A typical value is **0.785 um**.
  - `MOTOR_STEPS`: Defines the steps that the connected motor will execute for a complete revolution (360°), it is measured in **steps**. A typical value is **200 steps** or **1.8° per step**.
  - `MICROSTEPPING`: Defines the microsteps in which every single step will be divided, it is measured in **microsteps** that range from **1 to 256**. A typical value is **16 microsteps** per step.
  - `DRIVER_CURRENT_mA`: Defines the maximum electrical current the driver will push to the connected motor in order to operate it. `DRIVER_CURRENT_mA` is measured in **mA** and a typical value is **670 mA**.
  - `MAX_ACCEL`: Defines the maximum acceleration constant that the driver will multiply with the corresponding value from the Acceleration Lookup Table to produce the acceleration ramp. It is measured in **RPS/step** and a typical value is **0.0008 RPS/step**.
  - `MAX_DECEL`: Defines the maximum deceleration constant that the driver will multiply with the corresponding value from the Deceleration Lookup Table to produce the deceleration ramp. It is measured in **RPS/step** and a typical value is **0.0008 RPS/step**.
  - `MAX_SPEED_RPS`: Defines the maximum speed that the driver will operate at, corresponding to the connected motor. It is measured in **RPS** and a typical value is **20 RPS**.
  - `MIN_SPEED_RPS`: Defines the minimum speed that the driver will operate at, corresponding to the connected motor. It is measured in **RPS** and a typical value is **0.1 RPS**.
  - `INIT_SPEED_RPS`: Defines the initial speed that the driver will start operating from, in order for any movement to occur as fast as possible. It is measured in **RPS** and a typical value is **2 RPS**.
  - `STOP_SPEED`: Defines the speed that the driver will stop operate at, in order for any movement to stop as fast as possible. It is measured in **RPS** and a typical value is **1 RPS**.
  - `ERR`: Defines the maximum acceptable error in speed calculations, that the driver will take into account during real time decision making. This parameter is crucial for the system, in order for any movement to occur as smoothly as possible. It is measured in **RPS** and a typical value is **1 RPS**.
  - `limitTrigger`: Defines the state, from a deterministic point of view, according to which the axis limit handling system will react to potential events. It is a **Boolean Expression** and the acceptable values are **1** for low-to-high transition triggering and **0** for high-to-low transition triggering.
  - `MIN_AXIS_LENGTH & MAX_AXIS_LENGTH`: Defines the minimum and maximum acceptable motor positions, that the driver will be virtually bound to. This parameter is crucial for the system, in order to add virtual limitations to the motor's axis length. It is measured in **um** and typical values are **100000 um** for the `MAX_AXIS_LENGTH` and **0 um** for the `MIN_AXIS_LENGTH`.
- **Lookup Tables**
  There are two types of tables used in this design, the **Speed Tables** and the **Steps Count Tables**. Every table is calculated with respect to the connected motor and parameters such as the predefined **Utility Variables**.

* **speedTable** This table stores all available speed levels at which the system can operate, considering the predefined `MIN_SPEED_RPS & MAX_SPEED_RPS`, as well as the sampling rate of the corresponding continuous time signal SamplingRate. SpeedTable's values are measured in **RPS**.

$$speedTable(i) = \left| \frac{(i+1) \cdot (maxSp - minSp)}{SamplingRate} \right| + minSp \tag{4.2.2.1}$$

Where `minSp` is `MIN_SPEED_RPS`, `maxSp` is `MAX_SPEED_RPS` and `i` ranges from 0 to SamplingRate.

* **slope** This table stores values corresponding to the acceleration factor over time. In other words this table describes the acceleration derivative by determining a relative acceleration factor in respect to the user-defined `MAX_ACCEL`.

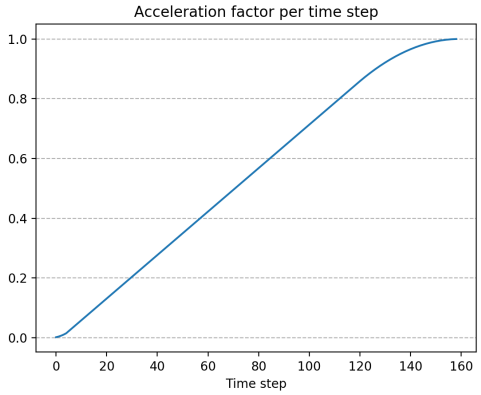

Figure 4.18: Acceleration Curve

* **accelStepsTable** This table stores values that describe the distance (in steps) from the Current Speed Index to `MAX_SPEED_RPS`. AccelStepsTable's values are measured in **steps**.

$$accelStepsTable(i) = \sum_{i=0}^{SamplingRate} \left| \frac{speedTable(i+1) - speedTable(i)}{slope(i) \cdot \texttt{MAX\_ACCEL}} \right| \tag{4.2.2.2}$$

Where i ranges from 0 to SamplingRate.

* **decelStepsTable** This table stores values that describe the distance (in steps) from the Current Speed Index to `MIN_SPEED_RPS`. DecelStepsTable's values are measured in **steps**.

$$decelStepsTable(i) = \sum_{i=0}^{SamplingRate} \left| \frac{speedTable(i+1) - speedTable(i)}{slope(i) \cdot \texttt{MAX\_DECEL}} \right| \tag{4.2.2.3}$$

Where i ranges from 0 to SamplingRate.

- **Calculations & Motor Operation**
  The Calculations section of the driver unit, is dedicated on the real time decision making. By utilizing the **Lookup Tables** and the **Utility Variables** described earlier, the **Speed Control Calculations** system is able to process any user command and translate it to precise motor motion in real time. Every decision taken by this unit gets translated in packets of steps with constant speed, which are fed to the **Speed Control Queue** to be executed from the **MCPWM engine**.

- **Motor Engine**
  The **MCPWM engine** decodes and transmits the steps packets, as **PWM** signal, from the **Speed Control Queue** to the **TMC5160 Step Input Pin**. This process is executed asynchronously by the peripheral hardware of the **ESP32 SoC**. The MCPWM has limited speed but wide pulse-width adjustment. Motors will work with somewhat fast PWM due to their inertia and high inductance, which acts as a low pass filter. Normally a motor speed control stays within the range that the motor can filter naturally, due to its inductance. Furthermore, the captured inputs from the motor, generates Interrupts (ISRs) for inspection of the motors operation (overloads, absence of load, motor current vs. expected current).

Devices Setup: Every custom device of our design, is code wise configured by attaching a Task to each Core of the ESP32. A peripheral device needs to communicate with the main system, so a **Hardware Communication** Task is attached to Core 0 of the ESP32, providing bidirectional real-time data streaming with the main system. The other Core of the ESP32 (Core 1) is used as a **Hardware Driver** that is designed to serve the fundamental purpose of each device. Each **Hardware Driver** is capable of being manipulated and setup by the **Hardware Communication** Task, not only on the initial **Device Setup**, but also on run time.

Code Segmentation: The code for the Device Setup is dedicated on configuring which Task runs on each core and setting up the global Variables used by the system and its cores.

Figure 4.19: Device Setup Block Diagram

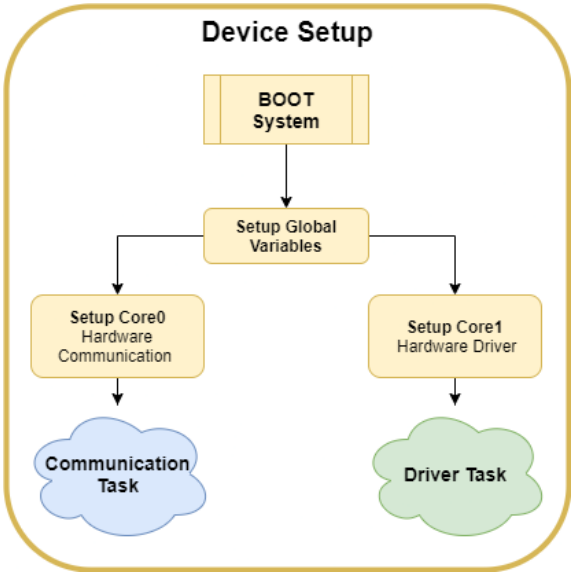

The color coding of this diagram [4.19] is designed to distinguish the parallel processing of tasks by the ESP32.

- Yellow color represents the blocks of code that are executed once by the MCU, the core they run at is not critical.
- Blue color represents the blocks of code that are executed at Core 0 of the MCU.
- Green color represents the blocks of code that are executed at Core 1 of the MCU.
-  represents the starting code block of each code section.
-  represents a link to another code section, calling its starting block.
-  represents the ending code block of each code section.

This Block Diagram representation [4.19], silhouette the initial procedure our custom devices will execute when powered up. Initially, the system will boot and setup all the global variables and structures that are going to be used for Device Identification, Version Control, Tasks Communication and Memory Management.

At this point, the non parallel procedures are finished and each individual core of the ESP32 is ready to get instructions about its functionality. For this to be accomplished, the system utilizes the FreeRTOS **xTaskCreatePinnedToCore** function and sets up the **Hardware Communication** Task to run at Core 0 and the**Driver** Task to run at Core 1, with specified Stack Memory Size, Input Parameters and Priority.

Finally, the system is ready to allocate tasks in each core depending on each device purpose. A generic setup for all of our real time decision making devices is accomplished by setting up a core to handle all the communication procedures and the other to handle the hardware driving procedures. Each task implemented for the purpose of this thesis, is autonomous and Thread Safe.

Motor Task: This block [4.20], presents the main task of the **Motor Driver** module. The color coding and the shapes used in these diagrams [4.20, 4.24, 4.25] follow the same fundamentals as [4.19] with one extra indication.

-  This is a color indication that characterises if a block of code of Core x is dependant on a block of code of Core y and vice versa. The outline and top half colorization indicates the Core in which the block is executed, and the bottom half indicates the Core with which it interacts.

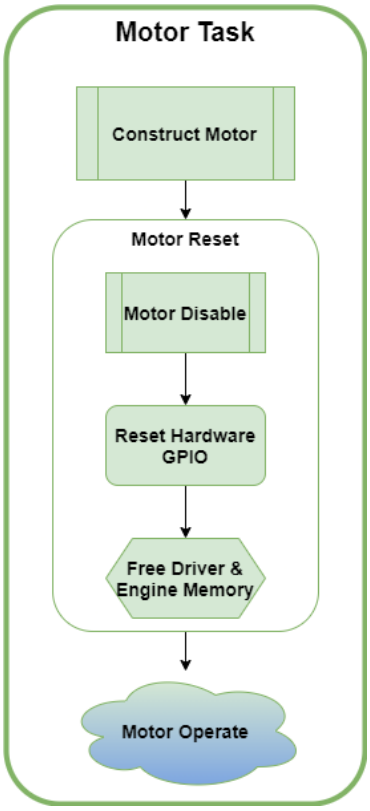

Figure 4.20: Motor Driver Task

This block executes after **Device Setup** and handles all the motor control and functionality. It is the main function running on Core 1 of the ESP32 as the **Driver Task**.

Motor Task is the main process an ESP32 needs to implement in order to gain access over the peripherals needed to drive a motor. This task initially, allocates memory for functions and variables, enabling the **Motor Driver** to be constructed from the **Motor Operate** block.

In order to normally execute the **Motor Operate** block and thus start up a new motor safely, the system needs to reset all the potentially hazardous allocated memory blocks and GPIOs. This is accomplished by firstly disabling the **Motor Driver** to ensure that the Power Stage is off and then resetting the variables, memory stacks, tasks and enabled peripherals used from the **Motor Driver**'s stepper engine.

Finally, the **Motor Operate** code section is ready to start up. This section, handles all the Location - Speed Control as well as the Packages Organisation and the data transactions with the stepper engine. For this operation to begin, it is necessary to have a connected user to the **Hardware Communication Task**, otherwise the driver will stay idle.

Motor Operate: This block [4.21], presents the main task of the **Motor Driver** module.

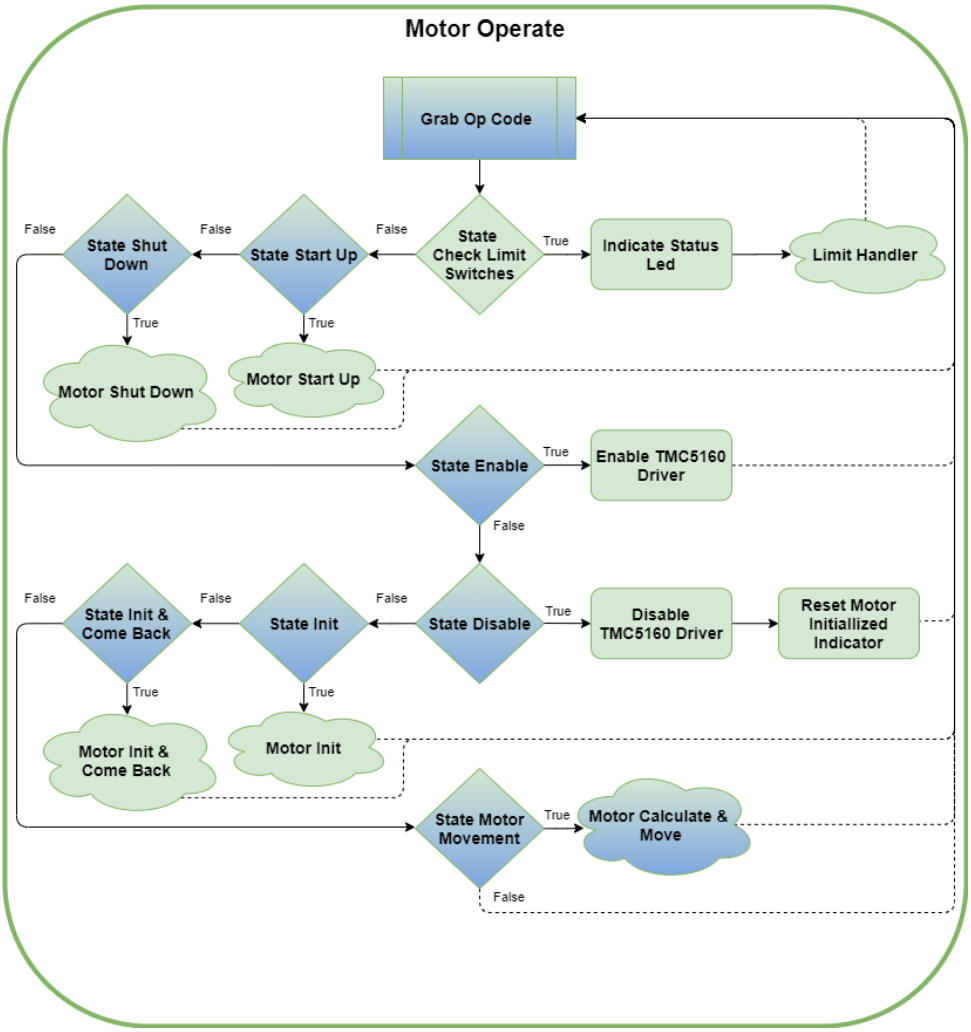

Figure 4.21: Motor Driver Operation

Motor Operate, as shown in Figure [4.21], is the core process of the **Motor Driver**, dedicated in motor management, decision making, handling interrupts and real-time speed control. This block, implements a State Machine which in every cycle receives user input and manipulates its functions. This state machine always tries to execute the **Motor Calculate & Move** block after checking all the possible hazard or incoming user command cases.

Initially, before each decision it made, the Motor Driver synchronises its user interface parameters with Hardware Communication. Then, it reads the Axis Limit Switches and if an event has occurred calls the Limit Handler function that handles the event with care. If there was not any limit switch pressed at the time, the driver checks if the user demands any special functionality to be executed, like Start Up or Shut Down, power stage enabling or disabling or axis initialization.

Finally, if all these checks passed without any interruption, the driver will go into a calculation mode in which the it will parse the target variables provided by the user through the **Hardware Communication**, and it will tune the system's peripherals to catch up with the targets.

In order for this block to be executed, the user has to send the **Start Up** command to initialize the drivers engine. This functionality is executed in an infinite loop, and the only way to stop it, is by calling the motor **Shut Down** command to disable the whole system.

Motor Calculate & Move: This block [4.22], presents the main task of the **Motor Driver** module.

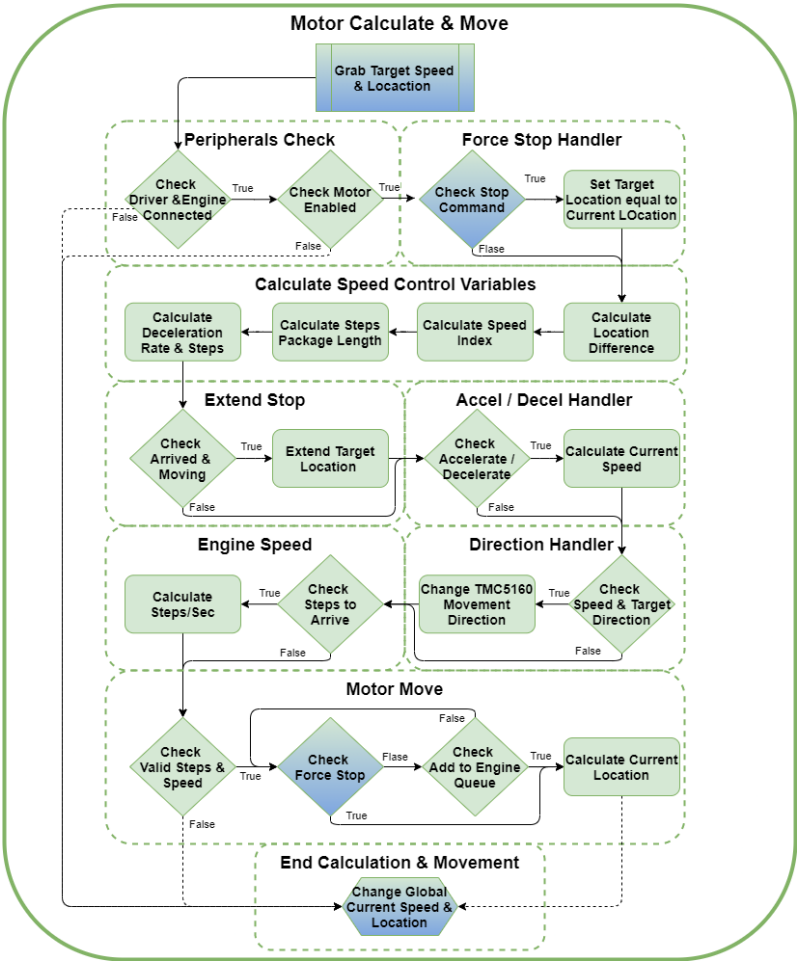

Figure 4.22: Motor Driver Real Time Calculations

As discussed previously, this section is the controller of any potential movement the motor will execute and it is called only if there was no hazard or user interrupt in the previous section. Nonetheless, this unit checks if the motor engine is connected to driver and if the motors is enabled at the time, so to execute its calculations for a reason, otherwise the block finished instantly its operation and returns to the previous loop.

Before any calculation occur, the unit also pareses the **Force Stop** data so to manipulate the calculation target parameters not for further moving but for fast deceleration thus stopping the motor. Then, regardless of whether the motor needs to stop or continue functioning, the driver begins calculations of the speed control variables based on the target variables.

Now, based on the calculated **Speed Control** variables, the driver has to decide whether or not it has to extend its target location for a smooth motor deceleration. Based on the previous calculations, the next step is to define the motors current speed and if there is a need for acceleration or deceleration at all or any direction changes. These direction changes can only occur if the motors current speed under the safe limit of `DIR_SPEED`.

Finally, the driver performs an arrival check to protect the motor from going back and forth on the target location. This means, that the calculations were precisely made to full a buffer of steps, and so, the driver can continue by converting the speed variables from Rounds per Second to Steps per Second and validating the buffer's setup variables before transferring them to the engine. In case the driver is close enough to the target speed and location, it constructs a new buffer that contains only the needed steps to move to the target with high accuracy.

This final step of validating and transferring data from the driver to the engine is not so trivial. That's because the engine is an asynchronous peripheral system, that has to be fed data with care. This is handled by our **Engine Queue**, which can compensate insertions and removals of data buffers from different threads of code. The driver remains in this section of data transferring to the Engine Queue until there is enough space in the queue for the new buffer, while always checking for any hazardous interrupts. Finally, when the system has arrived to the target Location and has achieved zero speed, it sets up an indication for the all the other Tasks running on different Cores to know that motor is done and in idle.

Motor Limit Handler: This block [4.23], presents the limit handling system of our Driver.

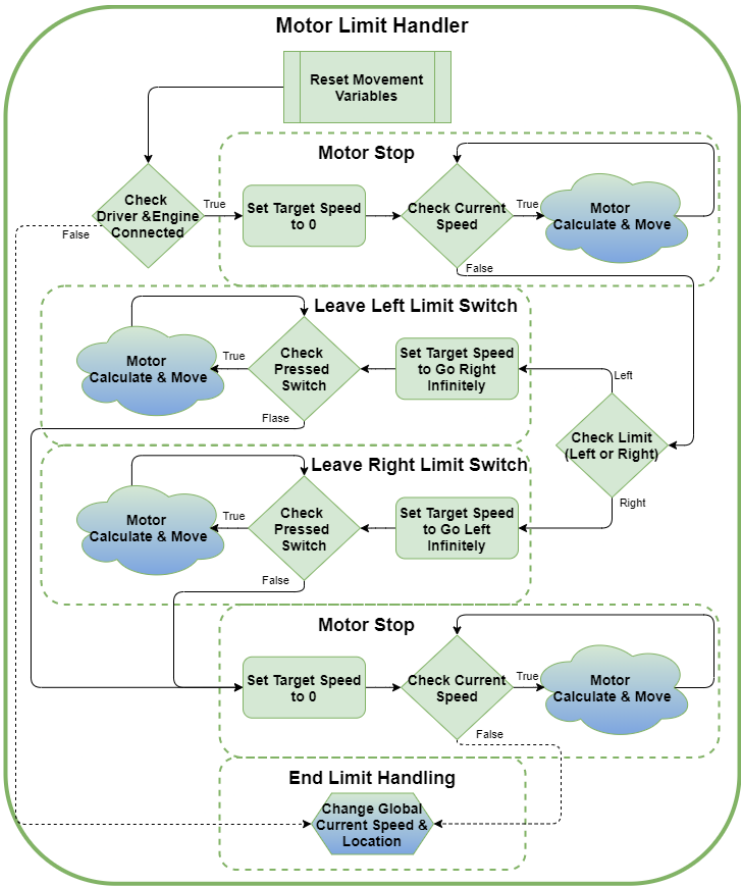

Figure 4.23: Motor Driver Limit Handler

This **Limit Handler**, shown in Figure [4.23], is a code section called from the **Motor Operate** block (Figure [4.21]) in case any hazard is detected. This code section, will block all the other sections of code running on the driver core to ensure that they will execute only if the motor is not in a hazardous state and that the hazard will be eliminated in time.

To achieve this, the limit handler, initially performs the driver to engine connection check. If it passes the check, it manipulates a set of temporary target variables and it executes its own movement loop by calling a temporary version of the same **Motor Calculate & Move** section of code with the temporary target variables, to force the motor to stop (**Motor Stop**).

When the motor has been carefully stopped, the limit handler checks which limit switch was pressed and moves the axis in the opposite direction until the limit switch gets unpressed. This is possible by performing again new calculations for the appropriate target variables and a fresh execution of the temporary movement loop. Finally, the limit switch is unpressed and the limit handler perform the same **Motor Stop** functionality to stop the motor smoothly. The motor is now safe from any collision with the axis limits and it is again available for the user.

Motor Start Up: This block [4.24], represents the "starter" of the **Motor Driver** module.

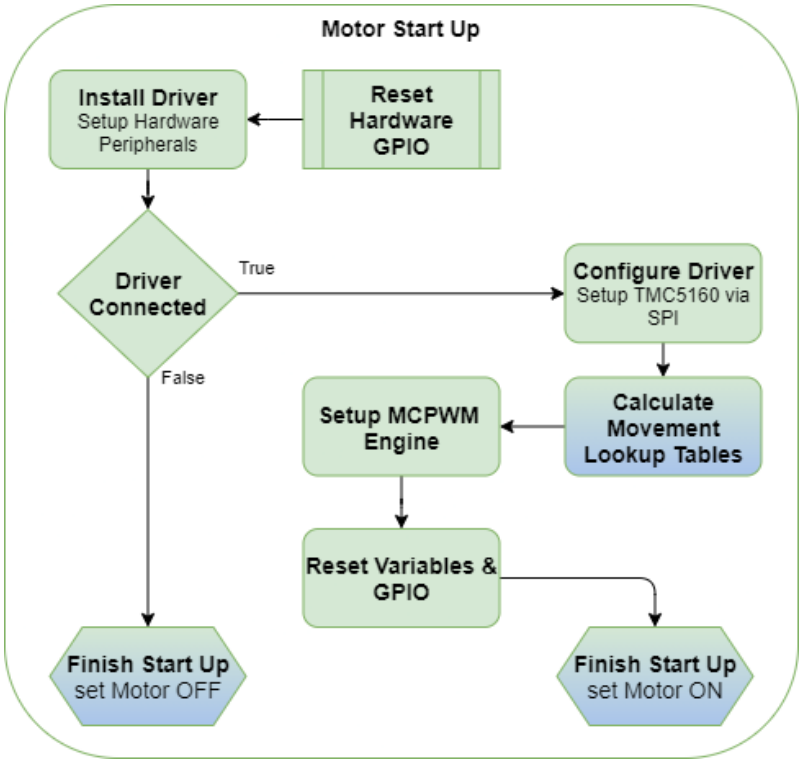

Figure 4.24: Motor Driver Start Up

This block, shown in Figure [4.24], handles the initialization of the driver's parameters and its configuration, as well as the start up of the **TMC5160 Driver** and the **MCPWM engine**. This code section is called from the **Motor Operate** block, as shown in Figure [4.21].

For a smooth start up the driver initially resets all the enabled peripherals of the ESP32 and the TMC5160. A crucial procedure before turning ON the **Motor Driver** because it handles the **Power On Sequence** with care. In order to create a new driver set of peripherals the system resets the TMC5160 driver's allocated memory and creates a new instance, with the default variables, gaining accessing its functionality.

The next step is to check whether the TMC5160 driver is properly connected with the ESP32 and if it is not connected the **Start Up** process finishes immediately to avoid powering up the power stage. On the other hand if there is a TMC5160 driver properly connected to the ESP32, the system configures the TMC5160 timing parameters, RMS current limiter, micro-stepping factor and enables the **SpreadCycle** and **StealthChop** choppers of the driver. All the communication with the TMC5160 is accomplished using the SPI synchronous serial communication interface of the ESP32.

An essential step that needs to be done before setting up the rest of the ESP32 peripheral drivers is to **Calculate Movement Lockup Tables**. This is accomplished by using the variables that the user provided through **Hardware Communication** (minSpeed, maxSpeed, initSpeed, stopSpeed, errorSpeed, acceleration and deceleration), and then by calculating the lookup tables (SpeedTable, AccelStepsTable and DecelStepsTable) that the program will use for speed control. While executing this code block, the variables it uses cannot be overwritten.

After all the necessary calculations are done, the system is ready to **Setup the MCPWM Engine**. It initializes the **Buffer Queue**, the **PCNT** (Pulse Counter) module, the **MCPWM** (Motor Control PWM) module and starts them up with the preset GPIO configuration. Finally, the driver, resets the basic Location and Speed variables and sets up an indication for the all the other Tasks running on different Cores that the **Motor Driver** is ready for use (Motor ON) or not (Motor OFF).

Motor Shut Down: This block [4.25], presents the Shut Down of the **Motor Driver** module.

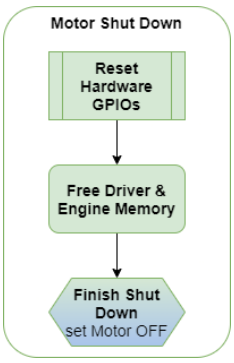

Figure 4.25: Motor Driver Shut Down

This block, shown in Figure [4.25], handles the shut down procedure of the driver's allocated peripherals. This code section is called from the **Motor Operate** block, as shown in Figure [4.21] and it is executed, by sending the **Shut Down** command through the **Hardware Communication** module of the device or by pressing the **Emergency Switch**.

For this Shut Down procedure to be done correctly, the driver firstly resets all the enabled peripherals of the ESP32 and the TMC5160 which is a crucial procedure before turning OFF the driver because it handles the **Power Off Sequence**. The next step is to delete all the allocated memory stacks and tasks used from the Motor Driver & Motor Engine, so that the Motor Operation is terminated.

Finally, the drivers sets up an indication for the all the other Tasks running on different Cores that the **Motor Driver** is disabled (Motor OFF).

Motor Initialize: These blocks [4.26, 4.27], presents the initialization or homing of the motors axis.

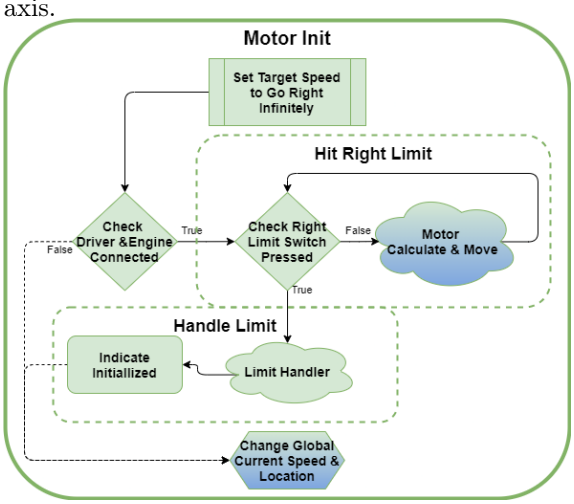

Figure 4.26: Motor Driver Initialize

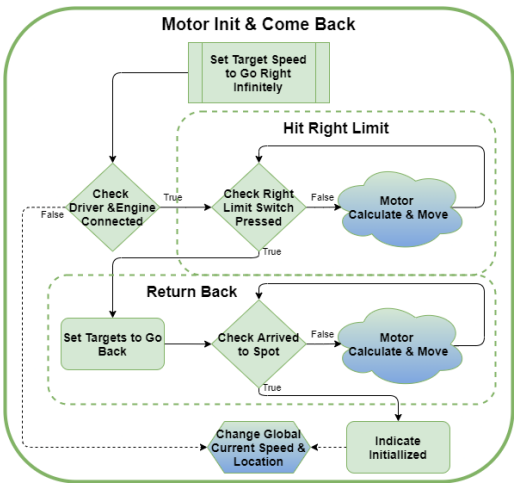

Figure 4.27: Motor Driver Initialize and Return

The blocks, shown in Figures [4.26, 4.27], are also self operating sections that when executed they will disable usage of the motor from other blocks, until they finish operation. These code sections are called from the **Motor Operate** block, as shown in Figure [4.21] by sending the **Init** or **InitAndComeBack** commands through the **Hardware Communication** module of the device. For the initialization or homing functionality to be executed as a self operating section, the driver checks again for connectivity between itself and the **Motor Engine**. Then it performs a loop of movements with temporary target variables in order to travel to the right limit switch of the axis.

When the limit switch triggers, **Motor Init** section, executes the **Limit Handler**, shown in Figure [4.23], section of code to properly handle this limit switch triggering event and it sets up an indication for the all the other Tasks running on different Cores that the **Motor Driver** is initialized. On the other hand, the **Motor Init & Come Back** section handles the limit switch triggering by its own. To properly handle this limit switch triggering event, this block has measured the steps occurred until hitting the axis limit and it performs a loop of movements with temporary target variables in order to travel back to the spot where it initially was.

Finally each block, sets up an indication for the all the other Tasks running on different Cores that the **Motor Driver** is initialized and done operating.

Hardware Communication A robust and high speed communication interface between our custom devices and the main system is critical for executing complex procedures and achieving an overall Real-Time experience. Moreover, the structure of the data packets need to be altered for the system to communicate, using the same interface, with all of our custom devices. For the reasons specified above, and for the transaction of instructions in closed loop systems, where having feedback with perfect timing is mandatory, we designed a generic hardware communication system, based on the Universal Asynchronous Receiver/Transmitter(UART) Serial communication functionality of the MCU.

Universal Asynchronous Receiver/Transmitter (UART) is a hardware feature that handles communication (i.e., timing requirements and data framing) using widely-adapted asynchronous serial communication interfaces, such as RS232, RS422, RS485. It is not a communication protocol like SPI and I2C, but a physical circuit. A UART provides a widely adopted and cheap method to realize full-duplex or half-duplex data exchange among different devices.

In UART communication, two UARTs communicate directly with each other. The transmitting UART converts parallel data from a controlling device like a CPU into serial form, transmits it in serial to the receiving UART, which then converts the serial data back into parallel data for the receiving device. Data flows from the Tx pin of the transmitting UART to the Rx pin of the receiving UART [4.28].

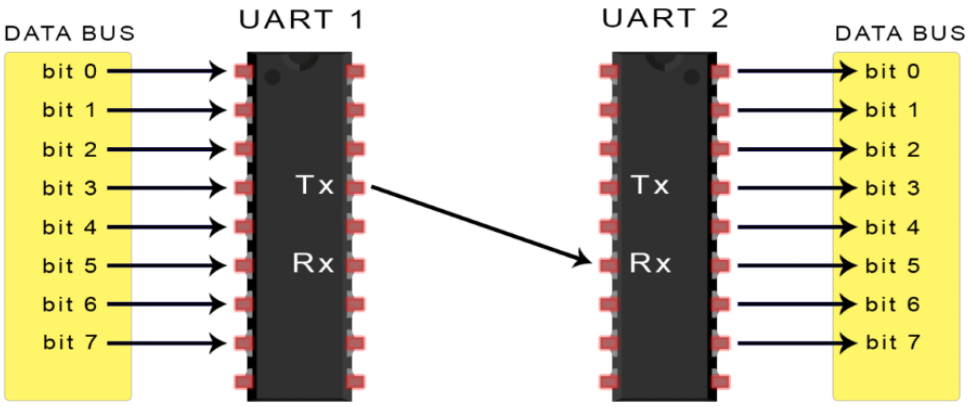

Figure 4.28: UART Communication
Source: circuitbasics.com

UARTs transmit data asynchronously, which means there is no clock signal to synchronize the output of bits from the transmitting UART to the sampling of bits by the receiving UART. Instead of a clock signal, the transmitting UART adds start and stop bits to the data packet being transferred. These bits define the beginning and end of the data packet so the receiving UART knows when to start reading the bits.

When the receiving UART detects a start bit, it starts to read the incoming data at a specific frequency known as the baud rate. Baud rate is a measure of the speed of data transfer, expressed in bits per second (bps). Both UARTs must operate at about the same baud rate and must also be configured to transmit and receive the same data packet structure.

The described interface for communication is a well documented and widely used method allowing us steady use and implementation. Also, another benefit of using the UART is the fact that no clock signal is necessary for the data transaction. Additionally, UART uses a parity bit to allow for error checking, witch is crucial for robustness in data transaction. Finally, one of the significant advantages of UART is that it only uses two wires to transmit data between devices and in our case, we used the preexisting USB interface of the ESP32 Development board so no additional hardware configuration was needed.

Code Segmentation: The code for the **Hardware Communication** section is dedicated on UART hardware peripheral utilization of the ESP32 and handling the bidirectional data transceiving events. The color coding and the shapes used in this diagram [4.29] follow the same fundamentals as [4.19].

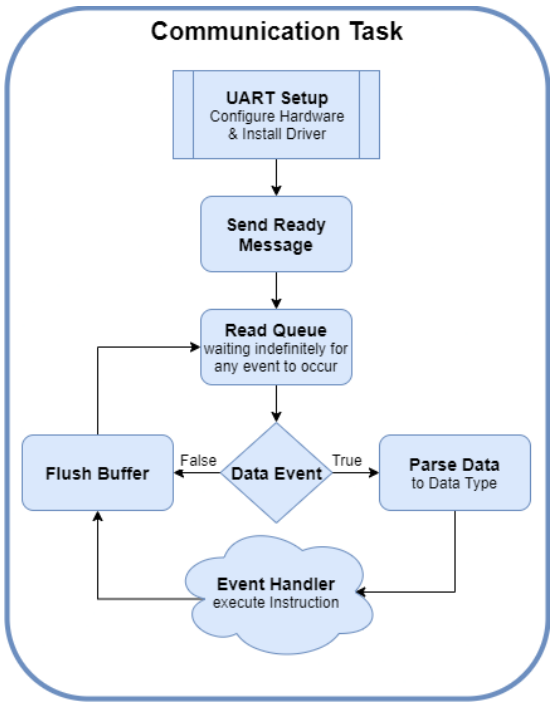

Figure 4.29: Hardware Communication Block Diagram

This Block Diagram representation [4.29], silhouette the structure of the **Hardware Communication** module. This code sets up the hardware and handles all the incoming, from the main system, events in an infinite loop. This task is terminated either by a user command or by an emergency switch also pressed by the user.

To begin with, this module utilizes the **FreeRTOS UART Library** to configure its parameters and attache specific GPIOs of the ESP32 to the UART hardware peripheral. After the hardware setup of the driver is completed, the driver installation begins. Firstly, it sets up the Buffer Queue and its useful length and attaches them to the driver and then enables the UART pattern detect function, so that the hardware can detect incoming events and trigger an interrupt. Finally, the module sends an handshaking message to the main program so that it knows when the communication setup is done. To handle the message sending procedures, the module uses the FreeRTOS `uart_write_bytes` command, which utilizes the UART channel, a string buffer containing the text and the text's length to operate.

After this operation is completed, the module is waiting indefinitely for an event to occur. When that happens, it utilizes the FreeRTOS `xQueueReceive` command for Receiving messages and copies the event's data to the Buffer Queue. For this `xQueueReceive` command to operate, there are some crucial parameters needed to be set up, a pointer to the queue from which the item is going to be received, also a pointer to the buffer into which the received item will be copied and the maximum amount of time the task should wait for an event to occur. After any event is occurred, the module checks if it is a data event or not, and executes the analogous procedure.

If there was data in the occurring event, it parses the data of the occurred event in a predefined structure that can differ from device to device and its is being related to the **Hardware Driver** it utilizes.Finally, send the data structure to the **Event Handler** corresponding to the **Hardware Driver** the device utilizes. On the other hand, if there was no data in the occurring event, the system cleans up the Buffer Queue Memory and returns to the indefinitely waiting state for new events to occur.

Motor Message Event Handler: This block [4.30], presents an application specific **Event Handler** running on the **Hardware Communication** module, designed to handle the **Motor Driver**'s Events.

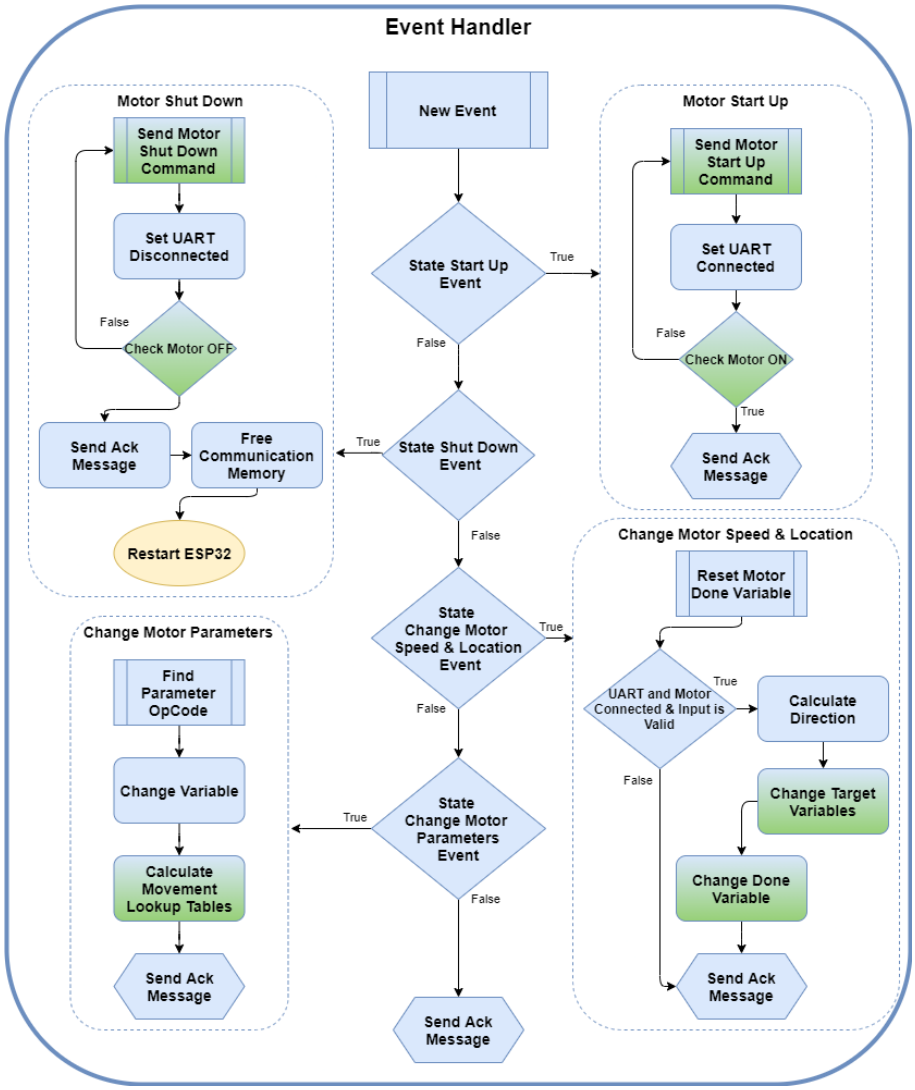

Figure 4.30: [Motor Communication Event Handler

This diagram, describes four different types of events the Motor Driver needs to handle. The State Machine picks a state by parsing the Operation Code provided by the Hardware Communication module.

- **Motor Start Up Event**
  Sends the **Start Up** command to the **Motor Driver** module, with the use of its **Operation Code** variable. To indicate that serial connection has been established with the user, it sets the **UART Connected** variable true. Every 12 ms, it checks if the **Start Up** sequence has finished, by looking at the **Motor ON** indication variable of the **Motor Driver**. Whenever the **Motor ON** indication variable becomes true, this Task knows that the user's command is satisfied and it sends an Acknowledgment message back to the user.

- **Motor Shut Down Event**
  Sends the **Shut Down** command to the **Motor Driver** module, with the use of its **Operation Code** variable. To indicate that serial connection with the user is going to end, it sets the **UART Connected** variable false. Every 12 ms, it checks if the **Shut Down** sequence has finished, by looking at the **Motor OFF** indication variable of the **Motor Driver**. Whenever the **Motor OFF** indication variable becomes true, this Task knows that

the user's command is satisfied and it sends an Acknowledgment message back to the user. Finally, it frees the allocated memory of the **Hardware Communication** module and forces the device to **Restart** itself.

- **Motor Change Speed & Location Event**
  Sets the **Done** variable of the **Motor Driver** to false, so that the driver won't stop operating while new data are getting parsed. Checks if the system is normally operating or if the input data are invalid and if something is not correct, breaks the sequence and sends the Acknowledgement error message. If everything is operating correctly, it calculates the desired movement **Direction** and changes the **Target Speed** and **Target Location** variables of the **Motor Driver**. Calculates the **Motor Driver**'s **Done** variable that indicates if the user's target Location is equal to the motors Current Location. Finally, sends the Acknowledgement message to the user.

- **Motor Change Movement Parameters Event**
  Matches the **Operation Code** with one of the **Motor Driver**'s variables. If the input data are valid it changes the analogous **Motor Driver**'s variable. Executes the Lookup Tables recalculation function of the **Motor Driver** so that the input data starts to affect the drivers calculations. Finally, sends the Acknowledgement message to the user.

This block is called whenever a new event is occupied by the **Hardware Communication** module.

In conclusion, we created a system that can easily setup and drive a huge variety of stepper motors due to its generic design and its dynamic usability.

Using this generic Motor Driver provides us the ability to control and overextend the capabilities of a stepper motor, in terms of speed and movement stability. With the help of the Acceleration and Deceleration Slope tuning mechanism, this driver can be tuned to overdrive stepper motors to accelerate rapidly from zero speed without any loss of steps, to maximum speeds exceeding the motors specified capabilities. This process is achieved by correlating the acceleration/deceleration curves (torque) with the load's inertia.

Moreover, this driver can control and manipulate linear Motorized Translation Stages with the help of its position decision making system. This can be extremely useful in applications where high level control of a motor demands the use of absolute positioning with great accuracy in real time.

4.3 Focusing

An essential and indispensable component of automated microscopes is the automatic focusing procedure. Auto Focus (AF) in digital microscopy determines the in-focus position of a given field of view by searching for the maximal focus index over a range of z-axis positions. Although focusing can be a trivial task for a trained observer, automatic systems often fail to focus images under different modalities.

Many auto focus algorithms have been proposed in the literature, but their accuracy can deviate depending on the content of the processed images. So, different focus criterion functions perform quite differently even for the same specimen. This occurs because these procedures are highly dependent on the sample topography variability and also its color distribution. Thus, among the publications that have analyzed a wide variety of auto focus methods, a different technique is proposed each time because it offers better results in each specific application.

Auto focus accuracy and its computation time are crucial to the robustness and efficiency of the system. So, the selection of a particular auto focus method depends on both criteria. [8]

4.3.1 Auto Focus Algorithms

In wide-field microscopy, the focusing procedure is done mechanically and is obtained by varying the distance between the objective lens and the subject. There are two types of auto focus systems – active and passive.

Active auto focus systems have a mechanism, that measures the distance between the camera and the subject, which does not depend on optical system and accordingly corrects the focus. The distance is measured mainly with the use of infrared light and ultrasonic sound waves. The advantage of an active auto focus system is that it has no limitation of low luminosity and it is easy to calculate the best focus position.

Passive auto focus systems are based on analyzing the sharpness of the imaging region, which is usually associated to a higher frequency content. Lots of different image processing techniques have been proposed in the literature about passive auto focusing. The advantages of these methods are that they can find differences in focus levels as long as the optic system and the camera can capture the variation. [8]

Usually, the accuracy of active systems is less than the passive systems. Active systems are unable to focus a subject very close to the camera, while passive systems find it hard to focus in situations where contrast or light condition is low. Therefore, a desirable focus measure should be evaluated in terms of reliability, accuracy and speed.

Having the solid understanding of the AF systems we began by implementing some of the proposed passive auto focus algorithms in C++. Based on our application, we later evaluated the results. In the following pages we present the implemented algorithms as well with their results.

1. **Derivative-Based Algorithms**

   These algorithms assume that well-focused images have more high-frequency content than blurred images. Neighbouring pixels in images with high-frequency content have large differences in intensity. The larger these intensity changes, the sharper the edges. In order to apply high pass filtering, these algorithms apply convolution masks to an image to obtain derivatives. [7]

   - **Brenner gradient:** This algorithm computes the first difference between a pixel and its neighbour with a horizontal/vertical distance of 2. [7] This is a fast method and we wait to see results that are relevant to the threshold value.

$$F_{Brenner} = \sum_{j}^{Height} \sum_{i}^{Width-2} (img(i+2,j) - img(i,j))^2 \qquad (4.3.1.1)$$

```
double MicroImageAnalysis::Brenner(QImage im){
    double Bren = 0,val =0;
    for(int i=1; i<im.width()-2; i++)
    {
        for(int j=1; j<im.height(); j++)
        {
            val += (qGray(im.pixel(i, j))-qGray(im.pixel(i+2, j)))*(qGray(im.pixel(i, j))-qGray(im.pixel(i+2, j)));
            if(val >= thresh){//threshold
                Bren+=val/100;
            }
        }
    }
   return Bren;
}
```

Figure 4.31: BrennerGradient C++ Implementation

where $[img(i+2,j) - img(i,j)]^2 >= threshold$

- **Vollath–5:** This algorithm presented a systematic study of the properties of auto focus criteria and proposed an equation that suppresses high frequencies. This metric is completely independent of noise.

$$F_{VOL5} = \sum_{j}^{Height} \sum_{i}^{Width-1} (img(i,j) \cdot img(i+1,j)) - (Width \cdot Height \cdot mean^2) \quad (4.3.1.2)$$

```
double MicroImageAnalysis::VollathF5(QImage im , int n){
    double f5 = 0;
    for(int i=1; i<im.width()-1; i++)
    {
        for(int j=1; j<im.height(); j++)
        {
            f5 += (qGray(im.pixel(i, j)) * qGray(im.pixel(i+1, j)))-(n*meanQimage(im)*meanQimage(im));
        }
    }
    return abs(f5)/100000;
    return 0;
}
```

Figure 4.32: Vollath-5 C++ Implementation

These methods are fast and will result to noise independent focus levels.

2. **Statistics-Based Algorithms**

These statistics-based algorithms, generally less sensitive to noise than derivative-based algorithms, distinguish focused images from defocused images using variance and correlation. [7]

- **Variance:** This algorithm computes variations in grey level among image pixels. It uses the power function to amplify larger differences from the mean intensity <mean> instead of simply amplifying high intensity values. [7]

$$F_{Var} = \frac{1}{Height \cdot Width} \sum_{j}^{Height} \sum_{i}^{Width} (img(i,j) - mean)^2 \quad (4.3.1.3)$$

```
// Function to find Variance.
double MicroImageAnalysis::Variance(uchar *arr, int n)
{
    double re = standardDeviation(arr, n)/(n);
    return re;
}
```

Figure 4.33: Variance C++ Implementation

- **Normalized variance:** Normalizing the final output with the mean intensity <mean>, this algorithm compensates for the differences in average image intensity among different images. [7]

$$F_{NormVar} = \frac{1}{Height \cdot Width \cdot mean} \sum_{j}^{Height} \sum_{i}^{Width} (img(i,j) - mean)^2 \quad (4.3.1.4)$$

These methods will result in a fast and accurate outcome in the focused images.

```
// Function to find NormalizedVariance.
double MicroImageAnalysis::NormalizedVariance(uchar *arr, int n)
{

    double re = standardDeviation(arr, n)/(n*mean(arr, n));


   return re;

}
```

Figure 4.34: Normalized Variance C++ Implementation

```
// Function to find mean of given array.
double MicroImageAnalysis::mean(QImage im)
{
    double sum = 0;
    for (int i = 0; i < im.width(); i++){
        for (int j = 0; j < im.height(); j++){
            sum = sum + qGray(im.pixel(i,j));
        }
    }
    return double(sum / (im.width()*im.height()));
}

// Function to find standard deviation of given array.
double MicroImageAnalysis::standardDeviation(QImage im)
{


    double sum = 0;
    double mea = mean(im);

    for (int i = 0; i < im.width(); i++){
        for (int j = 0; j < im.height(); j++){
        sum = sum + (qGray(im.pixel(i,j)) - mea) *
                    (qGray(im.pixel(i,j)) - mea);
        }
    }
    return double(sqrt(sum / (im.width()*im.height())));

}
```

Figure 4.35: mean and standardDeviation methods

3. **Intuitive Algorithms**

- **Thresholded pixel count:** This algorithm counts the number of pixels having intensity below a given threshold. [7]

$$F_{Var} = \frac{1}{Height \cdot Width} \sum_{j}^{Height} \sum_{i}^{Width} s(img(i,j), thres) \tag{4.3.1.5}$$

where $s(img(i,j), thres) = \left\{ \begin{array}{ll} 1, & img(i,j) <= thresh \\ 0, & \text{else} \end{array} \right\}$

```
double MicroImageAnalysis::ThresholdPixelCount(QImage im,int thres){

    double sum = 0;

    for(int i=1; i<im.width()-1; i++)
    {
        for(int j=1; j<im.height(); j++)
        {
            if(abs(qGray(im.pixel(i+1, j))-qGray(im.pixel(i, j)))>thres) sum
            += abs(qGray(im.pixel(i+1, j))-qGray(im.pixel(i, j))) ;
        }
    }
    return sum;
}
```

Figure 4.36: Threshold pixel count C++ Implementation

This is a very fast method and we wait to see results that again are relevant to the threshold value.

4. **Image Transformations based Algorithm**

- **Midfrequency–DCT (MDCT):** The influence of the band–pass DCT coefficients on the focus measure can be calculated as: [8]

$$F_{Var} = \frac{1}{Height \cdot Width} \sum_{j}^{Height} \sum_{i}^{Width} (img(i,j) * O_{MDCT})^2 \tag{4.3.1.6}$$

where $O_{MDCT} = \begin{bmatrix} 1 & 1 & -1 & -1 \\ 1 & 1 & -1 & -1 \\ -1 & -1 & 1 & 1 \\ -1 & -1 & 1 & 1 \end{bmatrix}$.

```
double MicroImageAnalysis::MDCT(QImage image)//Midfrequency Discrete Cosine Transform
{
        QMatrix4x4 om;
        om(0, 0) = 1; om(0, 1) = 1;     om(0, 2) = -1; om(0, 3) = -1;
        om(1, 0) = 1; om(1, 1) = 1;     om(1, 2) = -1; om(1, 3) = -1;

        om(2, 0) = -1; om(2, 1) = -1;   om(2, 2) = 1; om(2, 3) = 1;
        om(3, 0) = -1; om(3, 1) = -1;   om(3, 2) = 1; om(3, 3) = 1;

        double outs = 0;
        if(image.isNull())
            return 0;
//grayscale
        for(int i=1; i<image.width()-3; i++)
        {
            for(int j=1 ; j<image.height()-3; j++)
            {
                image.setPixel(i, j, uint(qGray(image.pixel(i, j))));
            }
        }
//convolution with mask
        for(int i=1; i<image.width()-3; i++)
        {
            for(int j=1; j<image.height()-3; j++)
            {
                double v =0;

                // ***************************************************
                v =
                        om(0, 0) * qGray(image.pixel(i, j)) +
                        om(0, 1) * qGray(image.pixel(i+1, j)) +
                        om(0, 2) * qGray(image.pixel(i+2, j)) +
                        om(0, 3) * qGray(image.pixel(i+3, j)) +

                        om(1, 0) * qGray(image.pixel(i, j+1)) +
                        om(1, 1) * qGray(image.pixel(i+1, j+1)) +
                        om(1, 2) * qGray(image.pixel(i+2, j+1)) +
                        om(1, 3) * qGray(image.pixel(i+3, j+1)) +

                        om(2, 0) * qGray(image.pixel(i, j+2)) +
                        om(2, 1) * qGray(image.pixel(i+1, j+2)) +
                        om(2, 2) * qGray(image.pixel(i+2, j+2)) +
                        om(2, 3) * qGray(image.pixel(i+3, j+2)) +

                        om(3, 0) * qGray(image.pixel(i, j+3)) +
                        om(3, 1) * qGray(image.pixel(i+1, j+3)) +
                        om(3, 2) * qGray(image.pixel(i+2, j+3)) +
                        om(3, 3) * qGray(image.pixel(i+3, j+3));

                outs += v*v;
            }
        }
    return outs/10000;
}
```

Figure 4.37: Midfrequency_DCT C++ Implementation

This is a time-consuming method but we will probably achieve high accuracy due to the noise reduction caused by the filter.

Results To evaluate the results of the focus research we will use the Focus Scan method of our microscope in the same sample, utilizing all the algorithms discussed previously. Here is a graphical representation of our Focus Scan method executed on a DAB - Haematoxylin sample, as shown in Figure [4.38]. The motion control system uses:

- Z Resolution 78.125 nm.
- Images Distance 10 steps x Z Resolution or 781,25 nm.
- Full Scan Focal Depth is 31.25 um.

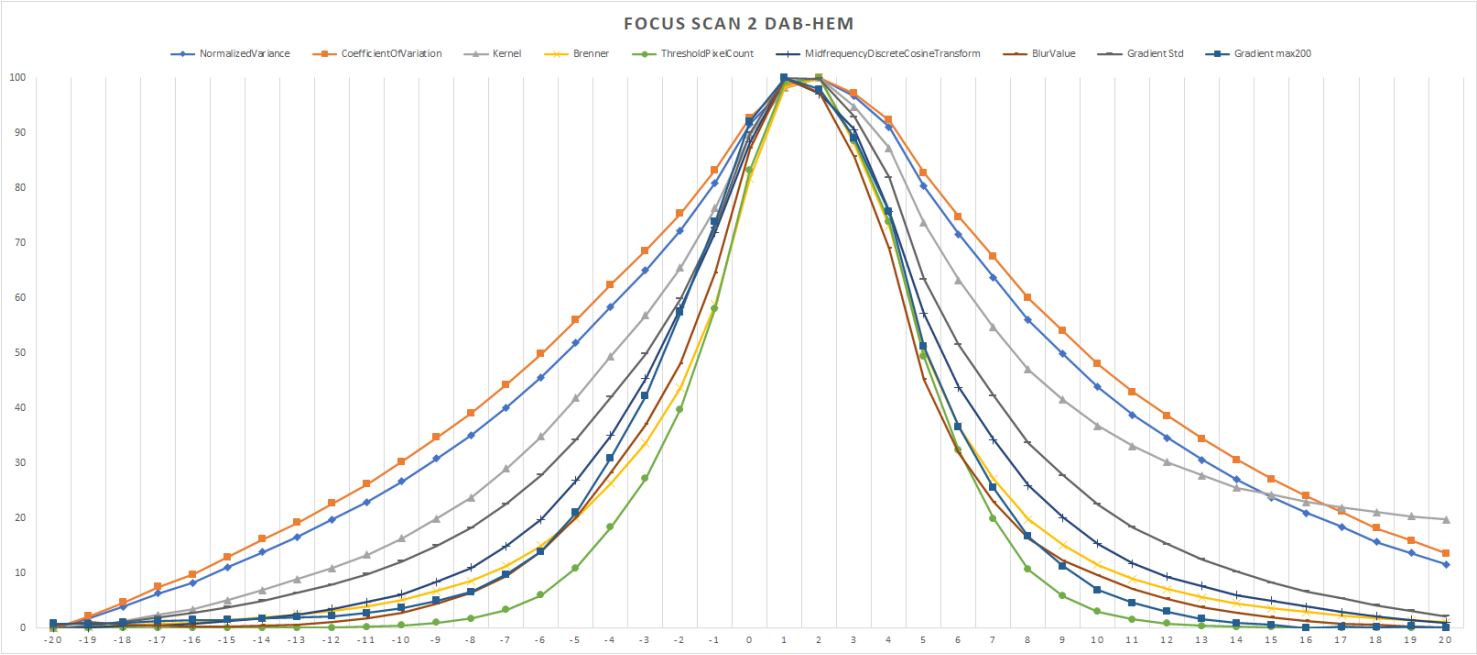

Figure 4.38: Focus Scan of DAB Hematoxylin Specimen

In conclusion, there are many algorithms that can be implemented and achieve accurate and fast focusing. Every one will have drawbacks as there are cases where it may fail to address the optimal focus. Results of different algorithms may also vary in the same focal region. This is normal because every one produces accurate results under certain circumstances (noise, background, illumination etc.).

We believe that the best option to succeed the research in the field of focusing, is not only to find the best algorithm but also to use it with the correct conditions. We implemented the proposed algorithms and used the best of them or a combination of them, in different occasions, in order to create an accurate, robust and time efficient auto focus system. Finally, all these algorithms produce relative measurements of focus (focal estimations), which means that the only comparable (between specimens and focal regions) measurement they can produce, is based on the derivative of their output curve. For this reason, a time consuming focus scan is mandatory for these relative measurements to produce arithmetically absolute focusing results.

4.3.2 Absolute Metrics for Focus Quality

As described in the previous section, auto focusing is clearly a relative metric and its accuracy may vary from specimen to specimen. In most cases, when an auto focusing system fails to identify the optimal focal plane, the specimen may suffer from:

- Alternations of the optimal focal plane, even on neighboring images.
- Multiple acceptable focal planes on the same image.
- Poorly exposed images or images with low Signal to Noise Ratio - due to errors in automated exposure and gain procedures - or images with counterproductive content (background).
- Vignetted or unevenly illuminated images.
- Artifacts in the image that may result in errors on focus calculations.

These types of image degradation tend to occur on a small fraction of a dataset, that is too large to survey manually, especially in high-content screening applications [12]. This can be a serious problem for automated digital imaging systems, due to potential loss of useful data.

Resolving these issues by re-configuring the optical setup and/or cleaning the specimen is not always possible, nor an effective solution to the problem. Therefore, a computational procedure needs to be implemented in order to assist those issues. In automated digital imaging, the main challenges that Auto Focusing techniques have to overcome are speed and accuracy. These are two dependent concepts, as obtaining perfectly focused images in different specimens with high accuracy is in most cases feasible, although computationally expensive and -therefore- slow. A multi-algorithm focus validation procedure could be a solution to several of the aforementioned problems, but due to its high computational demands it is inadequate for our design, especially when it has to be executed in every single image capture.

Image focus quality is only well-defined in foreground regions of images. As a result, the majority or previous approaches only enabled computation of the relative difference in quality between two or more images, rather than an absolute measure of quality [12]. An absolute focus metric would be of great importance in automated digital imaging systems, not only for the characterization of the focal plane (focusing), but also for focus correlation between different imaging regions (focusing-necessity). This enables the system to only execute computationally expensive focusing procedures when this is an absolute necessity. In this implementation, we present an absolute metric that evaluates whether the current focal plane needs to be re-focused. By calculating the need for re-focusing, as well as ensuring repeatability, our automated procedures are able to thrive in terms of speed and accuracy.

4.3.3 No-Reference Blur Metric

In absence of a reference, the blur annoyance in an image could be quantified by blurring it - using strong low pass filter - and comparing the variations between neighbouring pixels before and after filtering. High variation between the original and blurred image would indicate that the original image was sharp, while small variation means that the original image was already blurred.

This method, theoretically, provides a dimensionless value describing the blurriness/sharpness of the image, with small blur values representing sharper, thus more focused images. Assuming a global threshold based on the blur value, this metric can be considered valid for all specimens.

Based on this principle, the algorithm of this *no-reference blur metric* can described in detail as follows:

1. Pre-process the input image by blurring in vertical and horizontal direction to obtain the $Sharpred\_image$.
2. Compute the absolute horizontal and vertical gradient for the input image ($diff\_f\_ver$, $diff\_f\_hor$) and for the $Sharpred\_image$ ($diff\_fblur\_ver$, $diff\_fblur\_hor$).
3. Compute the absolute difference between the two images corresponding to the vertical gradients ($diff\_f\_ver$ & $diff\_fblur\_ver$) to obtain $ver\_fminusb$ and the images corresponding to the horizontal gradients ($diff\_f\_hor$ & $diff\_fblur\_hor$) to obtain $hor\_fminusb$.
4. Compute the sum of the values in each image $diff\_f\_ver$, $diff\_f\_hor$ and compare them with the sum of $ver\_fminusb$ and $hor\_fminusb$, accordingly.
5. The difference of the horizontal and vertical sums has to be normalized in order to obtain $bfVer$ and $bfHor$.
6. Finally, the blur value is defined as the more annoying (highest) value among the vertical and horizontal direction. $Sharp\_F$ is equal to maxOf($bfVer$,$bfHor$).

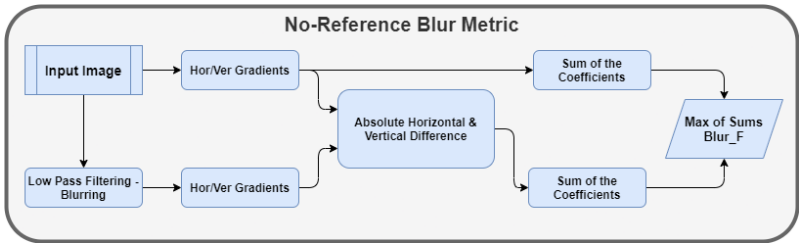

Figure 4.39: No-Reference Blur Metric Block Diagram
Source: A No-Reference Blur Metric Guided Fusion Technique For Multi-Focus Images, Ramy M. Bahy et al. [13]

```
////////////////////////////////////////////////////////////////////////////// blur fusion function
double MicroImageAnalysis::BlurValue(){
    QImage scImage = mImage.convertToFormat(QImage::Format_Grayscale8);//Convert to GrayScale
    cv::Mat img , blurred_image;
    imt::QImageToMat(scImage,img);

//    Pre Proccess
    cv::blur(img,blurred_image,cv::Size(15,15));

//    Compute the absolute difference images
    cv::Mat diff_f_ver = diff_vertical(&img);
    cv::Mat diff_f_hor = diff_horizontal(&img);
    cv::Mat diff_fblur_ver = diff_vertical(&blurred_image);
    cv::Mat diff_fblur_hor = diff_horizontal(&blurred_image);


//    Find the difference between the two vertical & horizontal variations
    cv::Mat ver_fminusb = abs(diff_f_ver - diff_fblur_ver);
    cv::Mat hor_fminusb = abs(diff_f_hor - diff_fblur_hor);

//    Compute the sum of the coefficients to compare the variations from the initial image
   cv::Mat diff_f_ver1 = imt::normalize(&diff_f_ver);
   cv::Mat diff_f_hor1 = imt::normalize(&diff_f_hor);

    double sum_diff_f_ver = cv::sum(diff_f_ver)[0];
    double sum_diff_f_hor = cv::sum(diff_f_hor)[0];
    double sum_ver_fminusb = cv::sum(ver_fminusb)[0];
    double sum_hor_fminusb = cv::sum(hor_fminusb)[0];

//    Normalize to [0,1]
    double bfVer = (sum_diff_f_ver - sum_ver_fminusb) / sum_diff_f_ver;
    double bfHor = (sum_diff_f_hor - sum_hor_fminusb) / sum_diff_f_hor;

//    Return the largest blur value
    double Blur_F = cv::max(bfVer, bfHor);
    return Blur_F;
}
```

Figure 4.40: No-Reference Blur Metric Algorithm
Source: C++ No-Reference Blur Metric Implementation

Results Figures [4.41, 4.42, 4.43] present the results of *No-Reference Blur Metric* algorithm compared with the best *Relative Auto Focus* Algorithm - Mid-Frequency Discrete Cosine Transform (MDCT). The samples were produced by focus scanning in different imaging regions of the same specimen. The gray-scale image in each figure is the best focused image as selected by the MDCT algorithm and does not always match the Blur Metric selection.

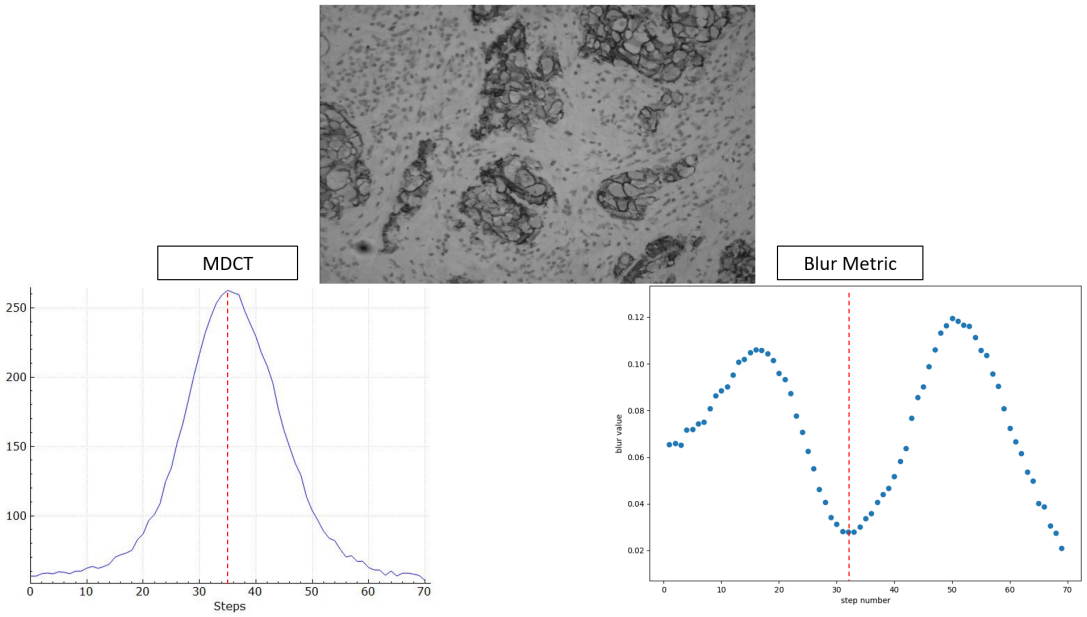

Figure 4.41: Blur Metric vs MDCT Sample 1
Source: No-Reference Blur Metric Results

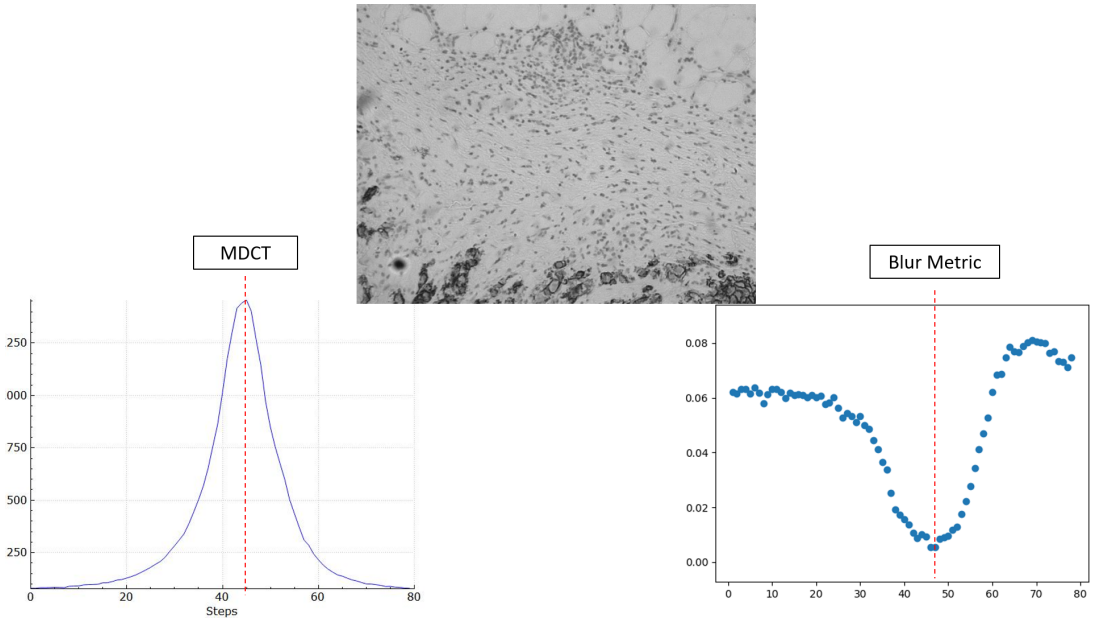

Figure 4.42: Blur Metric vs MDCT Sample 2
Source: No-Reference Blur Metric Results

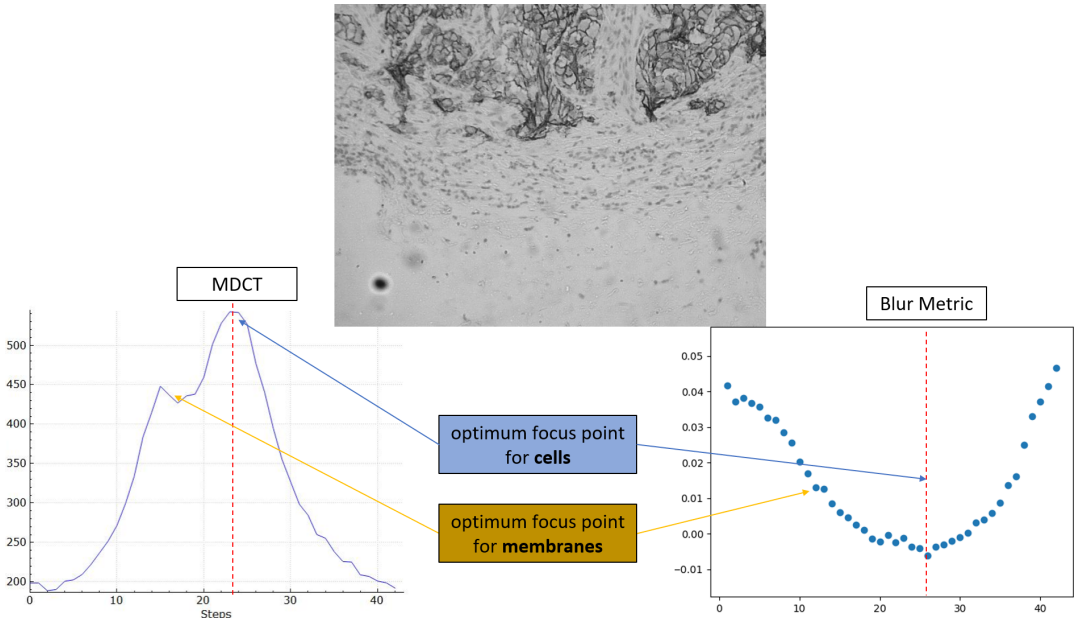

Figure 4.43: Blur Metric vs MDCT Sample 3
Source: No-Reference Blur Metric Results

It is important to notice that the Blur Metric algorithm produces results in the same scale across all samples, contrary to the MDCT algorithm which scales its output according to the content of the image. When comparing the two algorithms, the MDCT exhibits very robust behaviour, while the Blur Metric algorithm's performance displays these 3 main drawbacks:

- Inability to consistently select the best focal plane
- Possibility to select a (non-optimum) focal plane corresponding to the global minimum, instead of the local minimum (Figure [4.41])
- Inability to identify multiple optimal focal planes in the same imaging region, when present (Figure [4.43])

In order to counteract the problem of selecting a non-optimum focal plane due to the presence of a global minimum - different from the local minimum which would yield the desired result - a checking procedure has to be implemented. This procedure can use the information produced by consecutive images and identify whether it lies in the correct region of the function. The downside of this method is the need to know the distribution of the values, therefore requiring a full scan of the image to produce meaningful results.

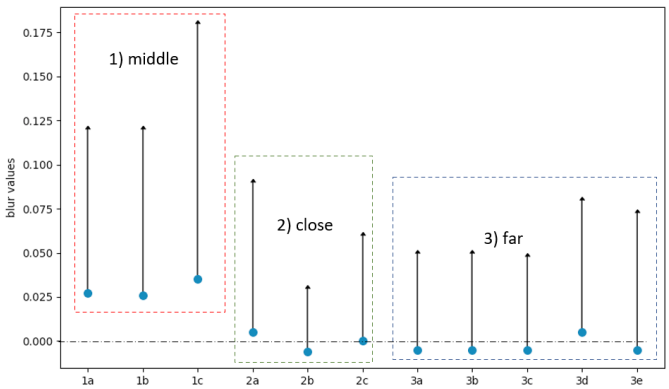

Figure 4.44: No-Reference Blur Metric Results Variation
Source: No-Reference Blur Metric Results

Figure [4.44] presents the variations of the Blur Metric values in three different illumination conditions, in this case Condenser-Specimen distances (middle, close, far). For each illumination condition, this figure shows the results corresponding to different imaging regions of the same specimen. Dots in this figure represent the optimal focus value produced by the Blur Metric and arrows the range in which the focal planes remain acceptable to the human eye.

This algorithm is able to produce satisfactory absolute focus values, referring to the same specimen given stable illumination conditions, although not always perfect (e.g. defocused or negative). At the same time, due to the nature of this algorithm, depending on the distribution of the values produced by the Blur Metric, this absolute focus value might not be unique in other imaging regions. In this case, the algorithm could yield a focal plane selection different from the optimum, as shown in Figure [4.45]. This means that its results are relative to each specific image and cannot be trusted for other imaging regions, unless it is recalculated.

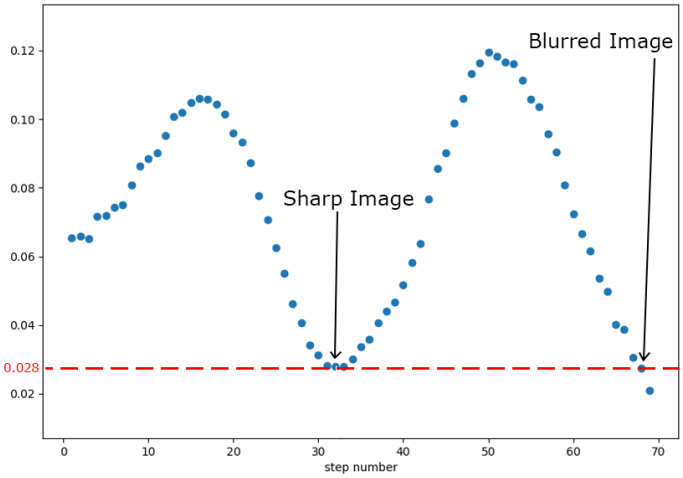

Figure 4.45: No-Reference Blur Metric Results Inconsistency
Source: No-Reference Blur Metric Inconsistency

Overall, this algorithm does not provide an ideal solution to our Absolute Focal Plane selection problem, due to its inconsistency with respect to illumination conditions and variations across specimens and imaging regions. Ideally, we would like to be able to define a specific threshold value that would yield convenient results among all imaging regions and illuminated conditions.

4.3.4 Gradient Based Metrics

The Gradient Based Metrics are implemented in order to gain control over the optimal focal plane estimation with an absolute value. The idea for these implementations is based on the Histogram of Gradients (HoG) and its ability to provide a robust classification of an image's content, in terms of focal variations. This could happen by observing the energy distribution of an image's first derivative, in the different parts of the histogram. It can become a powerful tool in focus measurements during autofocusing (AF) process and in the estimation of the absolute focus value of a single image.

In general, the first derivative based techniques, in digital image processing, are widely used for edge detection algorithms, and due to their computational simplicity and inherent parallelism they can be implemented in GPUs for real time image processing. In our case, we have been experimenting with the HoG in order to extract different types of information about our specimen sharpness. In this section we present three of the most promising implemented metrics, as follows:

- Mean value of "j" highest Gradients.
- Mean value of Mid-Bandpass from HoG.
- Mean Standard Deviation of HoG.

These methods, theoretically, provide dimensionless values describing the sharpness of an image, with high values representing sharper, thus more focused images. Assuming a global threshold based on these values, this metric can be considered valid for all specimens.

Pre-Processing Every single method we analyze is thereof based on the gradients of the input image. We firstly obtain the grayscale version from the input image (from RGB) and then we prepare the 2D gradient's map as shown in the following equation [4.3.4.1].

$$g(x,y) = \frac{2 \cdot img(i,j) - img(i-1,j) - img(i,j-1)}{2} \tag{4.3.4.1}$$

```
double MicroImageAnalysis::Gradients(QImage scImage){
    QImage gray = mImage.copy().convertToFormat(QImage::Format_Grayscale8);
    mImageMat = new cv::Mat;
    imt::QImageToMat(gray,mImageMat);

    cv::Mat gradHorizontal = diff_horizontal(mImageMat);
    cv::Mat gradVertical = diff_vertical(mImageMat);

    cv::Mat gradient = gradHorizontal + gradVertical;
    gradient = gradient/2;
}

//# function for vertical matrix element subtraction
cv::Mat MicroImageAnalysis::diff_vertical(cv::Mat *arrayA){
    cv::Mat arrayResult = cv::Mat::zeros( arrayA->size(), arrayA->type());
    for (int j = 0 ; j < arrayA->cols; j++)
        for (int i = 1 ; i < arrayA->rows; i++)
            arrayResult.at<uchar>(i,j) = uchar(abs(arrayA->at<uchar>(i,j) - arrayA->at<uchar>(i-1,j)));
    return arrayResult;
}

//# function for horizontal matrix element subtraction
cv::Mat MicroImageAnalysis::diff_horizontal(cv::Mat *arrayA){
    cv::Mat arrayResult = cv::Mat::zeros( arrayA->size(), arrayA->type());
    for (int j = 1 ; j < arrayA->cols; j++)
        for (int i = 0 ; i < arrayA->rows; i++)
            arrayResult.at<uchar>(i,j) = uchar(abs(arrayA->at<uchar>(i,j) - arrayA->at<uchar>(i,j-1)));
    return arrayResult;
}
```

Figure 4.46: C++ implementation of equation 4.3.4.1

We then sort the values of the gradient's map in descending order into a 1D table **sorted(g)**, as shown in Figure [4.47], in order to create the Histogram of Gradients (HoG) **hist(g)**. This histogram presents the number of pixels (un-normalized probability) for each gradient level.

```
typedef std::vector<QPair<cv::Point, double>> SortingData;

    static SortingData* sortImage(cv::Mat *imgIn){
        cv::Mat *img = new cv::Mat;
        imgIn->convertTo(*img,CV_64F);
        cv::Mat sortedImg = cv::Mat::zeros(cv::Size(1,img->rows*img->cols),CV_64F);
        int counter = 0;
        SortingData *sortData = new SortingData;
        for(int row=0 ; row<img->rows ; row++){
            for(int col=0 ; col<img->cols ; col++){
                cv::Point p = cv::Point(col, row);
                double value = img->at<double>(p);
                sortedImg.at<double>(cv::Point(0,counter)) = img->at<double>(p);
                QPair<cv::Point, double> dataPair(p,value);
                sortData->push_back(dataPair);
                counter++;
            }
        }
        std::sort(sortData->begin(), sortData->end(), [=]( QPair<cv::Point, double> a ,  QPair<cv::Point, double> b){
            return a.second > b.second;
        });
        return sortData;
    }
```

Figure 4.47: C++ implementation of image sorting

After the Pre-Process stage of the Gradient Based Metrics, our dataset consist of the *inputImage*, the *imageGradients* and the *HoG* as shown in Figure [4.48].

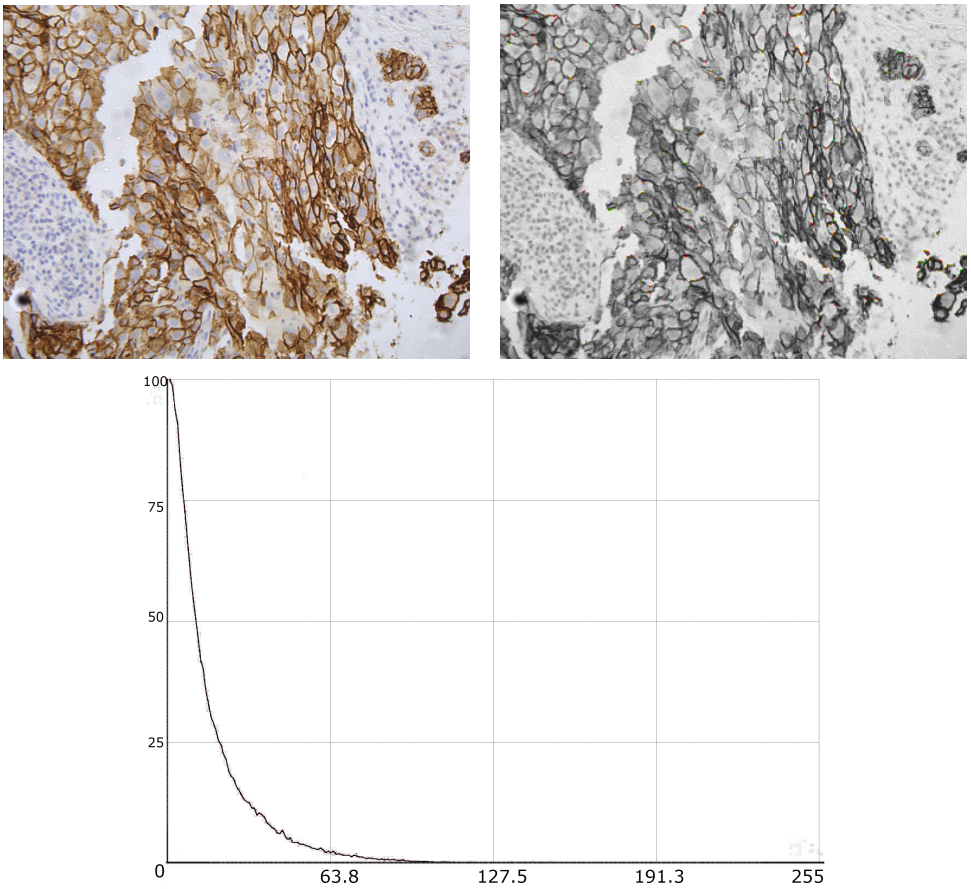

Figure 4.48: (a) DAB Specimen - Input(*inputImage*), (b) DAB Specimen - Gradients(*imageGradients*), (c) DAB Specimen - Histogram of Gradients(*HoG*)

Methods Using the Pre-Processed Histogram of Gradients **hist(g)** and the **sorted(g)** table, we have implemented our three metrics.

- **Mean value of j highest gradients:** We compute the mean ($meanJ$) value of the j pixels with the highest gradient values at each focus depth. Using $meanJ$, derived by the Equation [4.3.4.2], we create a focusing index which is affected only by highest gradient values (sharp pixels) and as a result a focusing method that is background (blur) irrelevant.

$$meanJ = \frac{1}{j} \cdot \sum_{g=0}^{j} sorted(g) \tag{4.3.4.2}$$

```
static double getMeanValueOfFirstMax(SortingData *sortData, int firstMax){
    double sum;
    for(int row=0 ; row<firstMax ; row++){
        sum+=sortData->at(row).second;
    }
    return sum/firstMax;
}
```

Figure 4.49: C++ implementation of equation 4.3.4.2

The values j (denoted as $firstMax$ in the code above) we experimented with, are {50},{100} and {200}. Finally, we reconstructed the GradientsImage($imageGradients$) in order to highlight each pixel that belongs to the first 200 highest gradients. The results are shown in Figure [4.50].

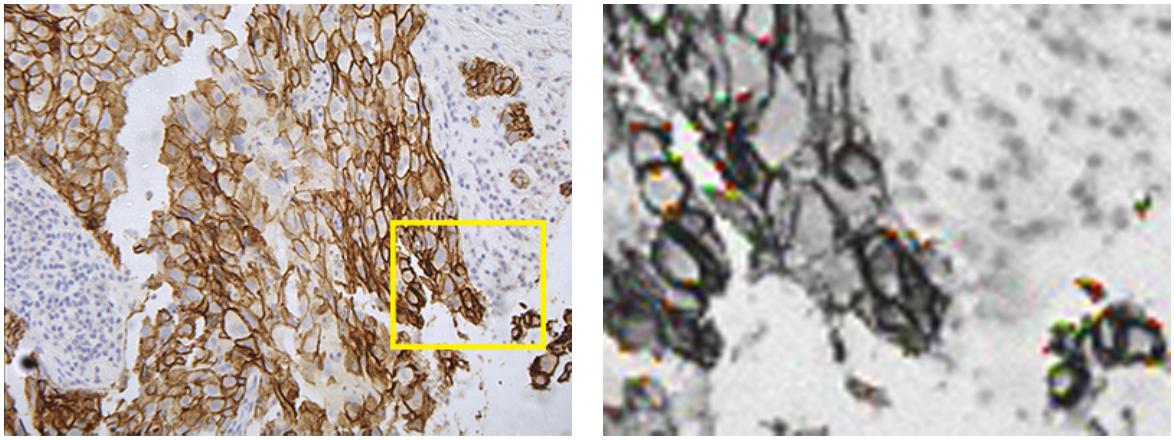

Figure 4.50: (a)DAB Specimen - Selected Region, (b)DAB Specimen - Gradients($imageGradients$) with the 200 highest value pixels highlighted

As shown in the Figure [4.50](b) the highest Gradient values of this image, are presented in a pseudo-color shading, ranging from green to red which represents the gradient values from low to high respectively.

Mean value of j Highest Gradients			
	$meanOfFirstMax50$	$meanOfFirstMax100$	$meanOfFirstMax200$
$DAB\_Specimen$	145.7	137.42	128.275

Table 4.1: Mean value of 50, 100, 200 Highest Gradients

Table [4.1] presents the outcome of our Mean value of j highest gradients Metric given the image of Figure [4.50](a) as an input and executed for three different j or $FirstMax$: 50, 100, 200.

- **Mean value of Mid-Bandpass from HoG:** In this method, we firstly divided the histogram in five bands, depending on the gradient levels we wanted to separate. We then classified the lowest and highest bands to describe the background and noise respectively and the middle bands to describe the content and sharpness of the image. To create a focus index, we computed the mean value of the existing gradients, weighted by the pixel count of the given band.

$$meanBand = \frac{1}{\sum_{g=bandStart}^{bandEnd} hist(g)} \cdot \sum_{g=bandStart}^{bandEnd} (g \ \forall \ hist(g) \neq 0) \tag{4.3.4.3}$$

```
static double getMeanOfBandPass(cv::Mat *imgIn, int bandMin, int bandMax){
        double mean = 0.0;
        double sum = 0.0;
        double cntr= 0.0;
        for(int row=0 ; row<imgIn->rows ; row++){
            for(int col=0 ; col<imgIn->cols ; col++){
                uchar pxl = imgIn->at<uchar>(row,col);
                if(pxl>=bandMin && pxl<=bandMax){
                    sum+=pxl;cntr+=1;
                }
            }
        }
        if(cntr!=0) mean = sum/cntr;
        return mean;
    }
```

Figure 4.51: C++ implementation of equation 4.3.4.3

Using this method we tried to classify the focal characteristics of a given imaging region from our DAB Specimen, in two focal regions. One that is sharp and one that is blurred, as shown in the Figure [4.52] below.

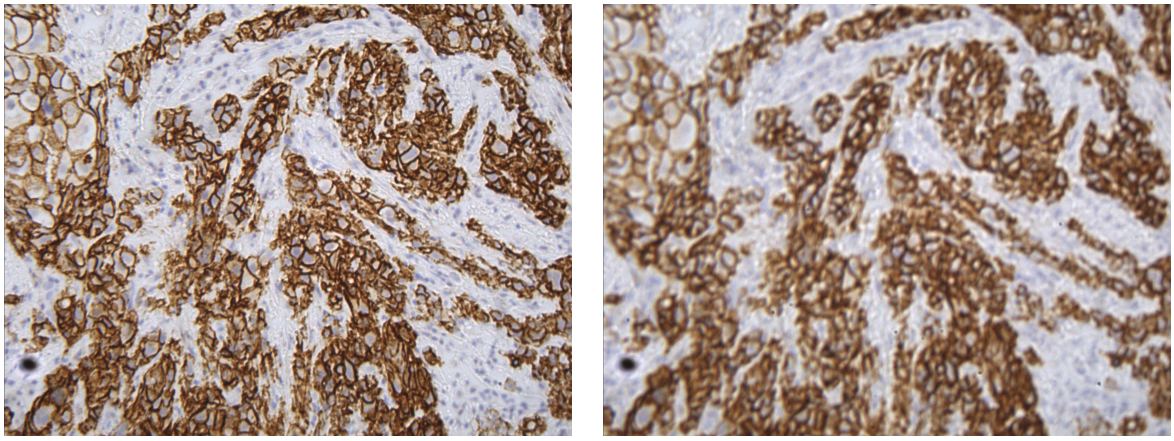

Figure 4.52: (a)DAB Specimen - Sharp Image, (b)DAB Specimen - Blurred Image

The bands we experimented with, are $\{0-15\}$, $\{16-30\}$, $\{31-50\}$, $\{51-100\}$ and $\{101-255\}$ and we classified *Background*, *BlurObjects*, *SharpObjects*1, *SharpObjects*2 and *Noise* respectively, as shown in Figure [4.53] and Table [4.2].

Mean values of Mid-Bandpass from HoG / Pixels of each Band					
	Background	*BlurObjects*	*SharpObjects*1	*SharpObjects*2	*Noise*
SharpImage	6.84506/63224	22.002/27705	39.0935/16136	67.1534/10402	112.15/733
BlurredImage	6.50081/86920	21.4481/24535	36.8438/6426	56.0564/319	0/0

Table 4.2: Mean values of Mid-Bandpass from HoG / Pixels of each Band

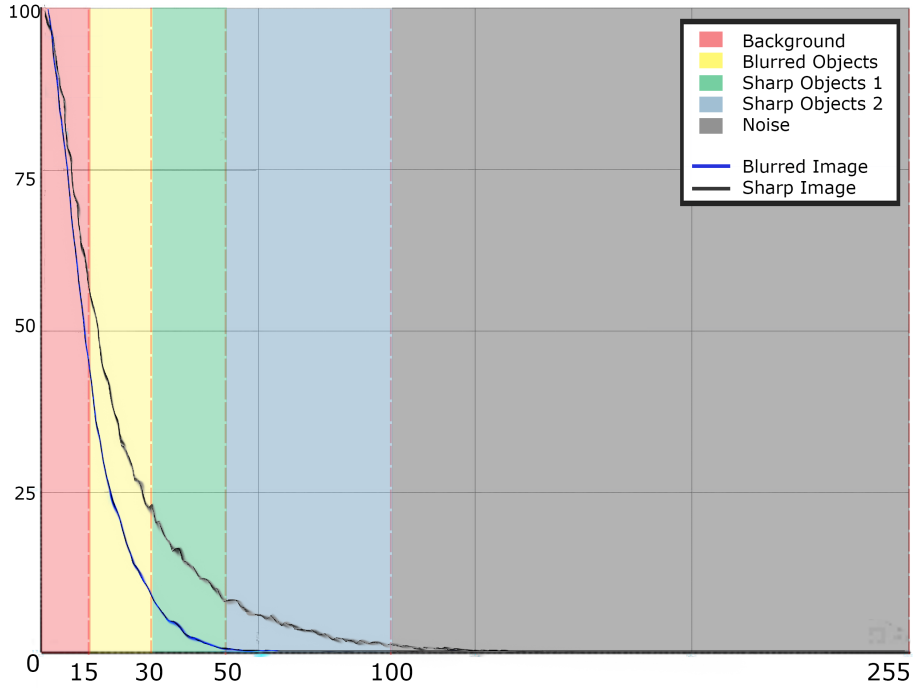

Figure 4.53: DAB Specimen - Histogram of Gradients(HoG) - Bands

As shown in Figure [4.53] and Table [4.2], selecting a single useful band (e.g. $SharpObjects1$) and processing it with the Mean value of Mid-Bandpass from HoG Metric, we were able to yield a focus index that is only relevant to the selected focal characteristic (band) of the input image. That essentially means that this metric is noise and background irrelevant.

- **Mean Standard Deviation of HoG:** In order to extract the histogram's mean Standard Deviation (**meanStd**), we firstly needed to calculate the mean gradient (**meanHoG** Equation [4.3.5.1]). By utilizing the HoG's standard deviation as a focus index, we observed that its width is directly associated with the sharpness of the image. As the width of the **meanStd** increases, the image gained sharper characteristics. We could therefore scan the z-axis in order to find its highest value, which corresponded to the optimal focal plane of the input image.

$$meanStd = \sqrt{\frac{1}{\sum_g hist(g)} \cdot \sum_g ((g - meanHoG)^2 \cdot hist(g))} \tag{4.3.4.4}$$

The results of this method, produced by providing the Sharp and the Blurred Images (Figure [4.52]) as inputs, are shown in the Table [4.3] below.

```
static double histogramSTD(QMap<uchar, double> histogram){
    double propCntr = 0;
    double mean = 0;
    foreach(int i, histogram.keys()){
        double prop = histogram.value(i);
        double val = static_cast<double>(i);
        mean+=val*prop;
        propCntr+=prop;
    }
    mean = mean/propCntr;
    double std = 0;
    foreach(int i, histogram.keys()){
        double prop = histogram.value(i);
        double val = pow(static_cast<double>(i)-mean,2);
        std+=(val*prop);
    }
    std = sqrt(std/propCntr);
    return std;
}
```

Figure 4.54: C++ implementation of equation 4.3.4.4

	$MeanGradientsSTD$
$SharpImage$	20.6143
$BlurredImage$	9.88571

Table 4.3: Mean Gradients STD

Finally, a focus scan using these methods versus the Mid-frequency Discrete Cosine Transform is shown in Figure [4.55] below. As always, the motion control system uses Z Resolution of 78.125 nm, the images distance is 10 steps x Z Resolution or 781,25 nm and the full scan focal depth of 31.25 um.

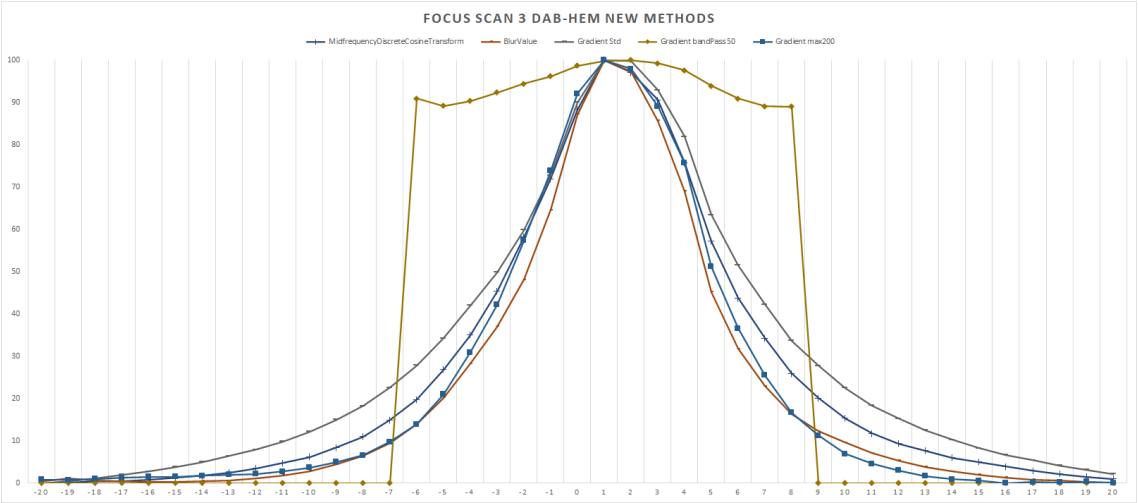

Figure 4.55: Gradient Based Methods Focus Scan

The graph of Figure [4.55] presents the performance of the proposed methods, compared with the selected Mid-frequency Discrete Cosine Transform. Due to their consistency, these methods can clearly be used for our focusing application. Moreover, the width of each curve indicates its (in)dependence from noise and background. When a curve is broad, its content is not only related to sharpness but also heavily affected by background blurriness and/or noise. On the other hand, a narrow curve corresponds to focal indices which are background and noise irrelevant.

*GradientBandPass*50 or *SharpObj*1 (Equation [4.3.4.3] {band [31-50]}), does not behave similarly to the other metrics in the graph. This happens because it produces values only if a certain amount of pixels contributes to the selected band. Thus, the focal estimation resolution remains background and noise irrelevant (due to band selection), but with exceptional accuracy thanks to its absolute characteristics.

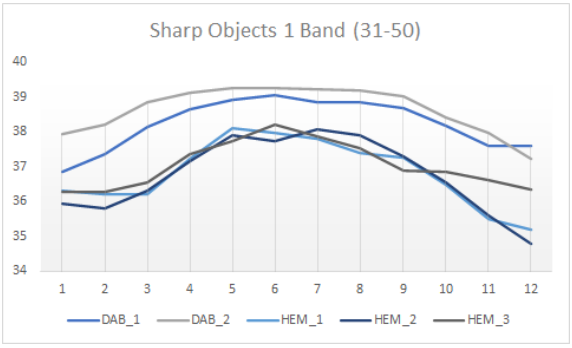

Figure 4.56: Gradient Based *SharpObj*1 Relativity over 5 Focus Scans

Despite the fact that these methods can estimate the optimal focal plane with ease, they can not robustly predict its absolute value because of their generic setup. Even the most promising one, *SharpObj*1, still succumbs in relativity, as shown in Figure [4.56]. In order to produce absolute focal plane estimations, dynamic tuning of each prescribed method is mandatory. For example, *SharpObj*1 needs to dynamically define its band range with respect to the image's content. A computational approach to this dynamic configuration problem, would lead to an efficiency abatement. On the other hand, a Neural Network could easily handle these complex procedures. Nonetheless, the addition of a Neural Network in this real time decision making problem, would be an overkill.

4.3.5 Multi-Method Fusion

Alternatively to the Neural Network tuning approach, we propose the use of Multi-Method Fusion for extracting an absolute focal estimation value. While experimenting with the datasets produced from the Gradient Based Methods, we concluded on plotting the sum of pixels contributing to the following bands:

- $GradientBandPass50$ or $SharpObj1$ (Equation [4.3.4.3] {band [31-50]})
- $GradientBandPass100$ or $SharpObj2$ (Equation [4.3.4.3] {band [51-100]})

versus the mean value of the Histogram of Gradients ($meanHoG$) (Equation [4.3.5.1]), as shown in Figure [4.57].

$$meanHoG = \frac{1}{256} \cdot \sum_{g=0}^{255} HoG(g) \tag{4.3.5.1}$$

Figure [4.57] presents how different data sets with sharp and blurred images behave in the plane mentioned above.

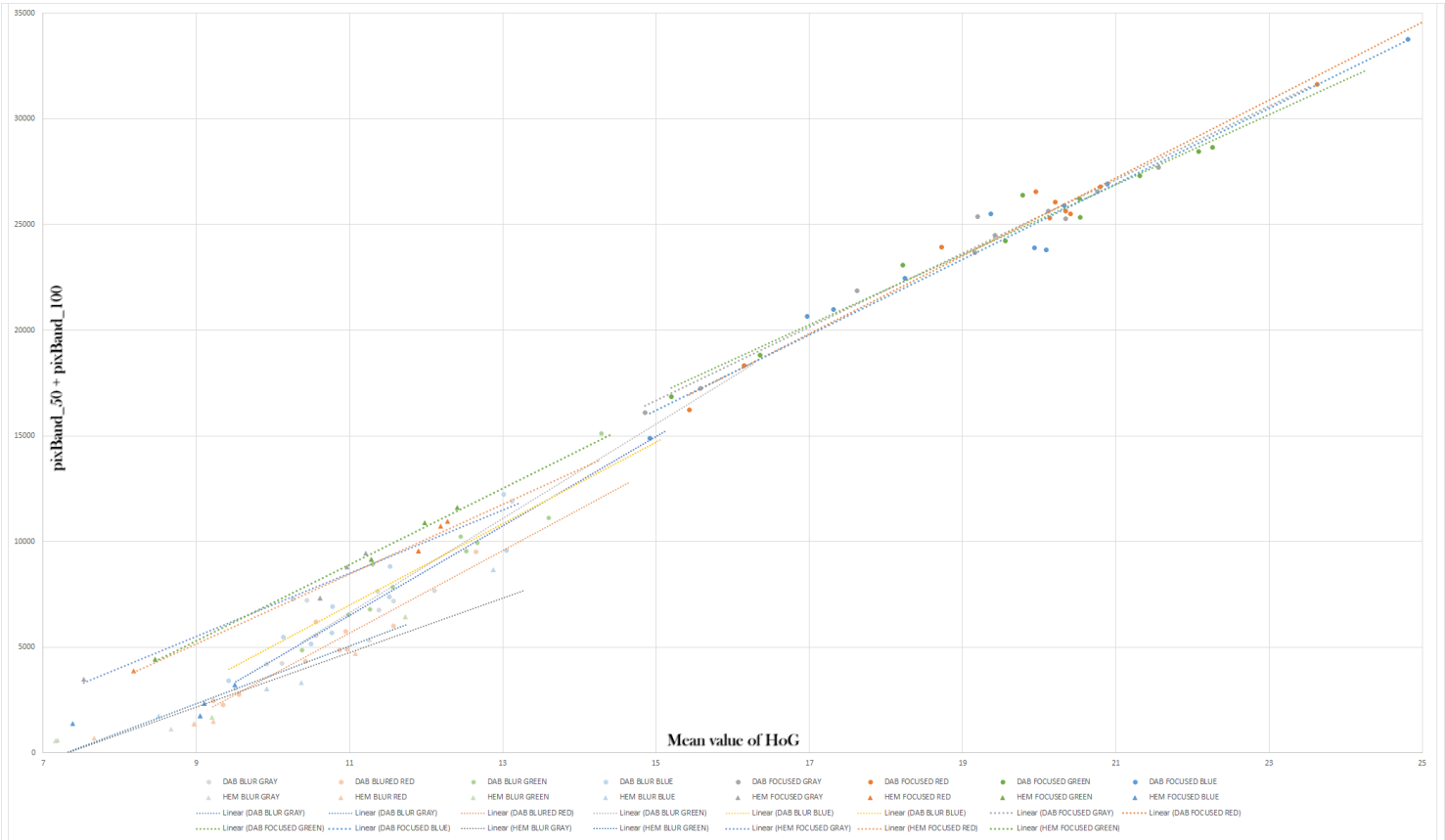

Figure 4.57: Gradient Based Absolute Metric Graph

The different data sets analyzed for the purpose of this thesis are DAB and Hematoxylin stains in Pathologoanatomical specimens, captured in ten different imaging regions each (2x10 RGB images). In every imaging region, we selected the most Focused and least Focused RGB images for our *Focused* and *Blurred* datasets respectively, using our Focus Scan procedure (2x20 RGB images). Each RGB image is then split to its three monochrome channels (Red, Green, Blue) and also represented as a single grayscale image (*Gray*) constructed from weighted merging the three (RGB) channels (4x40 single channel images), as shown in Figure [4.58].

Figure 4.58: Gradient Based Absolute Metric Graph Data Sets

Thresholds, based on a big data-set of Focused and Defocused images, are applied to the graph to bound a special area. Every single point($meanHoG$,$pixBand\_50 + pixBand\_100$) inside this area can be considered a focused image and every one that it is outside of the bounded area, can be considered blurred image, as shown in Figure [4.95].

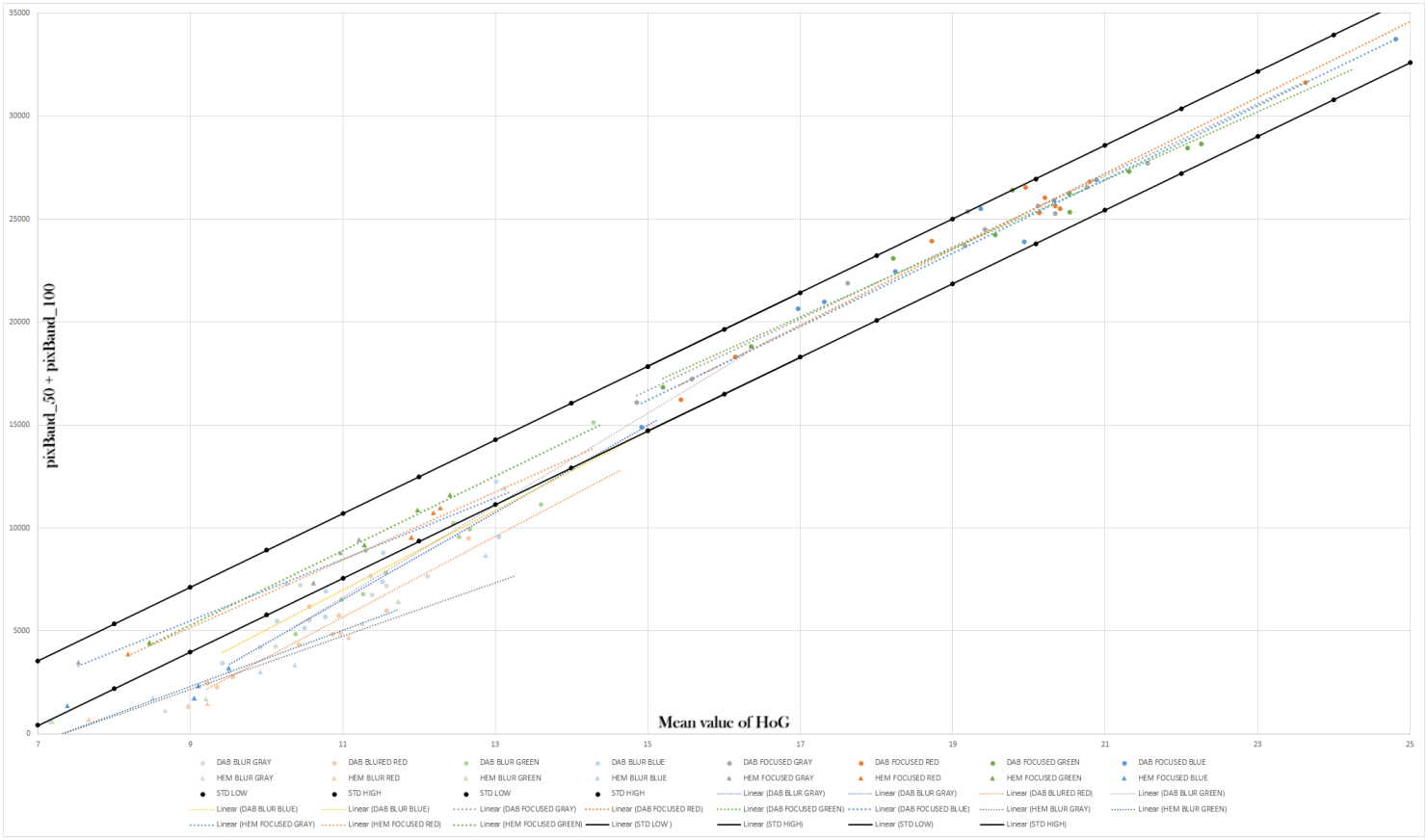

Figure 4.59: Gradient Based Absolute Metric Thresholded Graph

This thresholding method is proven to be a reliable and robust absolute focus criterion so far. Our main goal is to bound the axes of this graph with a ratio that can describe, with absolute values, how focused an image is, based on the deviation of each dataset from the thresholds. The thresholds applied and shown in Figures [4.95, 4.61, 4.63], are selected as the maximum distance a point can have from the Focused center line, to describe with confidence that the point refers to a focused image, as shown in Figure [4.61]. This center line is calculated from the mean values of all the focused datasets analyzed and it appears to be exactly in the center of the two black upper and lower bounds, as shown in Figure[4.60].

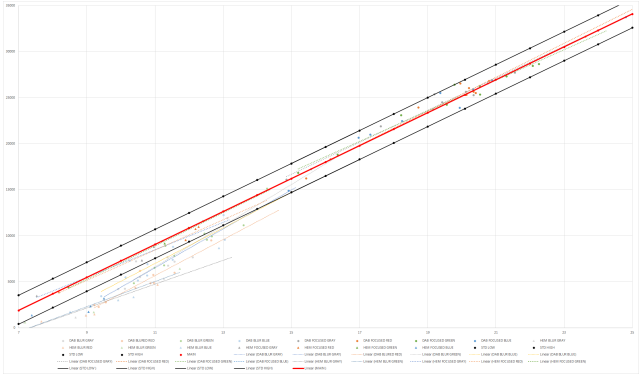

Figure 4.60: Gradient Based Absolute Metric Thresholded Graph - Center Line

Figure [4.61], presents all the focused datasets of our analysis, being bounded by our two threshold lines.

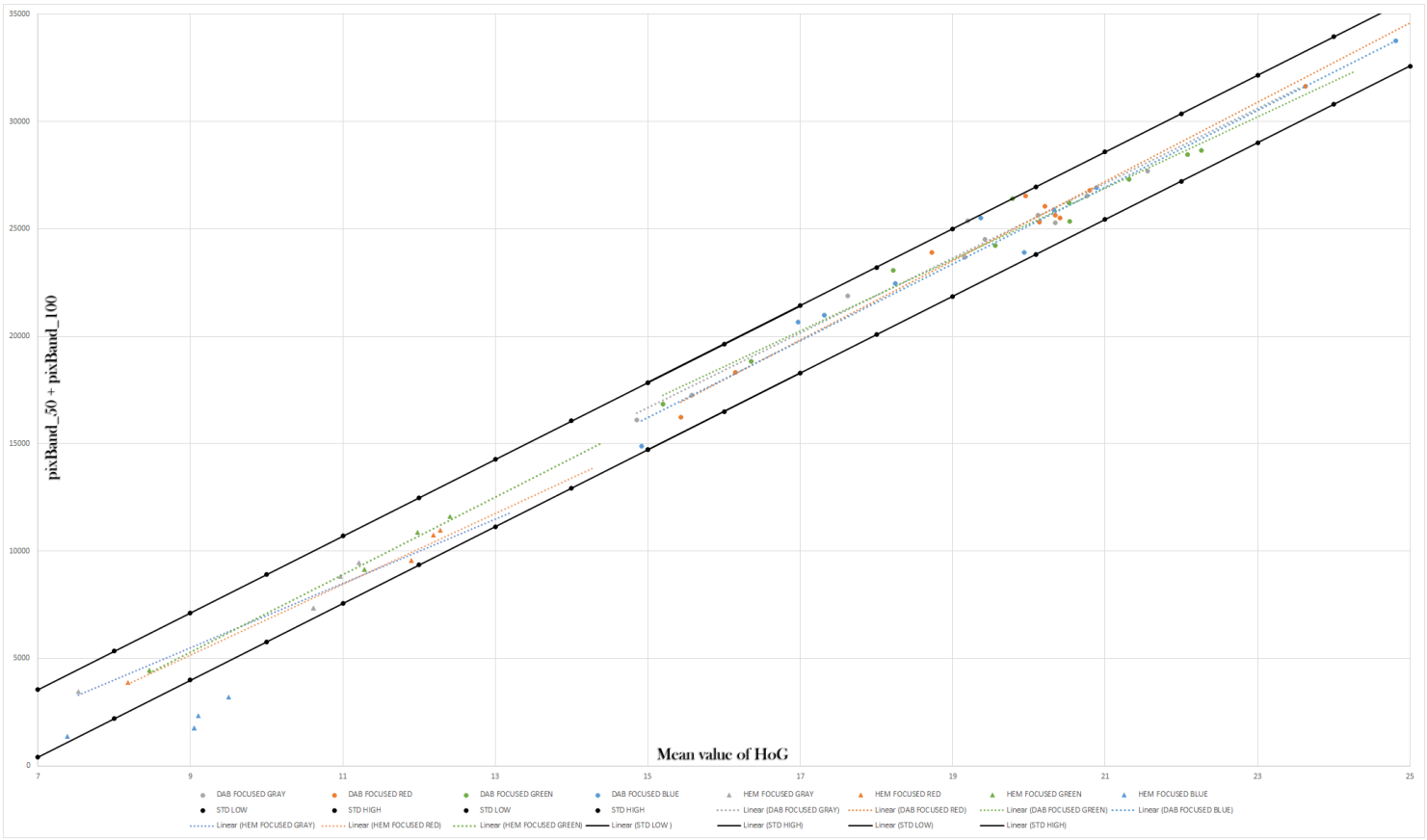

Figure 4.61: Gradient Based Absolute Metric Thresholded Graph - Sharp Images

In this Figure [4.61], we can notice focused images of DAB staining dominating the top right part of our bounding region and Hematoxylin staining images dominating the bottom left. This happens because of the focal characteristics of the specimen where each staining applies to. Specimens stained with DAB, are usually sharper and have sufficient depth, due to the fact that DAB stains the membranes of the cells, thus enhancing the contrast of the overall image. On the other hand, Hematoxylin stained specimens are usually blurry and have small depth, due to the fact that Hematoxylin stains the cell's core and not the membranes, thus it has peak intensity in the center of a cell that fades towards the membrane.

Moreover, it is noticeable that the blue channel of the focused Hematoxylin specimens, not only has the lowest values in the graph, but also produces results that are noisy and out of the threshold bounds. This happens because Hematoxylin bluish color merges with the white background when observed using the blue channel of our image, and as a result its gradients will produce very low and noise relevant values compared to the other channels of our datasets, as shown in Figure [4.62].

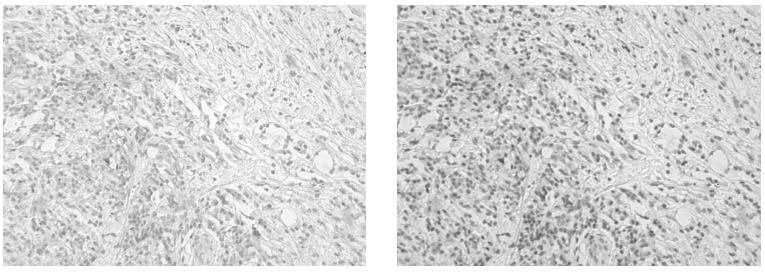

Figure 4.62: Focused Hematoxylin Specimen (a) Blue Channel, (b) Green Channel

Figure [4.63], presents all the blurred datasets of our analysis, not being bounded by our two threshold lines.

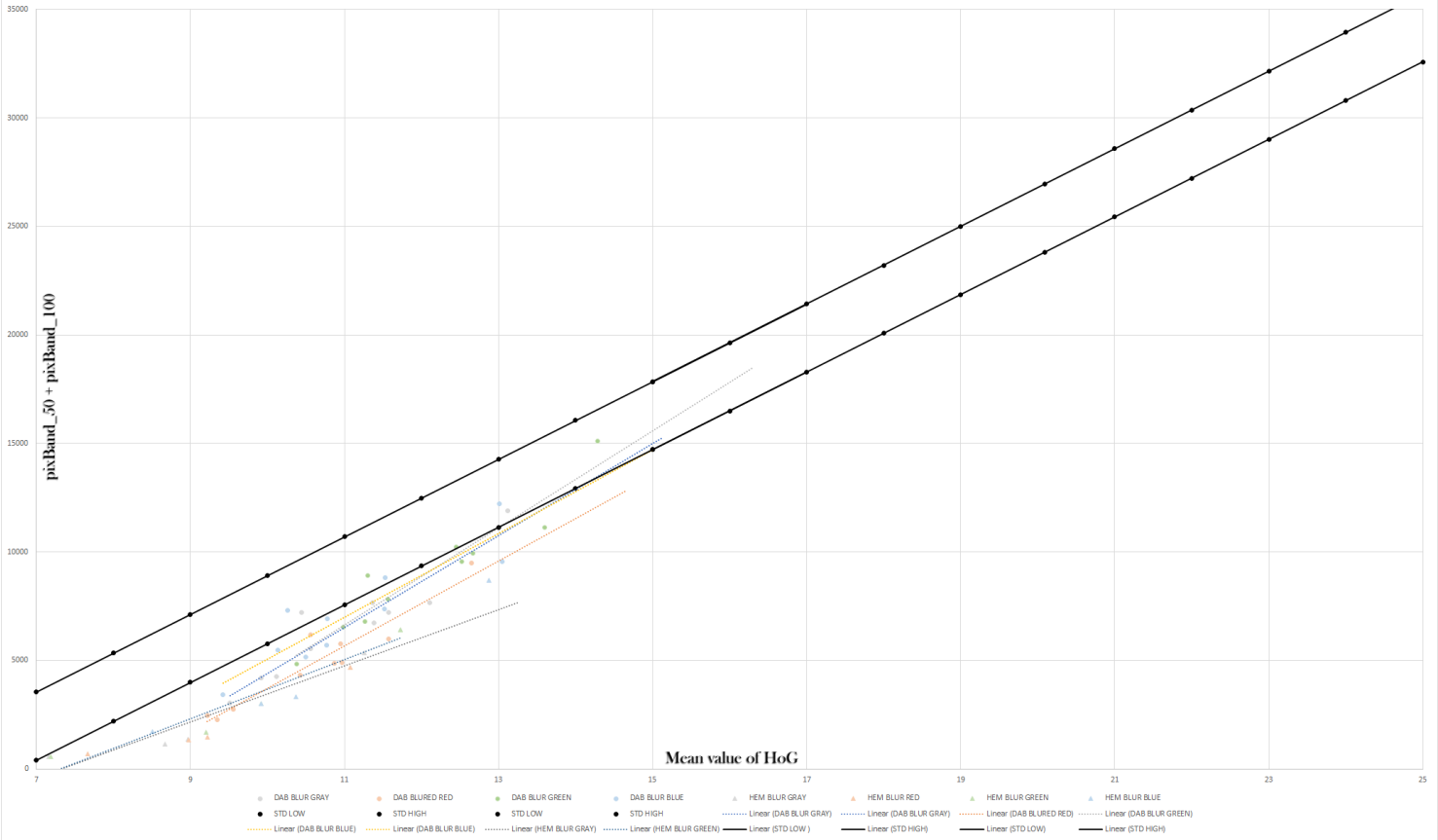

Figure 4.63: Gradient Based Absolute Metric Thresholded Graph - Blurred Images

Examining Figure [4.63], we observed cases of cross taking between our Focused and Blurred regions, especially when the blurred image's content contribution to the selected bands is significant. This occurs in cases where, the content of a blurred image in a specific color band, produces sharp variations due to noise or content artifacts, as shown in Figure [4.63].

Figures [4.64, 4.65] shown below, presents images produced from Focus Scan and classified from our metric as *Focused* (a,b) or *Blurred* (c,d).

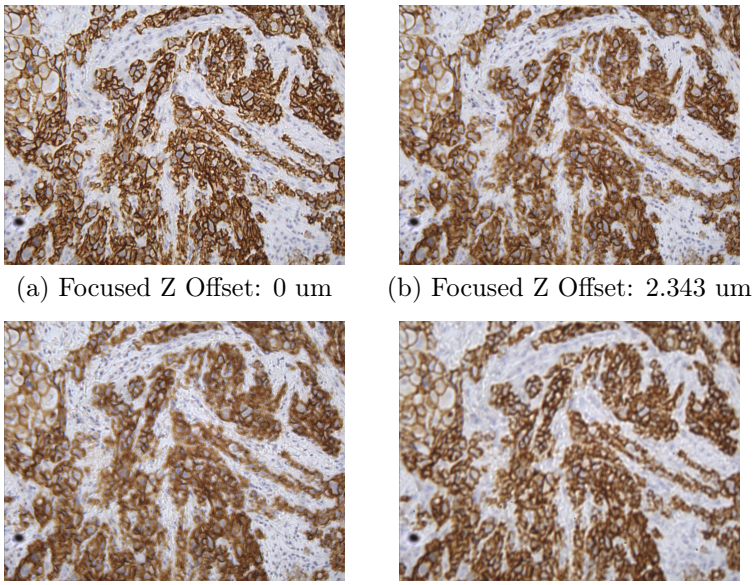

(a) Focused Z Offset: 0 um (b) Focused Z Offset: 2.343 um

(c) Blurred Z Offset: 3.906 um (d) Blurred Z Offset: -3.906 um

Figure 4.64: Gradient Based Absolute Metric Image Classification DAB

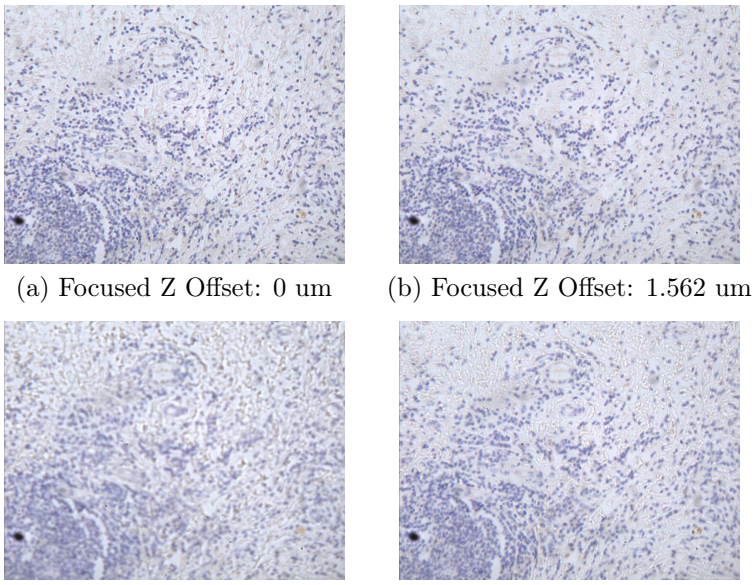

(a) Focused Z Offset: 0 um (b) Focused Z Offset: 1.562 um

(c) Blurred Z Offset: 3.906 um (d) Blurred Z Offset: -3.125 um

Figure 4.65: Gradient Based Absolute Metric Image Classification HEM

The outcomes shown in Figures [4.64, 4.65], are based on our experimental global thresholing.

In conclusion, this Gradient Based approach produces an easy to implement toolkit that can lead to topographical and focal measurement or even segmentation. Finally, due to its computational simplicity it can be implemented in GPU and therefore, achieve an overall real time experience.

4.4 Z Stack Processing

The concept of multi-focus image fusion emerges from the limitations in terms of depth of field in imaging, especially in Wide-Field Microscopy. Given the advances in sensor technology and computational power, it is possible to capture multiple images of the same scene, carrying redundant or complementary information due to sensor differences. Therefore, one can capture images at different focal planes and combine them to produce one sharp image, incorporating focused information at various depths of the scene. This process, in principle consists, of two main stages:

- **Out of focus extraction**, where the out-of focus information from each image is identified and disregarded.
- **Multi-focus Image Fusion (MIF)**, where the remaining (in-focus) information from each image is combined to create one sharp image.

The set of images corresponding to the different focal planes is typically called *Z-Stack* and this whole procedure is therefore referred to as *Z-Stack Processing*. In this section we present our approach on Z Stack Processing, as implemented within the scope of this Thesis.

4.4.1 Introduction to Multi-Focus Image Fusion (MIF)

Over the last years, several methods of image fusion have been implemented, each with its own advantages and disadvantages. These methods can generally be classified as *spatial domain based* and *transform based*, among with others involving Neural Networks (NN) [30]. In our implementation, we develop a Discrete Wavelet Transform (DWT) based multi-resolution fusion technique. DWT methods have proved that they can provide better spatial and spectral localisation than their counterparts and are therefore widely adopted in various fields, including Multi-Focus Image Fusion [32]- [34].

In DWT based Image Fusion, the first step is to transform the images to their multi-resolution representation, according to the Discrete Wavelet Transform. The composite multi-resolution representation is then created using a specific fusion rule. The final image is then reconstructed using the Inverse DWT.

The fusion rule is key to performance for this method. The simplest method is the *Maximum Selection* [35], based on selecting the largest absolute wavelet coefficient as the coefficient in the fused image at the corresponding location. A more elaborate approach involves processing each spectral band individually [36]. The most important part is to accurately identify in-focus information inside each image. As presented in [37], this can be best achieved by dividing low and high frequency bands in sub-bands and processing them using different window-based fusion rules, followed by a consistency verification step. This method was used as the basis of our proposed algorithm, which can be conveniently broken down into the following steps:

- **DWT Transform & Band Splitting**. Decompose each image into its spectral features or *Low* and *High* frequency components, using the DWT.
- **Fusion**. Combine the coefficients of the Z-Stack images for each pixel and colour channel, using a *Max Energy* based scheme for the Low frequencies and a *Maximum Sharpness* based scheme for the High frequencies.
- **Verification**. Verify the final coefficients using a window-based consistency verification process, for each colour channel, in order to ensure homogeneity and overcome the presence of noise.
- **IDWT**. Create the final image by performing Inverse Discrete Wavelet Transform (IDWT) on the resulting coefficients.

As we know that for multi-focus images, each of them has some clear information about the same scene but none of them is sufficient in terms of its information contents. The main idea of their fusion is to select sharply pixels from source images and combine them together to reconstruct the superior image in which all the pixels can be clearly focused.

4.4.2 DWT Transform & Band Splitting

High Frequencies consist of horizontal, vertical and diagonal components. This procedure, was held using the Single-level discrete 2-D wavelet transform function Matlab provides thought Wavelet Toolbox [6]. This function computes the approximation coefficients matrix cA and details coefficients matrices cH, cV, and cD (horizontal, vertical, and diagonal, respectively), obtained by wavelet decomposition of the input matrix X [6]. The 'wname' string contains the wavelet name. The syntax of this function is shown in Equation [4.4.2.1].

$$[cA, cH, cV, cD] = dwt2(X, wname) \tag{4.4.2.1}$$

The following Figure [4.66] describes the basic decomposition steps the Single-level discrete 2-D wavelet transform algorithm executes:

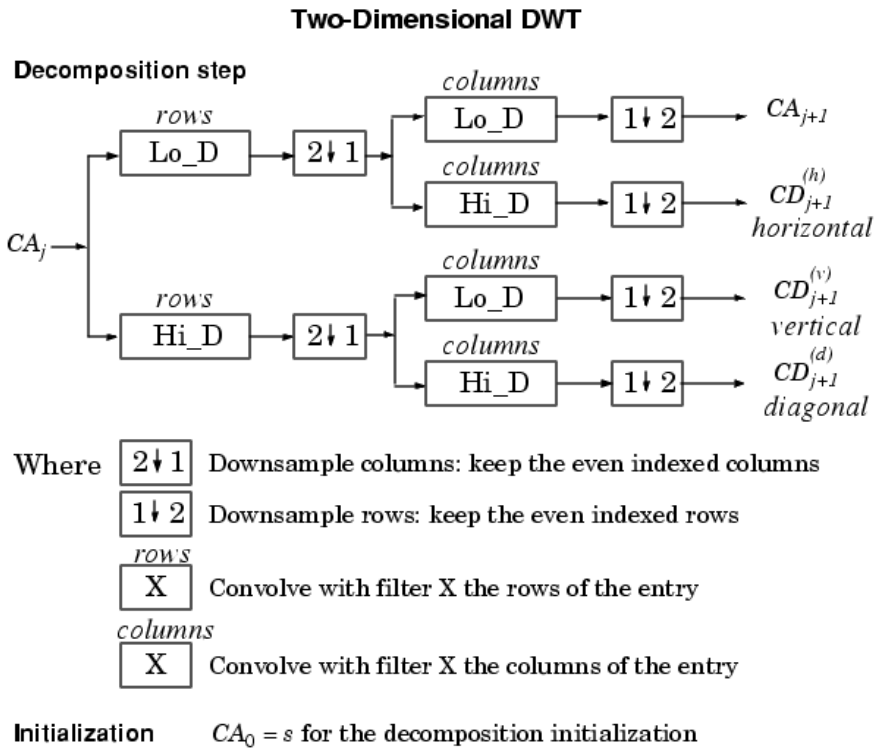

Figure 4.66: Single-level discrete 2-D wavelet transform Algorithm
Source: Wavelet Toolbox [6]

Figure [4.67] presents the Matlab implementation of DWT in an array of multichannel (RGB) and multidepth (Z position) images (`imageArray`).

```
for k=1:N
    [Ra(:,:,k),Rh(:,:,k),Rv(:,:,k),Rd(:,:,k)]=dwt2(imageArray(:,:,1,k),'haar');
    [Ga(:,:,k),Gh(:,:,k),Gv(:,:,k),Gd(:,:,k)]=dwt2(imageArray(:,:,2,k),'haar');
    [Ba(:,:,k),Bh(:,:,k),Bv(:,:,k),Bd(:,:,k)]=dwt2(imageArray(:,:,3,k),'haar');
end
```

Figure 4.67: Single-level discrete 2-D wavelet transform Matlab

In Figure [4.67], `k` is the Z position or depth an image was captured at, `N` is the number of different Z positions existing in the dataset, `imageArray(:,:,1,k)` returns a 2D single channel image (`1` for Red, `2` for Green, `3` for Blue) captured at depth `k`.

Figure [4.68] presents the first RGB image of our input dataset.

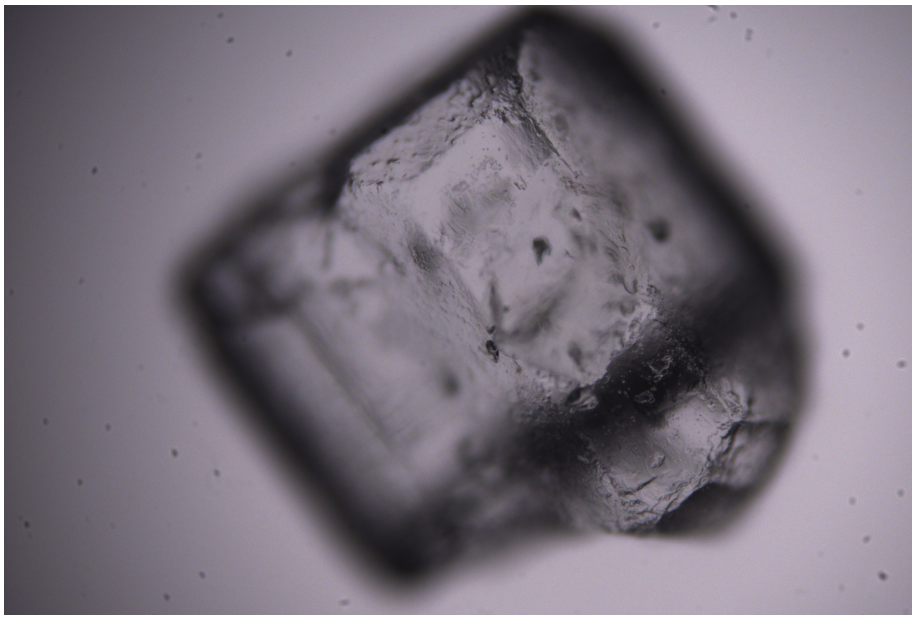

Figure 4.68: DWT First Input Image

Figure [4.69] presents the results of the Single-level discrete 2-D wavelet transform for first RGB image of our input dataset , as shown in Figure [4.68].

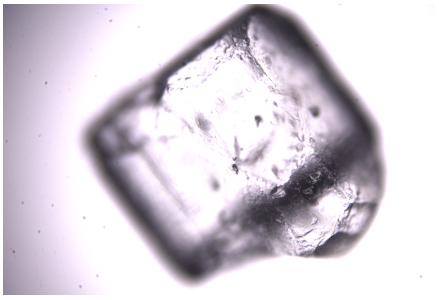

(a) Amplitude Coefficient (Low)

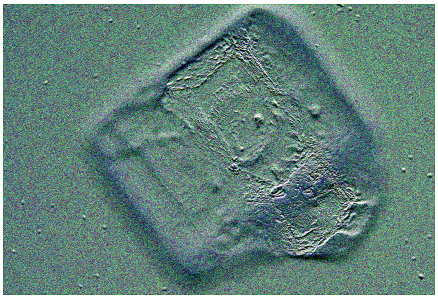

(b) Horizontal Coefficient (High)

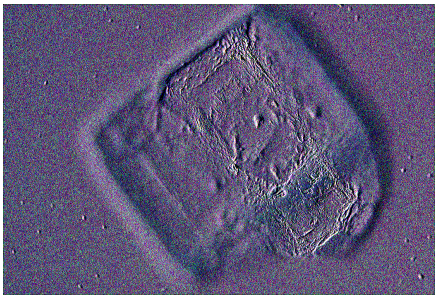

(c) Vertical Coefficient (High)

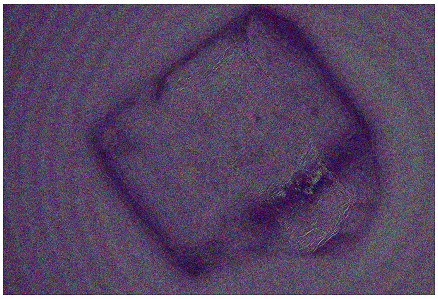

(d) Diagonal Coefficient (High)

Figure 4.69: DWT Coefficients

4.4.3 Low Frequency Coefficients Fusion

The low frequency sub-band presents a blurry version of the original image, where most information is kept at. To select the coefficients in low frequency sub-bands, a sharpness focus measure is implemented. The sharpness measure is a Tenengrad function based on Sobel operator, which also considered the neighborhood information of a pixel by a fixed window. This measure can be used to indicate the clarity of the image pixels, and a well-focused image is expected to have sharper information [37]. The sharpness focus measure is shown in Equation [4.4.3.1].

$$G(k,l) = \sqrt{(X(k,l) * J)^2 + (X(k,l) * K)^2} \tag{4.4.3.1}$$

where X(k,l) is the input coefficient array with size (i,j), G(k,l) is the output sharpness array with size (i,j), J $= \begin{bmatrix} -1 & -2 & -1 \\ 0 & 0 & 0 \\ 1 & 2 & 1 \end{bmatrix}$ and K $= \begin{bmatrix} 1 & 0 & -1 \\ 2 & 0 & -2 \\ 1 & 0 & -1 \end{bmatrix}$.

Figure [4.70] presents the sharpness measurement designed in Matlab.

```
function OUT = LowFreq(X)
    J = [ -1 -2 -1;
           0  0  0;
           1  2  1];

    K = [1 0 -1;
         2 0 -2;
         1 0 -1];

    N = size(X,4);
    [k1,k2]=size(X(:,:,1,1));

 for l=1:N
       for k=1 : 3
           for i=1 : k1
               for j=1 : k2
                   if (i==1) t1 = 0;
                   else t1 = 1;
                   end
                   if (j==1) t3 = 0;
                   else t3 = 1;
                   end
                   if (i==k1) t2 = 0;
                   else t2 = 1;
                   end
                   if (j==k2) t4 = 0;
                   else t4 = 1;
                   end
                   G(i,j,k,l) = sqrt(sum(sum(X(i-t1:i+t2,j-t3:j+t4,k,l).*J(2-t1:2+t2, 2-t3:2+t4))).^2 +
                                     sum(sum(X(i-t1:i+t2,j-t3:j+t4,k,l).*K(2-t1:2+t2, 2-t3:2+t4))).^2);
               end
           end
       end
    end
```

Figure 4.70: Sharpness Focus Metric Matlab

After obtaining the sharpness of all pixels of the low frequency sub-bands, a maximum scheme of it is then performed. Because, for multi-focus image fusion, the focused pixels should produce maximum sharpness measure, yet the defocused pixels should produce minimum sharpness measure on the contrary [37]. The *Maximum Sharpness* fusion scheme of the coefficients in low frequency sub-band is shown in Equation [4.4.3.2].

$$OUT(i,j,k) = X(i,j,k,maxL) \tag{4.4.3.2}$$

where X is the input image array, OUT is the fused coefficient, maxL is the Z position where G(i,j,k,l) maximizes for given i, j and k.

Figure [4.71] presents the maximum sharpness measurement designed in Matlab.

```
for i=1:k1
    for j=1:k2
        for l=1:N
            if (l == 1)
                maxi = l;
            else
                if(G(i,j,1,l)+G(i,j,2,l)+G(i,j,3,l) >= G(i,j,1,maxi)+G(i,j,2,maxi)+G(i,j,3,maxi))
                    maxi = l;
                end
            end
        end
        OUT(i,j,1) = X(i,j,1,maxi);
        OUT(i,j,2) = X(i,j,2,maxi);
        OUT(i,j,3) = X(i,j,3,maxi);
    end
end
```

Figure 4.71: DWT Low Frequency Max Sharpness Scheme Matlab

Figures [4.72,4.73] presents the fusion of the input Amplitude Coefficients with max Sharpness scheme.

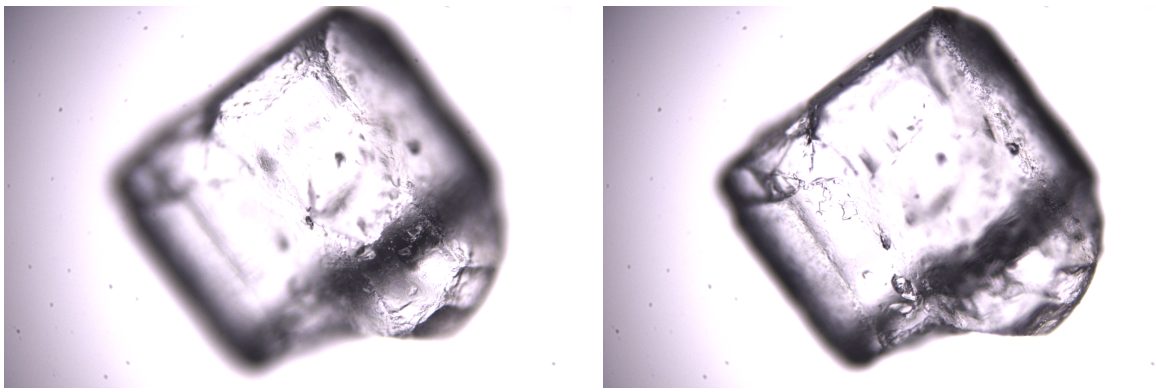

Figure 4.72: DWT Amplitude Coefficient of (a) the first input image (Low) (b) the second input image.

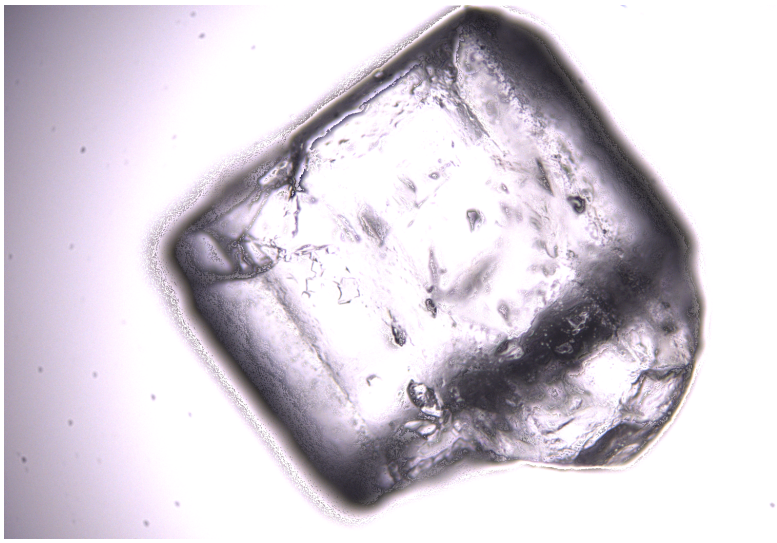

Figure 4.73: DWT Low Frequency Coefficients Fusion

4.4.4 High Frequency Coefficients Fusion

The high frequency sub-bands contain the detail coefficients of an image, which usually have large absolute values correspond to sharp intensity changes and preserve salient information in the image. So, if the rule mentioned above for low frequency sub-bands is adopted here, the fused results will be blocked. Besides, according to the wavelet transform theory, we know that the energy of the high frequency coefficients of a clear image is much larger than that of a blurred one. Based on this analysis and considering that the wavelet coefficient is related to its neighboring region, we propose a fusion scheme by computing the neighboring energy maximum to select the high frequency coefficients [37]. The neighboring energy feature is shown in Equation [4.4.4.1].

$$NE(k,l) = X(k,l)^2 * H \tag{4.4.4.1}$$

where X(k,l) is the input coefficient array with size (i,j), NE(k,l) is the output sharpness array with size (i,j) and H $= \begin{bmatrix} 0 & 1/8 & 0 \\ 1/8 & 1/2 & 1/8 \\ 0 & 1/8 & 0 \end{bmatrix}$.

Figure [4.74] presents the neighboring energy measurement designed in Matlab.

```
function OUT = HighFreq(X)
    H = [ 0 1/8 0 ;
        1/8 1/2 1/8;
        0 1/8 0];

    N = size(X,4);
    [k1,k2]=size(X(:,:,1,1));

    for l=1 : N
        for k=1 : 3
            for i=1 : k1
                for j=1 : k2
                    if (i==1) t1 = 0;
                    else t1 = 1;
                    end
                    if (j==1) t3 = 0;
                    else t3 = 1;
                    end
                    if (i==k1) t2 = 0;
                    else t2 = 1;
                    end
                    if (j==k2) t4 = 0;
                    else t4 = 1;
                    end
                    NE(i,j,k,l) = sum(sum(X(i-t1:i+t2,j-t3:j+t4,k,l).*H(2-t1:2+t2, 2-t3:2+t4)));
                end
            end

        end
    end
```

Figure 4.74: DWT High Frequency Neighboring Energy Scheme Matlab

Then we perform a maximum selection rule on the coefficients in high frequency sub-bands, which select the coefficients with higher energy into the fused image. The neighboring *Maximum Energy* fusion scheme of the coefficients in high frequency sub-bands is shown in Equation [4.4.4.2].

$$OUT(i,j,k) = X(i,j,k,maxL) \tag{4.4.4.2}$$

where X is the input image array, OUT is the fused coefficient, maxL is the Z position where NE(i,j,k,l) maximizes for given i, j and k.

Figure [4.75] presents the maximum sharpness measurement designed in Matlab.

```
for i=1:k1
    for j=1:k2
        for l=1 : N
            if(l==1)
                maxi = l;
            else
                if(NE(i,j,1,l)+NE(i,j,2,l)+NE(i,j,3,l)>NE(i,j,1,maxi)+NE(i,j,2,maxi)+NE(i,j,3,maxi))
                    maxi = l;
                end
            end
        end
        OUT(i,j,1) = X(i,j,1,maxi);
        OUT(i,j,2) = X(i,j,2,maxi);
        OUT(i,j,3) = X(i,j,3,maxi);
    end
end
```

Figure 4.75: DWT Low Frequency Max Neighbouring Energy Scheme Matlab

Figures [4.76,4.77] presents the results of the Single-level discrete 2-D wavelet transform.

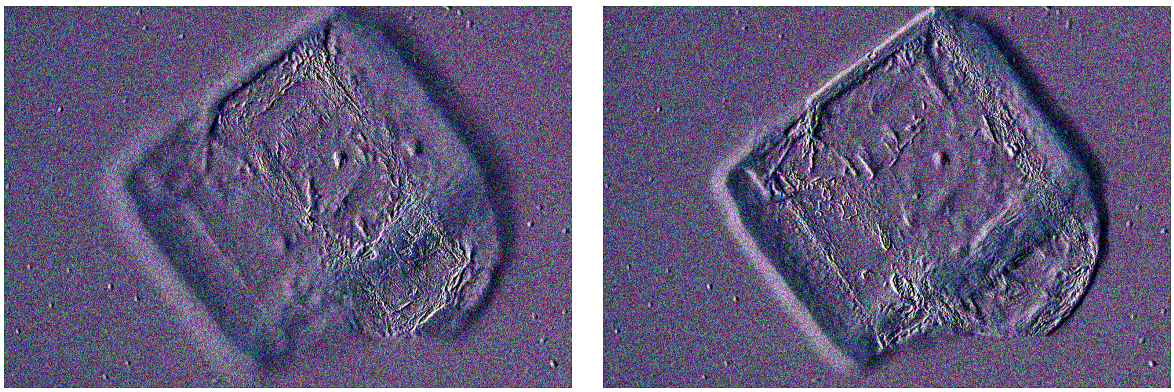

Figure 4.76: DWT Vertical Coefficients of (a) the first input image (Low) (b) the second input image.

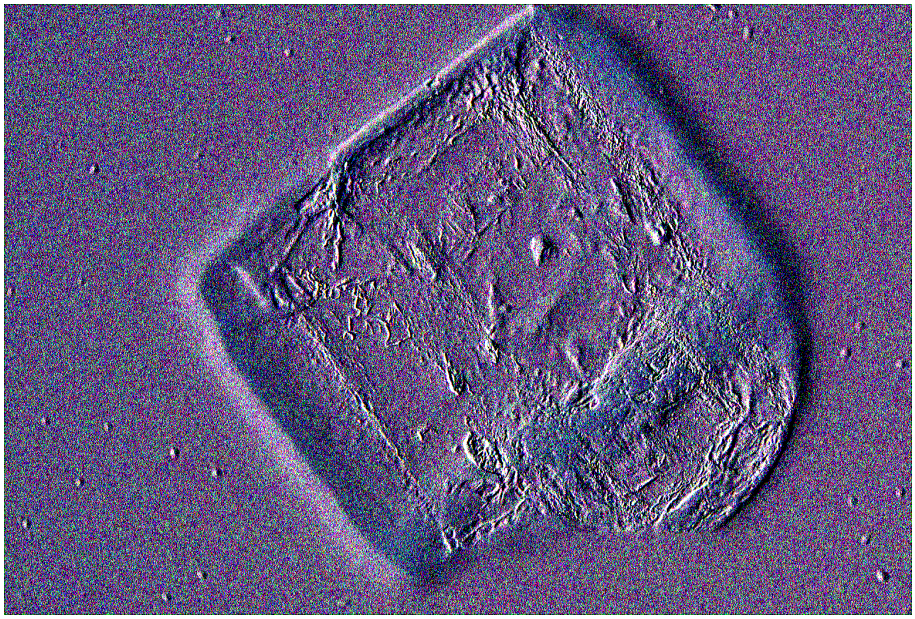

Figure 4.77: DWT High Frequency Coefficients Fusion

4.4.5 Verification

The selection of the coefficients for the image fusion was held with the help of the maximum selection schemes for both low and high frequency bands. These maximum selection schemes will produce sharper coefficients but heavily dependant to noise. Moreover, we processed the different coefficients separately, so in theory there will be a lack of homogeneity in the fused image.

This verification process is essential for improving the method's Signal to Noise Ratio (SNR) which is heavily dependant to noise and the non-homogeneity of the coefficients. This verification procedure, based on a majority filter, ensures that the dominant features of each input image, are incorporated as clearly as possible to the fused image. The verification process is based on a window-based verification (WBV), its rule is that if the center coefficient comes from image X, but the majority of the surrounding coefficients in the window come from image Y, then the center sample is changed to come from Y, and vice versa. This rule is applied to a binary decision map, and then it is followed by the application of a majority filter. The fused coefficients are finally obtained by the new binary decision map [37]. The window used in this implementation is 3 by 3 or dynamically allocated (reduced) in the borders of the image. This process can be formulated as follows.

Firstly, we compute, for each pixel, the fused coefficient's maximum value of the 3 by 3 window.

$$temp(k) = \sum_{i,j} max(|Y(i-t1:i+t2, j-t3:j+t4, k)|); \tag{4.4.5.1}$$

where, Y(i,j,k) is the input RGB coefficient, t1, t2, t3 and t4 are the dynamically allocated window bounds and temp is temporary variable holding the maximum value of the analyzed region.

Then, for each window we compute the absolute difference between the fused coefficient and the individual coefficients derived by the DWT Equation [].

$$pi(i,j,k,l) = |temp(k) - \sum_{i,j} max(|X(i-t1:i+t2, j-t3:j+t4, k, l)|)|; \tag{4.4.5.2}$$

where, X(i,j,k,l) is the input RGB coefficient, t1, t2, t3 and t4 are the dynamically allocated window bounds and pi(i,j,k,l) is the absolute difference between each coefficient and the fused coefficient.

Figure [4.81] presents the coefficients absolute difference calculation designed in Matlab.

```
function OUT = verified2(X,Y,name)
    N = size(X,4);
    [k1,k2]=size(X(:,:,1,1));

    for k=1 : 3
        for i=1 : k1
            for j=1 : k2
                if (i==1) t1 = 0;
                else t1 = 1;
                end
                if (j==1) t3 = 0;
                else t3 = 1;
                end
                if (i==k1) t2 = 0;
                else t2 = 1;
                end
                if (j==k2) t4 = 0;
                else t4 = 1;
                end
                temp = sum(sum(max(abs(Y(i-t1:i+t2,j-t3:j+t4,k)))));
                for l=1 : N
                    pi(i,j,k,l) = abs(temp - sum(sum(max(abs(X(i-t1:i+t2,j-t3:j+t4,k,l)))))));
                end
            end
        end
    end
```

Figure 4.78: DWT Coefficient Fusion Verification Matlab

The selection of the coefficient that contributes the most to the fused coefficient, is done by creating a binary mask based on their minimum differences form the fused coefficient, computed earlier. As

shown in Equations [4.4.5.3], each coefficient's mask will have a pixel highlighted (1) if it has the minimum difference from the fused coefficient pixel, or else not (0).

$$q(i,j,l) = \left\{ \begin{array}{ll} 1, & \sum_k pi(i,j,l) \leq \sum_k pi(i,j,mini) \\ 0, & else \end{array} \right\} \tag{4.4.5.3}$$

where, q(i,j,k,l) corresponds to binary information for each individual coefficient describing its contribution to the fused coefficient.

Figure [4.79] presents the selection of the minimum difference coefficients for each pixel designed in Matlab.

```
for i=1 : k1
    for j=1 : k2
        for l=1 : N
            q(i,j,1:3,l) = 0;
            if (l == 1)
                mini = l;
            else
                if(sum(pi(i,j,1:3,l)) <= sum(pi(i,j,1:3,mini)))
                    mini = l;
                end
            end
        end
       q(i,j,1:3,mini) = 1;
    end
end
```

Figure 4.79: DWT Coefficient Fusion Verification Binary Mask Matlab

Next, we redesign the individual coefficients binary masks in order to obtain better homogeneity. To achieve this, we are going to filter each coefficient's pixel used in the fused coefficient based on a neighbouring scheme, meaning that fused coefficients are selected based on which individual contributes the most in a neighbouring region, as shown in Equation [4.4.5.4].

$$q1(i,j,l) = \left\{ \begin{array}{ll} 1, & \sum_{m,n} q(m,n,1,l) \geq \sum_{m,n} q(m,n,1,maxi) \\ 0, & else \end{array} \right\} \tag{4.4.5.4}$$

where, m and n describes the window (neighbour) around each i,j and q1(i,j,k,l) corresponds to binary information for each individual coefficient describing its contribution to the fused coefficient.

Figure [4.81] presents the coefficients absolute difference calculation designed in Matlab.

```
for i=1 : k1
    for j=1 : k2
        if (i==1) t1 = 0;
        else t1 = 1;
        end
        if (j==1) t3 = 0;
        else t3 = 1;
        end
        if (i==k1) t2 = 0;
        else t2 = 1;
        end
        if (j==k2) t4 = 0;
        else t4 = 1;
        end
        maxi = 1;
        for l=1 : N
            q1(i,j,1:3,l) = 0;
            if(sum(sum(q(i-t1:i+t2,j-t3:j+t4,1,l)))>=sum(sum(q(i-t1:i+t2,j-t3:j+t4,1,maxi))))
            maxi = l;
            end
        end
        q1(i,j,1:3,maxi) = 1;
    end
end
```

Figure 4.80: DWT Coefficient Fusion Verification Matlab

Finally, we use the binary masks to select which of the input coefficients pixels will contribute to fused coefficient output. The selection of the fused image and vector designed in Matlab, as presented in Figure [4.81].

```
for i=1 : k1
    for j=1 : k2
        for l=1 : N
            OUT(i,j,1:3,l) = 0;
        if (q1(i,j,1,l) == 1)
            OUT(i,j,1:3,N+1) = q1(i,j,1:3,l) .* X(i,j,1:3,l);
            OUT(i,j,1:3,l) = q1(i,j,1:3,l) .* X(i,j,1:3,l);
        end
    end

    end
end
```

Figure 4.81: DWT Coefficient Fusion Verification Matlab

Figures [4.82, 4.83] presents the results of the verification of each of the individual coefficients as perceived through the final fused output.

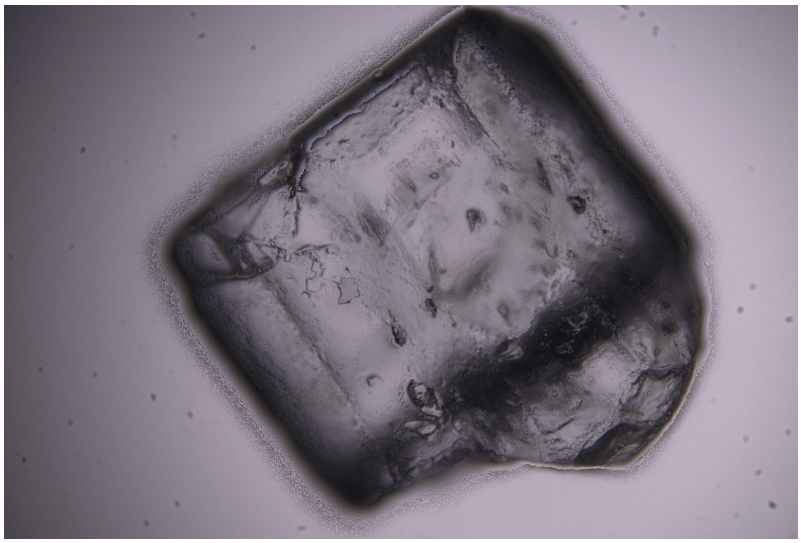

Figure 4.82: DWT Fusion Output.

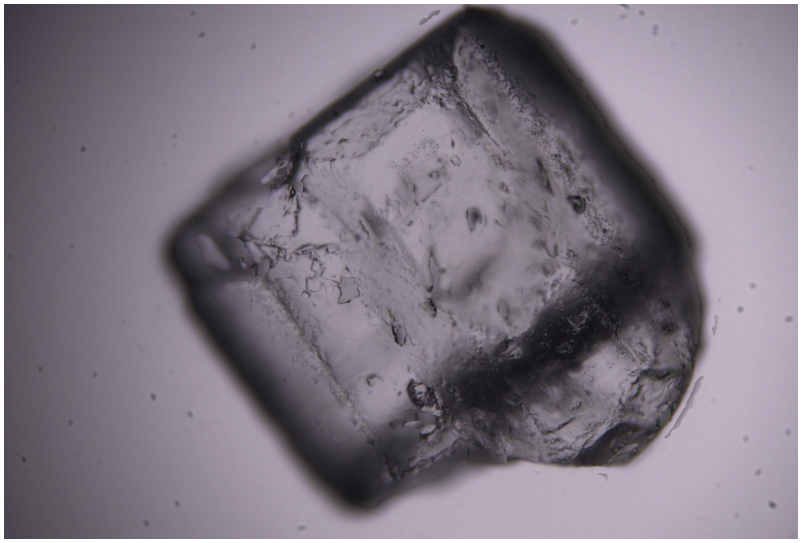

Figure 4.83: DWT Fusion Verified Output.

4.4.6 Inverse DWT

Compose an image using its spectral features or *Low* and *High* frequency components, using the iDWT. This procedure, was held using the Single-level inverse discrete 2-D wavelet transform function Matlab provides thought Wavelet Toolbox [6]. This function performs a single-level two-dimensional wavelet reconstruction based on the approximation matrix cA and details matrices cH, cV, and cD (horizontal, vertical, and diagonal, respectively) using the wavelet specified by wname [6]. The 'wname' string contains the wavelet name. The syntax of this function is shown in Equation [4.4.6.1].

$$x = idwt2(cA, cH, cV, cD, wname) \tag{4.4.6.1}$$

The following Figure [4.84] describes the basic decomposition steps the Single-level inverse discrete 2-D wavelet transform algorithm executes:

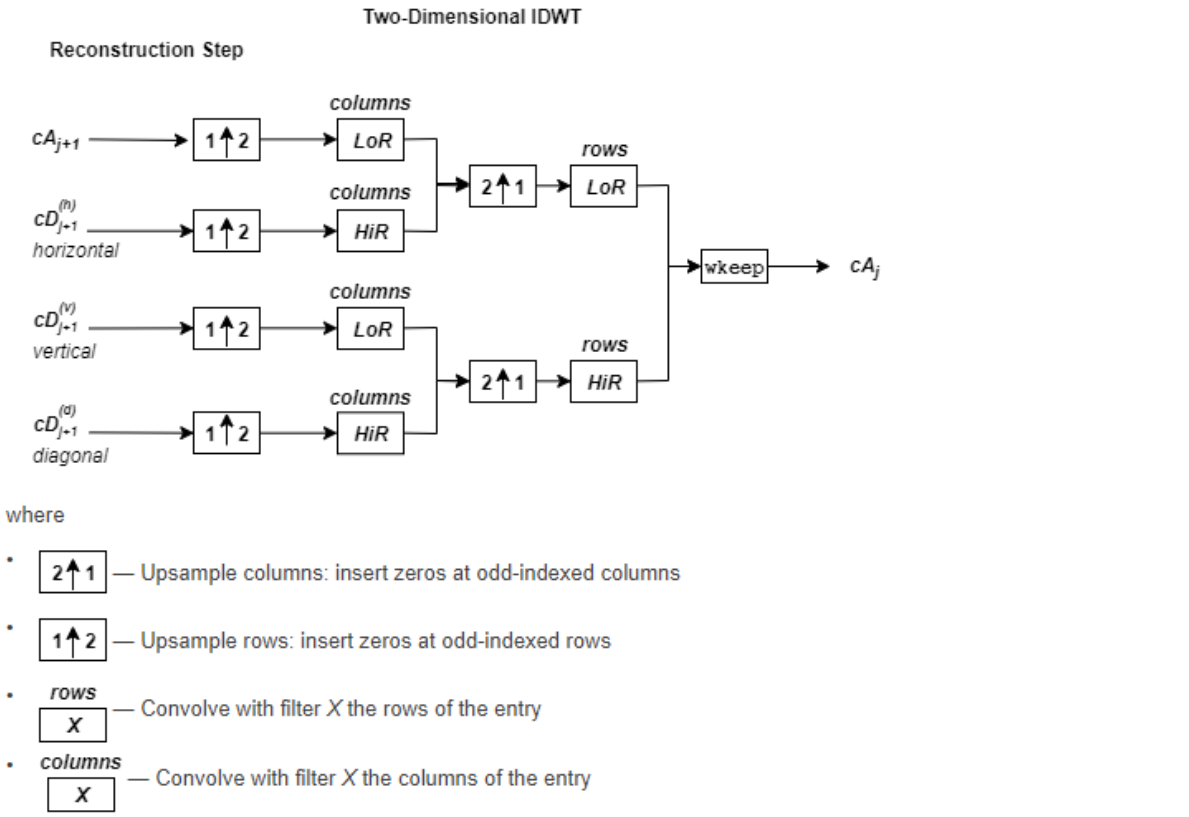

Figure 4.84: Single-level inverse discrete 2-D wavelet transform Algorithm
Source: Wavelet Toolbox [6]

Figure [4.85] presents the Matlab implementation of iDWT, using as inputs the fused coefficients produced from the previously refereed schemes, resulting to the fused output image (`Newimage`).

```
Newimage(:,:,1)=idwt2(A(:,:,1),H(:,:,1),V(:,:,1),D(:,:,1),'haar');
Newimage(:,:,2)=idwt2(A(:,:,2),H(:,:,2),V(:,:,2),D(:,:,2),'haar');
Newimage(:,:,3)=idwt2(A(:,:,3),H(:,:,3),V(:,:,3),D(:,:,3),'haar');
```

Figure 4.85: Single-level inverse discrete 2-D wavelet transform Matlab

In Figure [4.85], `A` represents the Low Frequency sub-band or Amplitude Coefficient, for the High Frequency sub-bands `H` represents the Horizontal Coefficient, `V` represents the Vertical Coefficient, `D` represents the Diagonal Coefficient and `Newimage(:,:,1)` returns a 2D single channel image (`1` for Red, `2` for Green, `3` for Blue).

Merging the resulting values to produce a meaningful RGB Image. Foe the merging algorithm we implemented a simple weighted merge, the mathematical representation of which is shown in Equation [4.4.6.2].

$$image(k) = Newimage(k) \cdot 0.004 \tag{4.4.6.2}$$

where k refers to an individual red or green or blue channel, Newimage(k) is the input coefficient array with size (i,j), image(k) is the output sharpness array with size (i,j).

```
RGBimage = cat(3,Newimage(:,:,1)*0.004,Newimage(:,:,2)*0.004,Newimage(:,:,3)*0.004);
```

Figure 4.86: Weighted Image Merge Matlab

Figure [4.86] presents the Matlab implementation of weighted image merging, using as inputs the fused monochrome channels produced from the previously refereed iDWT, resulting to the fused output RGB image (`RGBimage`).

Figures [4.97, 4.98] presents the results of the proposed Multi Focus Image Fusion technique.

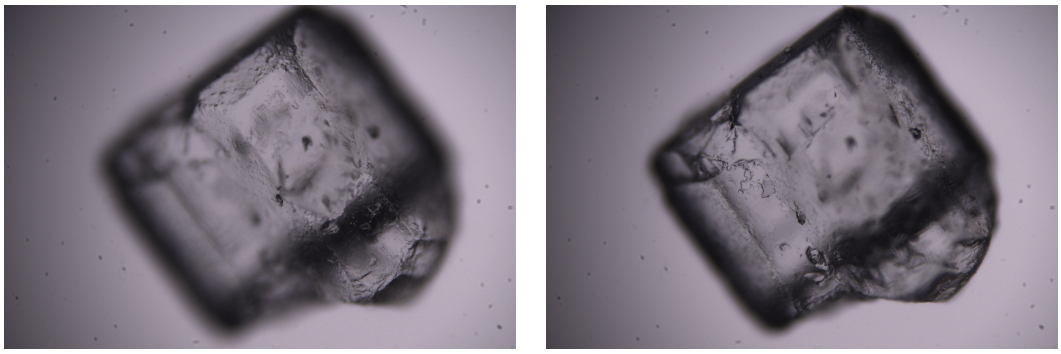

Figure 4.87: Multi Focus Image Fusion - Input Images

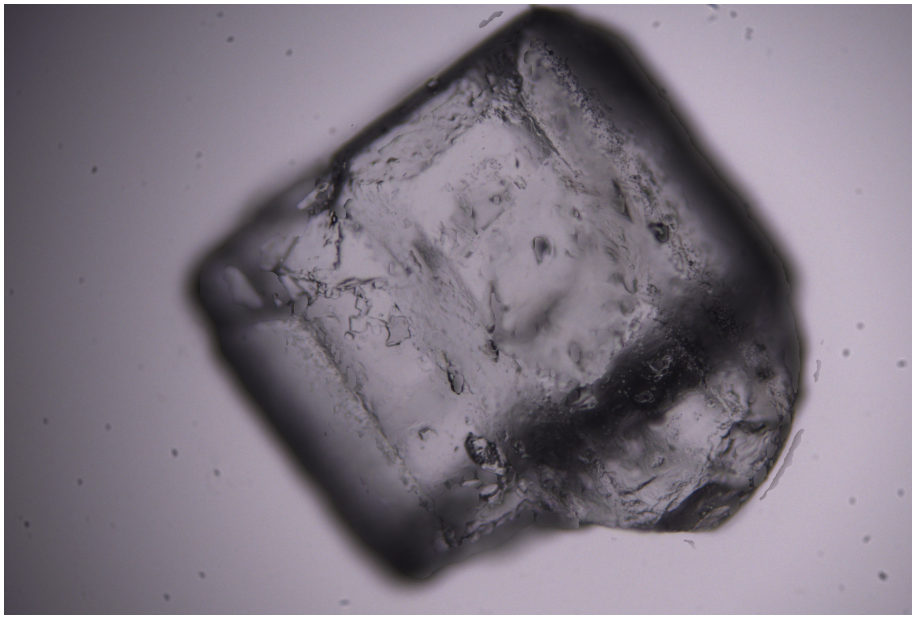

Figure 4.88: Multi Focus Image Fusion - Verified Fused RGB Image

4.4.7 Out of focus extraction

As presented, the most important part of a Multi-Focus Image Fusion algorithm is identifying the useful information - inside each partly focused image - and fusing this information together along the Z-Stack. *Window-based* fusion functions have exhibited better performance than *pixel-based*.

Using this *Window-based* verification process, we can now create separate binary decision maps for each input image. By applying each of these maps to its respective input image, we can filter all of their non-sharp content. In other words, using this method we implement Out of Focus Extraction of the input images. The drawback of this approach is that in order to extract the out of focus of an image, it is mandatory to analyze a big z-stack (dataset).

Figures [4.89, 4.90] presents the results of the proposed Out of Focus extraction technique.

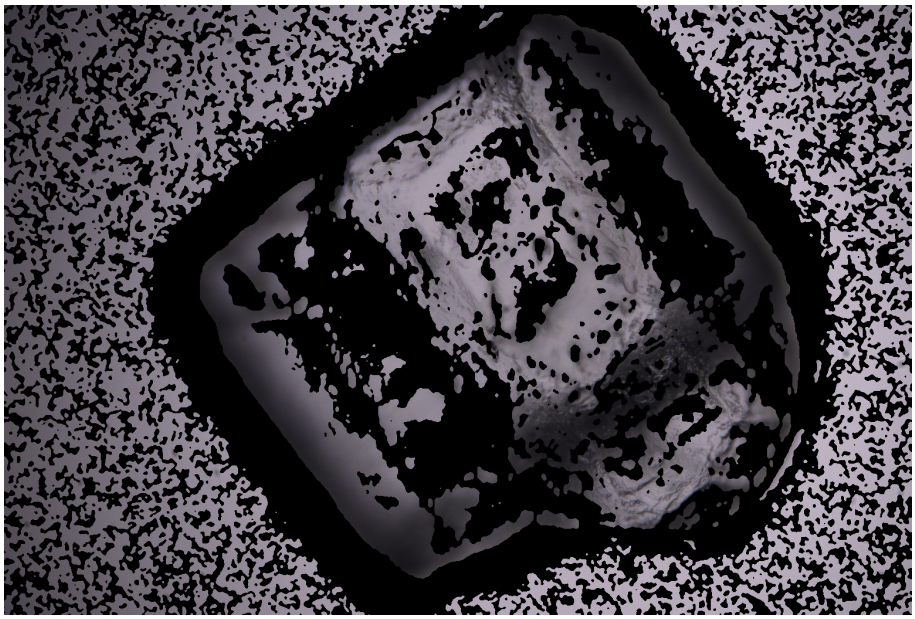

Figure 4.89: Out of Focus Extraction - Verified Image 1

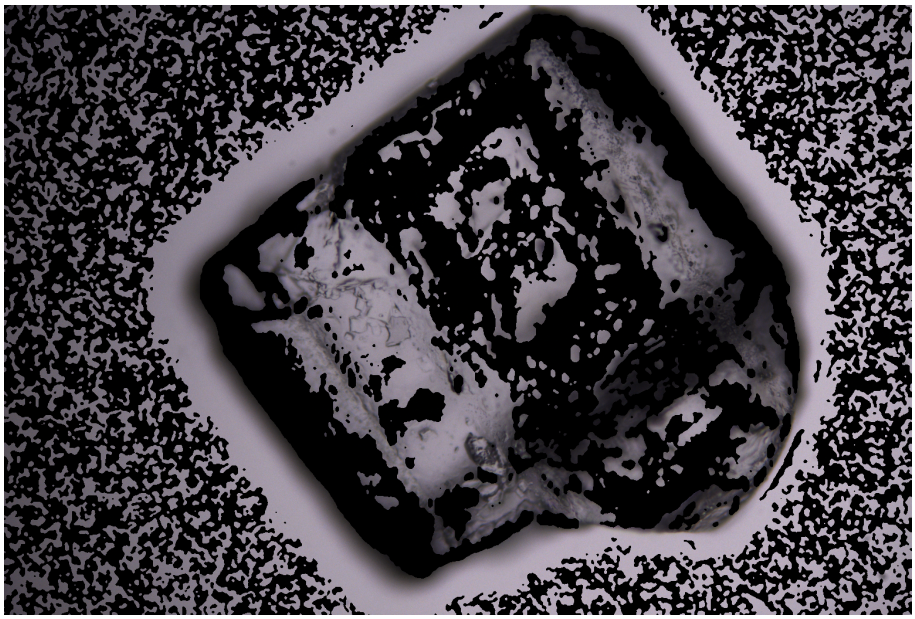

Figure 4.90: Out of Focus Extraction - Verified Image 2

4.5 System's Configuration & Setup

While implementing the Motor Driver and the Focusing sections of this research, the basic setup and integration to the main software of the system was achieved with the precious help and guidance of the researchers from the Electronics Laboratory in Technical University of Crete and the Spectricon's engineers.

The first stage of integration was focused on implementing a test case with all the peripherals connected and basic functionality in terms of motion enhancements. The hardware of the microscope was installed and peripherals communication, motors operation and navigation processes were constructed. The microscope is shown in Figure [4.93].

In next stage, the microscope's automated acquisitions began to emerge. The Auto Focus algorithms and the Absolute Metric for Focus Quality was tested and evaluated. An Area Scanning procedure was implemented in order to acquire consecutive adjacent images and potentially stitch them the together, with the help of a fellow researcher's algorithm.

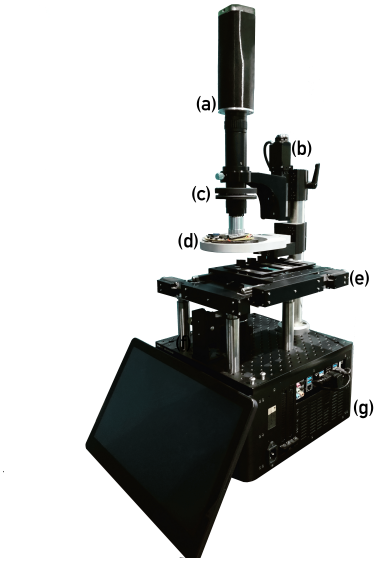

Figure 4.91: Lumnia Updated Hardware

Figure [4.93], presents the final setup of our microscope. This microscope utilizes (a) Multimodal Camera, (b) Z motor for Focus Control, (c) Variable Magnification and Encoder, (d) Epi Illuminations Controllable Light Source, (e) X Y Stage for Spatial Control, (g) enclosed high performance computer, Three Axes Motor Driver and Transmission Controllable Light Sources.

Finally, the Graphical User Interface (GUI) of the system was constructed by Spectricon's engineers and is shown in Figure [4.92].

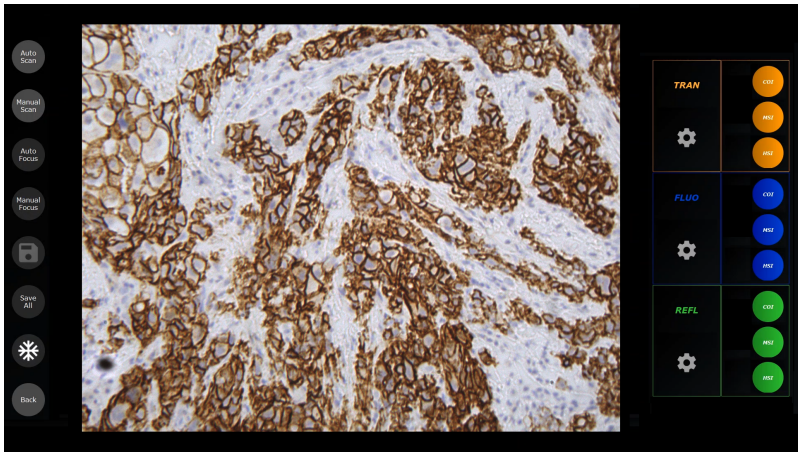

Figure 4.92: Lumnia Software GUI

In Figure [4.92], the modality selection bar is presented in the right part of the GUI and operation selection bar is presented on the left part. Manual Scan button refers to the joystick operation of the motor units, whereas the Auto Scan button refers to automatic area scanning and potentially stitching acquisition. The Manual Focus button enables the Z axis control through joystick, whereas Auto Focus button enables the system automatic focusing capabilities. In the right part, through modality selection bar the system enables the fast use of the illumination control system and preview mode selection. Finally, in the center of the GUI, the live preview of the specimen under examination is presented.

4.6 Technical Validation

Overall, this research gave us the opportunity to work in an real biomedical research environment, with the precious help of specialized engineers and real use cases scenarios using state of the art machinery. The results this thesis contents, were produced, discussed and evaluated in this environment, achieving an overall high efficiency.

The design architecture of our Motor Driver and the resulting hardware setup is presented in Figure [4.93].

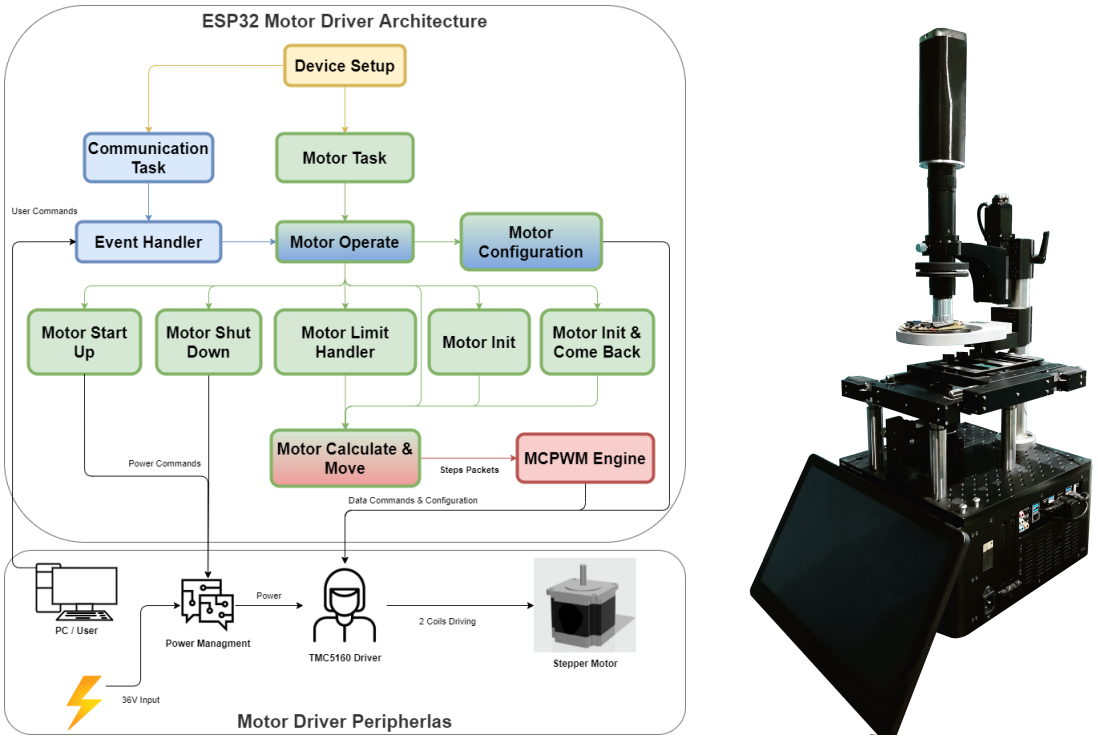

Figure 4.93: Lumnia Updated Hardware

We achieved creating a system that can easily setup and drive a huge variety of stepper motors due to its generic design and its dynamic usability. Using this generic Motor Driver provides us the ability to control and overextend the capabilities of a stepper motor, in terms of speed and movement stability. With the help of the Acceleration and Deceleration Slope tuning mechanism, this driver can be tuned to overdrive stepper motors to accelerate rapidly from zero speed, without any loss of steps, to maximum speeds exceeding the motors specified capabilities. This process was achieved by correlating the acceleration/deceleration curves (torque) with the load's inertia. Moreover, this driver can control and manipulate linear Motorized Translation Stages with the help of its position decision making system. This can be extremely useful in applications where high level control of a motor demands the use of absolute positioning with great accuracy in real time.

The results of our Auto Focus algorithms evaluation process are presented in Figure [4.94].

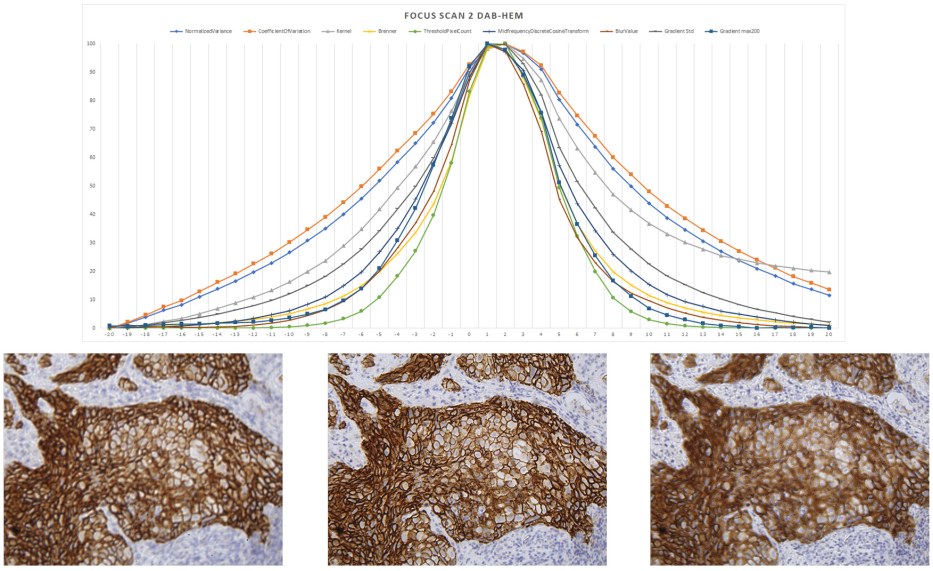

Figure 4.94: Focus Scan of DAB Hematoxylin Specimen

The result curves of Figure [4.94] are normalized for presentation proposes. We concluded that the results of different algorithms are always related to the content characteristics of the imaging region and may also vary even in the same focal region. This is normal because every one produces accurate results under certain circumstances (noise, background, illu-mination etc.). In order to create an accurate, robust and time efficient auto focus system, we implemented the proposed algorithms and used the best of them or a combination of them, in different occasions. Finally, we observed that all these algorithms produce relative measurements of focus (focal estimations), which means that the only comparable(between specimens and focal regions) measurement they can produce, is based on the derivative of their output curve. For this reason, a time consuming focus scan is mandatory for these relative measurements to produce arithmetically absolute focusing results.

The Absolute Metric for Focus Quality results and evaluation process are presented in Figure [4.95].

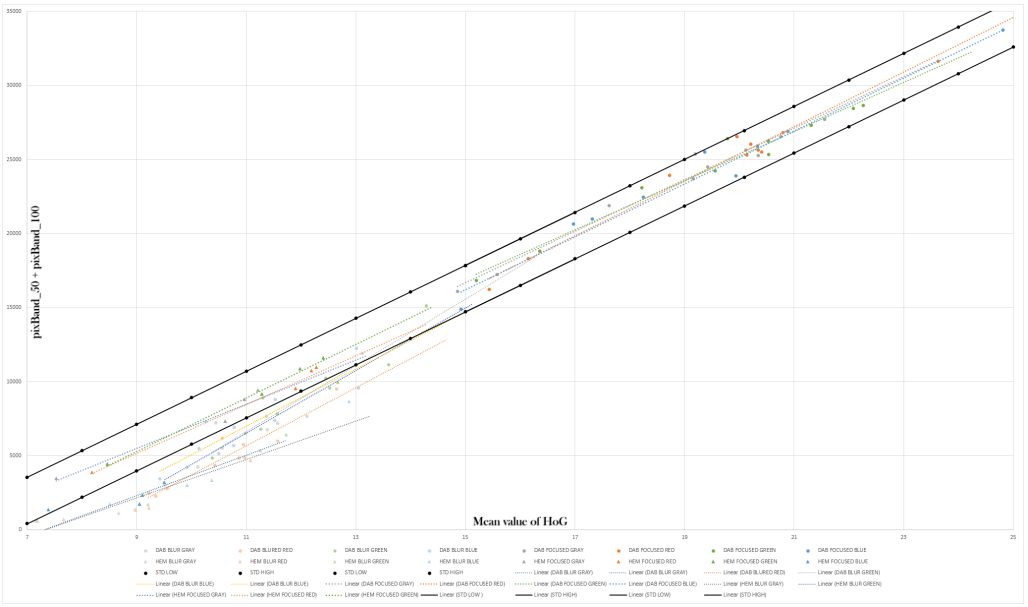

Figure 4.95: Gradient Based Absolute Metric Thresholded Graph

Thresholds, based on a big data-set of Focused and Defocused images, are applied to the graph to bound a special area. Every single point inside this area can be considered a focused image and every one that it is outside of the bounded area, can be considered blurred image. This thresholding method is proven to be a reliable and robust absolute focus criterion so far. The resulting mechanism achieved to bound the axes of this graph with a ratio that can describe, with absolute values, how focused an image is, based on the deviation of each dataset from the thresholds, as presented in Figure [4.96] shown below, where images produced from Focus Scan are classified from our metric as *Focused* or *Blurred*.

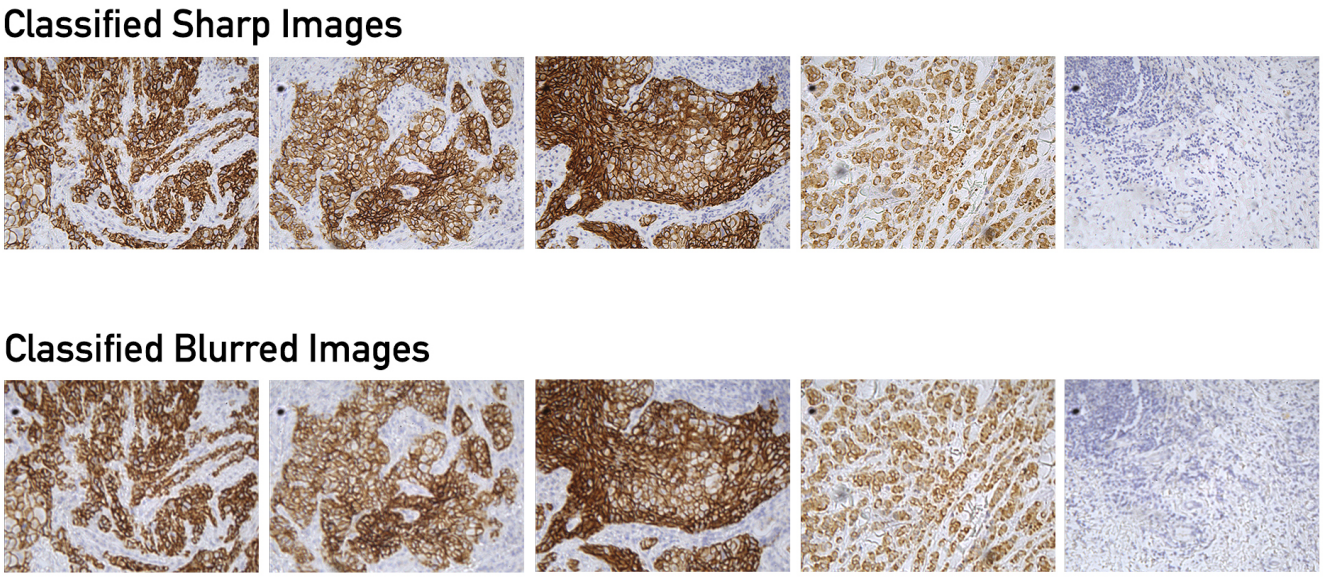

Figure 4.96: Gradient Based Absolute Metric Image Classification

The outcomes shown in Figures [4.64, 4.65], are based on our experimental global thresholing. In conclusion, this Gradient Based approach produces an easy to implement toolkit that can lead to topographical and focal measurement or even segmentation and due to its computational simplicity it can be implemented in GPU and therefore, achieve an overall real time experience.

The results our Multi Focus Image Fusion technique for RGB z-stack structures, are presented in Figures [4.97, 4.98].

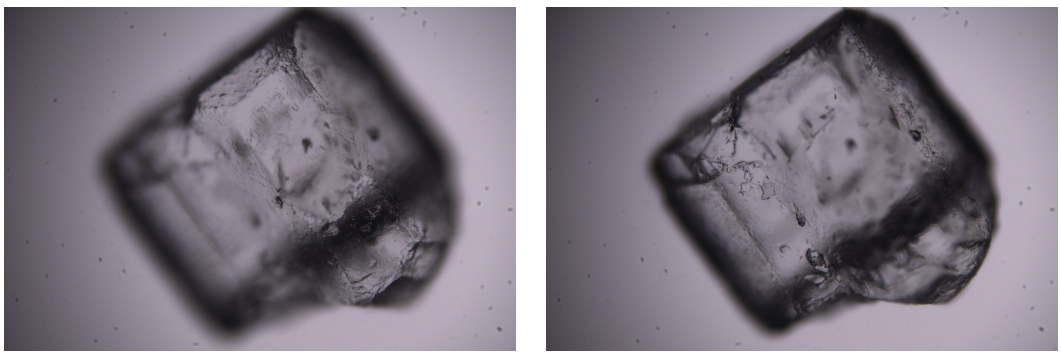

Figure 4.97: Multi Focus Image Fusion - Input Images

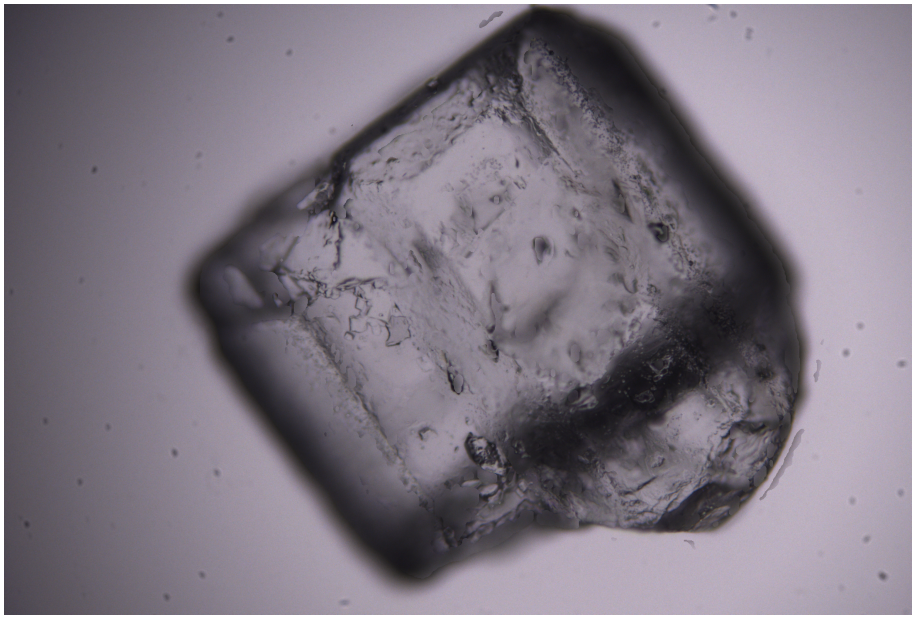

Figure 4.98: Multi Focus Image Fusion - Verified Fused RGB Image

Through this *Window-based* verification process, we can now create separate binary decision maps for each input image. By applying each of these maps to its respective input image, we can filter all of their non-sharp content. In other words, using this method we implement Out of Focus Extraction of the input images. The drawback of this approach is that in order to extract the out of focus of an image, it is mandatory to analyze a big z-stack (dataset).

Figure [4.99] presents the results of the proposed Out of Focus extraction technique.

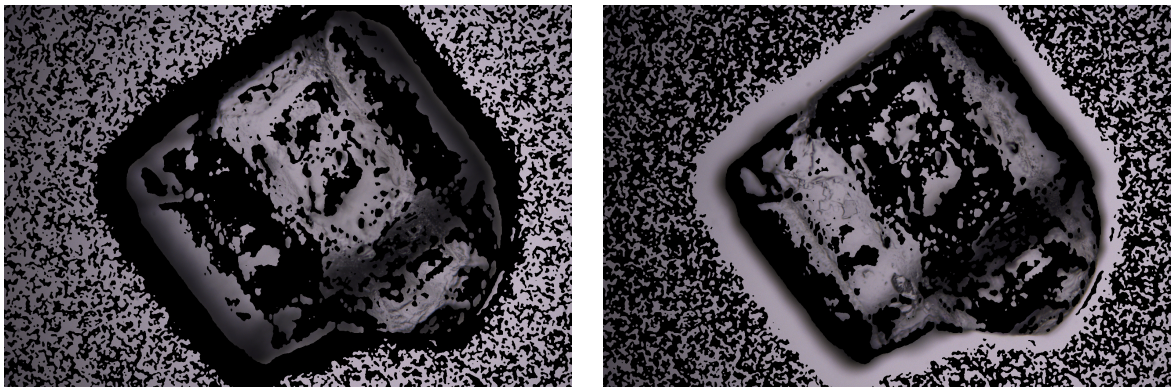

Figure 4.99: Out of Focus Extraction - Verified Images

4.7 Clinical Validation

Clinical validation of the system's imaging capabilities was conducted in real case scenarios, with the help of the researchers from the Electronics Laboratory in Technical University of Crete and the Spectricon's engineers. The system is designed to work as Widefield Microscope with the updown configuration and utilizes the Brightfield, Darkfield and Epi-fluorescence modalities. The images produced from the examination of pathological specimens, fibers with different magnifications are presented in Figures [4.100, 4.101, 4.103].

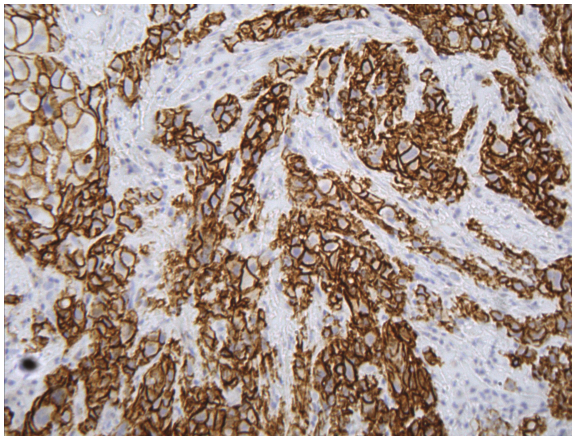

Figure 4.100: Pathology Brightfield - Stained Tissue

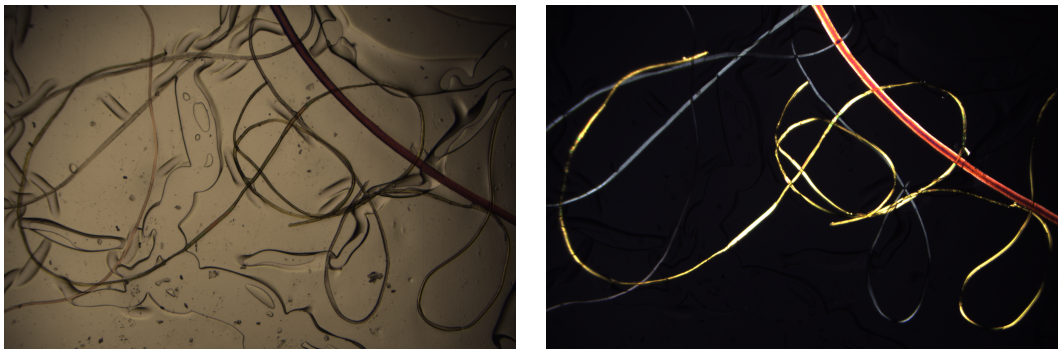

Figure 4.101: Fibers Brightfield (left), Multi Epi-Fluorescence (right)

This microscope also offers more advanced features for Spectral Acquisition, Selective Excitation/Emission (Ex/Em) Overlay Maps and Intensity Maps that produce specialized data structures for research and diagnosis, as shown in Figure [4.102].

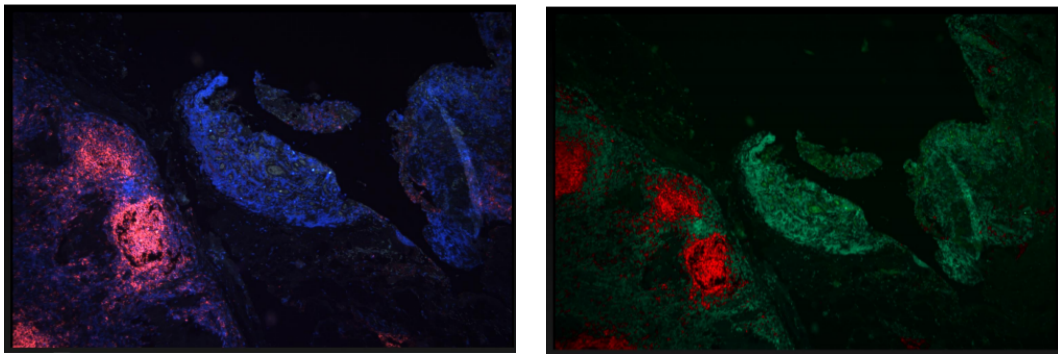

Figure 4.102: Lumnia-FL Imaging Advanced Modalities Multi Epi-Fluorescence (left), Selective Ex/Em Overlay Map (Emission: Green[510-575] + Red[640-...]) (right)

The imaging capabilities of this system, compared with some of the most accurate Confocal microscope images, provided by a research group from the Foundation for Research and Technologie Hellas (FORTH) in Heraklion, are presented in Figure [4.103].

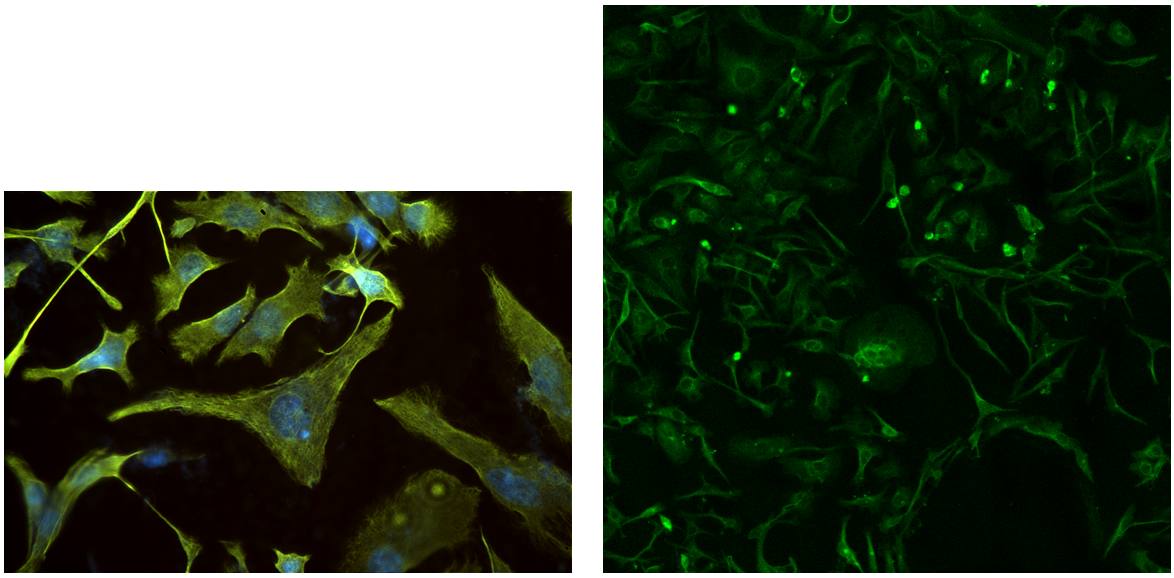

Figure 4.103: Our Deconvolution in Wide-Field Microscopy (left) vs Confocal Microscopy (right). Source: Spectricon & FORTH

Finally, all the required datasets for the testing and evaluation of our research, was acquired by the proposed system. This gave us the opportunity to gain knowledge also in the biomedical research field, through the time and effort needed to select samples, understand their importance and produce representative images of their structure.

Chapter 5

Conclusions & Future Work

Summary Overall, this research demonstrated that there is a significant potential in combining the fields of electronics and biomedical science to construct innovative machinery for enhanced observation.

Automation of the mechanical parts of a microscope was held by designing our own stepper motor driver. The design focuses on the driver's compatibility with a wide variety of motors, from small and fast, to big and demanding. Moreover, the driver is capable of being (re)configured dynamically, which -when combined with real time motion control- enables robust operation on demanding situations like emergencies or synchronization. Finally, the configurable Acceleration/Deceleration slopes mechanisms provide a great tool for tuning the motor's behaviour and contending with the load's inertia. The drawbacks of this design are the significant bandwidth used for real time synchronization (which is considered an "easy" task), the complexity of tuning the stepper motor parameter in order to overextend its capabilities and the potential lack of efficiency in the three ESP32 hardware design (the use of one ESP32 was avoided due to the complexity of the design).

With the use of these automations related to the movement of the microscope, we focused on the image processing associated with the optimum focal estimation. This was accomplished by carefully crafting several algorithms and lead to the establishment of the Auto Focusing capability of our microscope. While testing these algorithms, we concluded that the best way of dissipating focal drifts, while executing the microscope's automated data acquisition processes, is to abort the use of these relative measures and find an absolute solution.

In order to address our need for focal estimation, without the use of neural networks based techniques - which is out of the scope of this research-, we implemented the most promising method we found in the literature, based on the research of the Egyptian Armed Forces el al [13]. This resulted in inconsistent estimations of focus quality for the proposed application. Subsequently, we designed a focus metric for absolute focus quality estimation. This method was based on the first derivative of the input images, which produces promising but still relative measurements. While analyzing the data provided by this metric, we examined cases where we could extract absolute information about an image's focal characteristics by comparing and thresholding a combination of our metrics. The resulting mechanism is a system that is able to accurately address the optimum focal plane of an imaging region. Additionally, it can also classify out of focus and in need of re-focusing regions, something that drastically improved the overall efficiency.

The drawback of this approach is the difficulty of evaluating its operation and consistency, which requires several tests under completely different circumstances and specimens, as well as a lot of time. A neural network or deep learning approach could potentially produce more accurate results and could need less time in evaluation due to its learning process.

The final technique implemented in this research is the Multi Focus Image Fusion. Its implementation was based on a study from Yong Yang et al [37]. This research guided us to the implementation of an image fusion method for z-stack datasets, based on the Discrete Wavelet Transform. In addition to the researchs' original design, we began experimenting with multichannel images (RGB)

and z-stack datasets that consist of more than two images. The results of our implementation for multi focus image fusion, but also -as a derivative- out of focus extraction, are promising. The drawbacks of a system like this are the intensive processing needed for the transformation of the images and verification of the fusion, as well as the fact that out of focus extraction outcome is correlated with the size of the z-stack.

In conclusion, the microscopy system of our research is indeed an easy to install and use motorized extension for digital microscopes. We managed to fully control and automate its mechanical and optical parts, reducing the contact with samples, providing a comfortable and relaxing imaging experience, while maximizing image quality and improving the repeatability of image capturing and measurement. Our outcome of more accurate data analysis and improved image processing techniques, will give a different perspective in the way experts observe and analyze the samples.

Future Work The design and implementation of the methods described in this research are a starting point, that updates any microscopes capabilities to the era of automation. This project is still a work in progress and despite the satisfying results presented in this thesis, we identify several potential improvements.

Regarding the motor driver, one easy-to-implement improvement would be to directly control its parameters through the GUI, allowing for easier tuning. Furthermore, the integration of specific sensors would give us the ability to have feedback regarding the motor's state. The captured inputs from the motor, would generate Interrupts (ISRs) for inspection of the motors operation (overloads, absence of load, motor current vs. expected current). This can help us fully automate the calibration procedure of different motors, which at this stage of development still requires significant effort. Another significant improvement would be the extension of its communication capabilities to Ethernet Communication. This is crucial in order to cope with the high bandwidth demand of our application, especially when dealing with multiple high resolution cameras.

Given the findings of our research regarding the absolute focus estimation, we believe that several improvements could be realised, leading to significant advances. One notable example is the automatic tuning of HoG bands, by observing the image's content, increasing this method's robustness. Additionally, image segmentation, based on the focal and topographical characteristics of the image, would also be an option. This could be achieved by utilizing several of the bands provided by the Histogram of Gradients analysis, in order to classify the desired characteristics, also leading to improvements to our out of focus extraction algorithm's performance. Finally, there is also the possibility of providing a normalised absolute focus estimation value, describing the image's percentage of focusing.

In every case, either by extracting the out of focus characteristics with the proposed Discrete Wavelet Transform or with the Gradients Based Metrics, a very useful tool shall emerge for the visualization of the segmented data in the 3D domain.

A fully operational microscope system is presented for the purpose of this thesis. All the construction and design processes required for its implementation, was held with appetite and careful guidance. Overall, it was a fun experience.

Bibliography

[1] William A. Locy, Transactions of the American Microscopical Society, 1923.

[2] ZEISS, Education in Microscopy and Digital Imaging, http://zeiss-campus.magnet.fsu.edu/articles/livecellimaging/techniques.html

[3] OLYMPUS, Introduction to Confocal Microscopy, https://www.olympus-lifescience.com/en/microscope-resource/primer/techniques/confocal/confocalintro

[4] C.J.R. Sheppard, X.Q. Mao, Confocal Microscopes with Slit Apertures, 1987.

[5] Holger Steiner, Hendrik Sommerhoff, David Bulczak, Norbert Jung, Martin Lambers, Andreas Kolb, Fast motion estimation for field sequential imaging: Surveyand benchmark, 2018.

[6] Wavelet Toolbox, http://matlab.izmiran.ru/help/toolbox/wavelet/dwt2.html.

[7] Yu Sun, Stefan Duthaler, Bradley J. Nelson, Autofocusing Algorithm Selection in Computer Microscopy, 2005.

[8] R. Redondo, M. G. Bueno, J. C. Valdiviezo, R. Nava, G. Crist´obal, M.Garc´ıa, O. D´eniz, B. Escalante-Ram´ırez, Evaluation of autofocus measures for microscopy images of biopsy and cytology, 2011.

[9] Z. Zhang, Focus and Blurriness Measure using Reorganized DCT Coefficients for Autofocus Application, 2015.

[10] F. Crete Roffet, The Blur Effect: Perception and Estimation with a New No-Reference Perceptual Blur Metric, 2007.

[11] R. Hurtado-Pérez, C. Toxqui-Quitl, A. Padilla-Vivanco, J. F. Aguilar-Valdez, G. Ortega-Mendoza, Focus measure method based on the modulus of the gradient of the color planes for digital microscopy, 2018.

[12] Samuel J. Yang, Marc Berndl, D. Michael Ando, Mariya Barch, Arunachalam Narayanaswamy, Eric Christiansen, Stephan Hoyer, Chris Roat, Jane Hung, Curtis T. Rueden, Asim Shankar, Steven Finkbeiner and Philip Nelson, Assessing microscope image focus quality with deep learning, 2018.

[13] Ramy M. Bahy 1, Gouda I. Salama 1, Tarek A. Mahmoud 1, A No-Reference Blur Metric Guided Fusion Technique For Multi-Focus Images, 2011.

[14] James G. McNally, Tatiana Karpova, John Cooper and Jose Angel Conchello, Three-Dimensional Imaging by Deconvolution Microscopy.

[15] Lowe, Distinctive Image Features from Scale-Invariant Keypoints, 2004.

[16] Karami, Image Matching Using SIFT, SURF, BRIEF and ORB: Performance Comparison for Distorted Images , 2017.

[17] Shree K. Nayar, Shape from Focus, Department of Electrical and Computer Engineering, The Robotics Institute, Carnegie Mellon University, Pittsburgh, Pennsylvania, 1989

[18] B.K.P. Horn, Focusing, MIT Artificial Intelligence Laboratory, Memo No. 160, 1968.

[19] J.M. Tenebaum, Accomodation in computer Vision, Ph.D. Thesis, Stanford University, 1970.

[20] R.A. Jarvis, Focus optimisation criteria for computer image processing, Microscope, Vol. 24, NO. 2, pp. 163-180, 1976.

[21] J.F. Schlag, A.C. Sanderson, C.P. Neumann, EC. Wimberly, Implementation of automatic focusing algorithms for a computer vision system with camera connol, Camegie Mellon University, CMU-RI-TR-83-14, August, 1983.

[22] E. Krotkov, Focusing, International Journal of Computer Vision, Vol. 1, pp. 223-237, 1987.

[23] E. Krotkov, Exploratory visual sensing with an agile camera, Ph.D. Dissertation, TR-87-29, University of Pennsylvania, 1987.

[24] A. Pentland, A new sense for depth of jeld, Proc. IJCAI, Los Angeles, pp, 988-994, August, 1985.

[25] P. Grossmann, Depthfrom Focus, Pattern Recognition Letters, Vol. 5, pp. 63-69, 1987.

[26] T. Darrell and K. Wohn, Pyramid Based Depthfrom Focus, Prw. CVPR, pp. 504-509, 1988.

[27] M. Subbarao, Direct Recovery of Depth Map 2: A New Robust Approach, Technical Report, 87-03, State University of New York, Stony Brook, 1987.

[28] T. Ohta, K. Sugihara, and N. Sugie, A Method for Image Composition using Image Variance, Transactions of IECE, Vol. J66-D, No. 10, pp. 1245-1246 , 1989.

[29] K. Kaneda, Y. Wakasu, E. Nakamae, E. Tazawa, A Method ofPan-Focused and Srereoscopic Display Using a Series of Optical Microscopic Images, Roc. of Fourth Symposium on Image Sensing Technologies in Industry, pp. 189-194, June, 1988.

[30] Zhang, B.H., Zhang, C.T., Liu, Y.Y., Wu, J.S., He, L., Multi-focus image fusion algorithm based on compound PCNN in Surfacelet domain. Optik, 125 (1), 296-300, 2014.

[31] Liu, G.X., Yang, W.H., A wavelet-decomposition-based image fusion scheme and its performance evaluation. Acta Automatica Sinica, 28 (6), 927-934, 2002.

[32] [18] Zheng, Y.F., Essock, E.A., Hansen, B.C., Haun, A.M. , A new metric based on extended spatial frequency and its application to DWT based fusion algorithms. Information Fusion, 8 (2), 177-192, 2007.

[33] Yang, Y., Park, D.S., Huang, S.Y., Yang, J.C., Fusion of CT and MR images using an improved wavelet based method. Journal of X-Ray Science and Technology, 18 (2), 157-170, 2010.

[34] Chen Y.Q., Chen L.Q., Gu H.J., Wang K., Technology for multi-focus image fusion based on wavelet transform. In Third International Workshop on Advanced Computational Intelligence, 25-27 August 2010. IEEE, 405-408, 2010.

[35] Li, H., Manjunath, B.S., Mitra, S.K., Multisensor image fusion using the wavelet transform. Graphical Models and Image Processing, 57 (3), 235- 245, 1995.

[36] Chu H, Li J., Zhu W.L., Multi-focus image fusion scheme with wavelet transform. Opto-Electronic Engineering, 32 (8), 59-63, 2005.

[37] Yong Yang, Shuying Huang, Junfeng Gao, Zhongsheng Qian, Multi-focus Image Fusion Using an Effective Discrete Wavelet Transform Based Algorithm, 2014.